Investigation of Fluid and Particle Transport in Undulating Micro- and Nanochannels

विद्या वाचस्पति की
उपाधि की अपेक्षाओं की आंशिक पूर्ति में प्रस्तुत शोध प्रबंध

A thesis submitted in partial fulfillment of the requirements of the degree of Doctor of Philosophy

द्वारा / By
आकाश / Aakash
पंजीकरण सं. / Registration No.: 20172026

शोध प्रबंध पर्यवेक्षक / Thesis Supervisor:
प्रो. अरिजीत भट्टाचार्य / Prof. Arijit Bhattacharyay

भारतीय विज्ञान शिक्षा एवं अनुसंधान संस्थान पुणे

INDIAN INSTITUTE OF SCIENCE EDUCATION AND RESEARCH PUNE

2025

List of Publications

1. Anand, A., & Bhattacharyay, A. (2023). Room temperature flashing ratcheting in nanochannels. *Physica A: Statistical Mechanics and its Applications, 626*, 128889.

   DOI: https://doi.org/10.1016/j.physa.2023.128889

2. Anand, A., & Bhattacharyay, A. (2025). Flow cross-overs under surface fluctuations in cylindrical nanochannel. *Physics Letters A*, Article 130676.

   DOI: https://doi.org/10.1016/j.physleta.2025.130676

3. Anand, A., & Bhattacharyay, A. (2025). Hydrodynamic ratcheting of tracers in microchannels: A detailed analysis.

   Preprint available at: arXiv:2510.12492.

Certificate

Certified that the work incorporated in the thesis entitled "*Investigation of fluid and particle transport in undulating micro- and nanochannels*", submitted by *Aakash* was carried out by the candidate under my supervision. The work presented here or any part of it has not been included in any other thesis submitted previously for the award of any degree or diploma from any other university or institution.

Date: December 24, 2025

Prof. Arijit Bhattacharyay

Thesis Supervisor

Declaration

I declare that this written submission represents my ideas in my own words. Where others' ideas have been included, I have adequately cited and referenced the original sources. I also declare that I have adhered to all principles of academic honesty and integrity. I have not misrepresented, fabricated, or falsified any idea, data, fact, or source in my submission. I understand that violation of the above will result in disciplinary action by the institute and may also lead to penal action if proper citation or permission has not been obtained from the sources used.

The work reported in this thesis is the original work done by me under the guidance of Prof. Arijit Bhattacharyay.

Date: December 24, 2025

Aakash

Reg. No. 20172026

This thesis is dedicated to

My Family.

Acknowledgments

"This thesis represents a journey of learning not only how to do research, but also how to mature and grow through a range of experiences, beyond the final destination."

Firstly and foremost, I would like to acknowledge my PhD supervisor, Prof. Arijit Bhattacharyay, for his kind support throughout the PhD journey, which wouldn't have been possible without his assistance. Throughout my PhD journey, I have learned a great deal from many people. I want to thank all those who helped make this journey easier for me.

I would like to express my sincere gratitude to my labmate, Mayank Sharma, for creating a supportive environment and providing all the necessary assistance, whether related to discussions or otherwise. I couldn't have asked for a better labmate. Special mention to Ritam Pal for his help whenever needed with any coding-related queries or otherwise. I want to acknowledge Sandipan Manna for his kind assistance with research discussions and other matters. I am grateful to Priyanka Gawade, who was pivotal in shaping my thinking process and fostering my curiosity. I would also like to acknowledge Shaunak Roy, my roommate, for his friendship and companionship, as well as Shiv Sagar Maurya for teaching me badminton during my PhD journey.

Beyond the PhD work, my experience was enriched by a vibrant community of people whom I met not only through academia but also through badminton, whom I would like to call the Badminton family. I am greatly indebted to Ritam Pal for introducing me to this fantastic sport of Badminton, which I will hold dear throughout my life.

I would like to express my deep gratitude to all the faculty at IISER Pune who have taught me, especially Prof. Deepak Dhar, from whom I have learned immensely. Words are simply not enough to describe the clarity and insight with which he explains physics

concepts. He is not only an excellent researcher but also a wonderful person, and I am very thankful to him for the many thought-provoking discussions.

I am also grateful to my batchmates and friends, Hitendra, Rajeev, Karthikeyan, Gaurav, Chetan, and many others, whose friendship and companionship I will cherish throughout my life. I would like to thank Dipanshu Garg for his constant emotional support and for his unique ability to present even the most complex ideas in a deceptively simple manner, often by insisting that "this is nothing," a perspective that never failed to bring a smile.

I am grateful to my RAC members, Dr. Bijay Aggarwalla and Prof. Sagar Chakraborty, for their valuable suggestions, and to the Physics staff at IISER Pune for their administrative and technical support. I also thank the anonymous reviewers whose feedback sharpened the quality of this research.

This work was supported by the Council of Scientific and Industrial Research (CSIR), India. I thank the CSIR for funding this research. I also thank the National Supercomputing Mission for providing computing resources of PARAM Brahma at IISER Pune. Finally, I would like to thank IISER Pune for the opportunity to conduct this research.

Aristotle once said, *"It is not enough to have a good mind; the main thing is to use it well."* I feel this is the right place to acknowledge the things that kept me mentally and physically healthy. Maintaining the clarity of mind required for this work was made possible by the IISER Pune gym and badminton facilities, which kept me physically and mentally fit.

Finally, I would like to extend my heartfelt gratitude and appreciation to my family members, especially my mother and brother, for their unwavering support and encouragement. To everyone who helped make this path easier to walk: thank you.

Aakash
IISER Pune

Abstract

This thesis explores the transport of particles and fluids through soft micro- and nanochannels with spatiotemporally undulating walls, a problem that sits at the intersection of biological transport and the design of next-generation nanofluidic devices. To study these systems, the work combines analytical perturbation theory for low-Reynolds-number flows with computational Langevin dynamics, capturing how thermal fluctuations, wall interactions, and external driving forces work together to shape transport.

The research is presented in three parts. First, we investigate an entropic flashing ratchet model, demonstrating that asymmetric surface fluctuations alone can drive directed particle transport. Our results identify optimal conditions for this phenomenon, showing it is maximally efficient for 10 nm particles in a water-like medium at room temperature.

Second, we analyze the competition between pressure-driven bulk flow and surface-driven boundary flow in a soft nanochannel. We develop a perturbation analysis that delineates these two regimes and derive a dimensionless parameter that quantifies the flow crossover, a result critical for applications in particle filtration and trapping.

In the final part, we develop a hydrodynamic ratchet model. Here, we demonstrate that carefully designed wall undulations can generate an asymmetric flow field capable of rectifying Brownian motion, resulting in a steady net particle drift. This mechanism provides a promising route for achieving controlled transport through purely hydrodynamic means. We derive the structure of fluid flow in this microchannel and the Boundary modes sustaining this fluid flow structure. Since surface-driven flow becomes stronger near the channel boundary, the presence of surface undulations is crucial when studying fluid or particle transport in a channel. This mechanism provides a promising route for achieving controlled transport through purely hydrodynamic means.

Overall, the thesis advances our theoretical understanding of particle transport in soft, confined environments and offers a quantitative framework that could guide the development of new nanofluidic pumps and separation devices.

Contents

1

Introduction

HANDLING fluids at the micro and nanoscales present a challenge from the perspective of technological applications, yet it is one of nature's greatest triumphs. Additionally, the quest to understand the transport processes in biological systems has driven curiosity to comprehend these mechanisms for the benefit of technology, as well as for pure scientific interest. For example, the directed motion of motor proteins carrying cargo, such as various cell organelles and other objects, occurs in a noisy environment without any net external drive. In a medium such as honey or molasses, propulsion immediately stops. However, these processes occur for our benefit, maintaining internal metabolism and functioning. The answer lies in the fascinating realization, *"When you cannot control noise and chaos on this scale, why not use it?"* Biological systems, from single-celled bacteria to multicellular organisms, rely heavily on transport processes for their proper functioning. These processes often occur through specialized micro- and nanochannels, even in the absence of an external pressure gradient. Depending on their characteristic dimensions, channels are generally classified as microchannels (typically 10 μm in diameter) and nanochannels (typically 1–100 nm in diameter).

In biological systems, well-known examples include ion channels and aquaporins. Ion channels are nanometer-scale membrane proteins that enable the selective transport of ions across membranes. Aquaporins, also known as water channels, are another type of biological nanochannel that forms pores in cellular membranes to facilitate the transport of single-file water at a very high speed. These structures exemplify nature's remarkable ability to control and direct molecular transport at nanoscale levels.

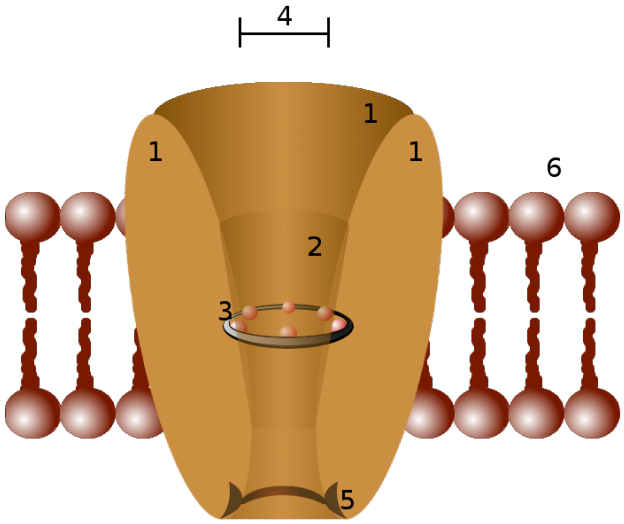

Figure 1.1: Schematic diagram of an ion channel protein. Adapted from the work of Outsider (Paweł Tokarz). Source: Wikimedia Commons, Public Domain [1].

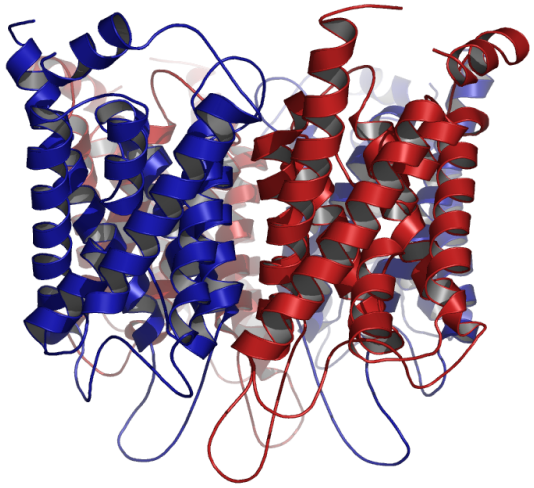

Figure 1.2: Schematic diagram of an aquaporin channel (PDB ID: 1J4N). Source: Vossman, Wikimedia Commons, licensed under CC BY-SA 3.0 [2].

At slightly larger scales, structures such as plasmodesmata in plants and gap junctions in animal tissues enable intercellular exchange through nanometric passages. Meanwhile, microscale conduits such as ciliary ducts, mucus-laden airways, and the highly crowded intracellular environment exhibit flows in which viscous forces dominate, and geometry exerts a strong influence on transport.

These examples demonstrate that nature routinely exploits confinement, thermal fluctuations, wall elasticity, and geometric asymmetry to achieve efficient transport without pressure-driven flow. Understanding these mechanisms is therefore crucial for designing artificial micro- and nanofluidic systems that mimic biological precision while requiring minimal external energy input.

These phenomena have naturally sparked human curiosity to understand their mechanisms. In biological systems, directed transport is achieved by motor proteins in the presence of thermal noise. Motor proteins act as Brownian motors (more about this later). Although the theory of Brownian motors is well-established and approximately a decade old, there is still a need to understand and design these systems, particularly at the micro- and nanoscales, especially within channels or confined geometries that exhibit undulating spatiotemporal behavior. In this direction, this thesis aims to understand the mechanisms of transport processes in micro- and nanochannels with soft, elastic walls from both biological and technological application perspectives, providing a detailed analytical and numerical treatment.

This thesis is motivated by a key question relevant to biological systems, synthetic microfluidics, and nanofluidics: How does transport occur in micro- and nanochannels without an external pressure driving force, and how can we develop a theoretical framework to understand the transport properties?

1.1 Background and Literature Review

At small scales, such as micro- and nanoscales, thermal noise plays a pivotal role. Thermal noise is not a useless phenomenon, but it is the primary driver of transport at these scales. Let us understand it in detail. We begin with a detailed account of Brownian motion (the thermal noise), including its history and development. We then examine various theories

to gain a deeper understanding of Brownian motion, which is crucial for its comprehension. We then study Brownian ratchets in detail and conclude the chapter by providing a brief description of motor proteins in both nature and technology.

1.1.1 Brownian Motion: The Physics of Noise

Imagine a speck of dust moving randomly, like dancing in a room with no air currents and no turbulence, in a sunbeam. This is an example of Brownian motion in action. Brownian motion is the random motion of particles suspended in a medium. This phenomenon has a rich history and has revolutionized the understanding of atoms and molecules. The word Brownian is named after Scottish Botanist Robert Brown, who first observed the constant, haphazard, and erratic motion of pollen grains of the plant *Clarkia pulchella* immersed in water in 1827 through a microscope. Initially, Brown thought it was a manifestation of life [3]. For a long time, the phenomenon of Brownian motion remained a mystery. In 1900, the French mathematician Louis Bachelier studied what is now known as Brownian motion in his doctoral thesis, *The Theory of Speculation*, in which he analyzed stock and option markets. However, his work was largely unknown till 1950. In 1905, Albert Einstein published a paper, "On the Movement of Small Particles Suspended in a Stationary Liquid Required by the Molecular-Kinetic Theory of Heat" [4], modeling the Brownian motion of pollen grains as being moved by the continuous hitting of water molecules, and provided the first mathematical framework for the understanding of Brownian motion. Einstein's theory was based on the existence of atoms and molecules. At that time, the existence of atoms and molecules was a subject of debate [5]. Following Einstein's 1905 theory, Marian Smoluchowski independently developed a kinetic description of Brownian motion in 1906 [6], also deriving the diffusion equation through a molecular collision argument. Three years later, in 1908 [7], Paul Langevin introduced a stochastic differential equation for the particle's velocity, combining Newton's law with a random force term. His formulation naturally led to the fluctuation–dissipation relation and offered a more intuitive mechanical picture of Brownian trajectories. In 1908, Jean Baptiste Perrin[1] conducted a series of experiments to observe the

[1] Jean Baptiste Perrin's quantitative measurements of Brownian motion provided one of the first precise experimental determinations of Avogadro's number, offering decisive evidence for the physical reality of atoms and resolving a long-standing debate. A decade later, Theodor Svedberg further reinforced the molecular theory of matter through ultracentrifugation studies of colloidal particles, obtaining molecular masses with remarkable accuracy. Perrin received the Nobel Prize in Physics in 1926 for his work, while Svedberg was awarded the Nobel Prize in Chemistry the same year. Their combined contributions effectively put the final

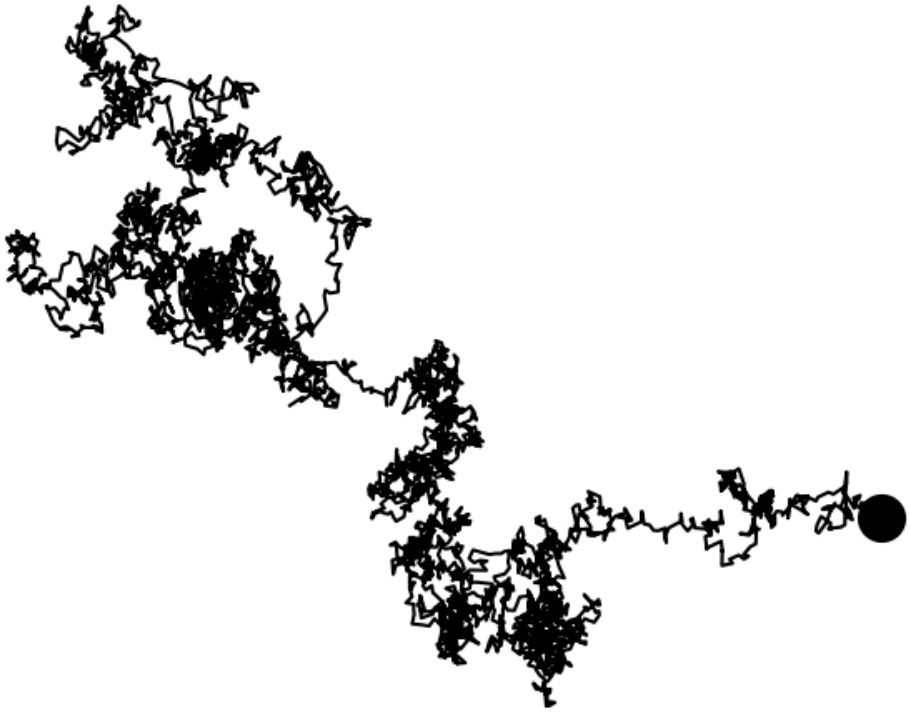

Figure 1.3: A two-dimensional trajectory of a particle undergoing Brownian motion.

Brownian motion of colloidal particles in water. By tracking the motion of many particles, Perrin experimentally verified Einstein's theory with remarkable accuracy. His experiments allowed him to calculate Avogadro's number with high accuracy. For his groundbreaking work, which settled the long-debated[2] The existence of atoms and molecules led to Perrin being awarded the Nobel Prize in Physics in 1926. Several excellent reviews on the history of Brownian motion are available [8, 9, 10, 11]. In 1923, Norbert Wiener provided the first mathematically rigorous foundation for Brownian motion, laying the groundwork for the mathematical concept of the Wiener process.

nail in the coffin of skepticism about the existence of atoms; shortly thereafter, academic publishers quietly removed conditional phrases such as "if atoms exist" from scientific textbooks.

[2]Before Einstein's 1905 theory, Henri Poincaré suggested Brownian motion might be the key to settling the atomic debate, but he never pursued it mathematically.

1.1.2 Theories of Brownian Motion

To transition from the qualitative observation of random motion to a precise physical understanding, several landmark theories were developed. These models range from Einstein's thermodynamic perspective to Langevin's mechanical formulation, providing the rigorous framework necessary to analyze fluctuations in microscopic systems.

1.1.2.1 Einstein's Theory

Einstein started by assuming atoms exist, then made a prediction based on that assumption, and finally, that prediction was verified by experiments. At the beginning of the twentieth century, the existence of atoms was a highly debated topic among physicists and chemists. Although chemists found the idea of atoms very useful for explaining chemical reactions, many prominent physicists opposed the concept of atomic existence. Einstein considered the increment of particle position in time τ in a one-dimensional space as a random variable with some probability density function $\varphi(\Delta)$. That is, $\varphi(\Delta)$ is the probability density for a jump of magnitude Δ, i.e., the probability density of particle incrementing its position from x to $x + \Delta$ in time interval τ. Assuming the conservation of particle number. Expanding $\rho(x, t + \tau)$ in the time variable using Taylor series, we get:

$$\rho(x, t + \tau) = \rho(x, t) + \tau \frac{\partial \rho(x, t)}{\partial t} + \cdots . \tag{1.1}$$

Now comes the conservation of particle part. Since the number of particles at x and at time $t + \tau$ equals the sum (integral) of all the contributions coming where particles take a jump in multiples of Δ (Δ can be positive and negative) from the previous time step, which is t, to arrive at x at time $t + \tau$, we get:

$$\rho(x, t + \tau) = \int_{-\infty}^{\infty} \rho(x - \Delta, t)\, \varphi(\Delta)\, d\Delta = \mathbb{E}_{\Delta}[\rho(x - \Delta, t)]. \tag{1.2}$$

Now expanding $\rho(x - \Delta, t)$ in the space variable using Taylor series, we get:

$$\rho(x, t+\tau) = \rho(x, t) \int_{-\infty}^{\infty} \varphi(\Delta)\, d\Delta - \frac{\partial \rho}{\partial x} \int_{-\infty}^{\infty} \Delta \varphi(\Delta)\, d\Delta + \frac{\partial^2 \rho}{\partial x^2} \int_{-\infty}^{\infty} \frac{\Delta^2}{2} \varphi(\Delta)\, d\Delta + \cdots . \tag{1.3}$$

The integral in the first term is equal to one by the definition of probability, and the second and other even terms (i.e., the first and other odd moments) vanish due to space symmetry. That is

$$\rho(x, t+\tau) = \rho(x,t) \cdot 1 - 0 + \frac{\partial^2 \rho}{\partial x^2} \int_{-\infty}^{\infty} \frac{\Delta^2}{2} \varphi(\Delta)\, d\Delta + \cdots . \tag{1.4}$$

What is left gives rise to the following relation:

$$\frac{\partial \rho}{\partial t} = \frac{\partial^2 \rho}{\partial x^2} \int_{-\infty}^{\infty} \frac{\Delta^2}{2\tau} \varphi(\Delta)\, d\Delta + \text{higher-order even moments},$$

where the coefficient after the Laplacian, the second moment of probability of displacement Δ, is interpreted as mass diffusivity D:

$$D = \int_{-\infty}^{\infty} \frac{\Delta^2}{2\tau} \varphi(\Delta)\, d\Delta.$$

Then the density of Brownian particles ρ at point x at time t satisfies the diffusion equation:

$$\frac{\partial \rho}{\partial t} = D \frac{\partial^2 \rho}{\partial x^2}.$$

For N particles starting out from the origin, above the equation has the following solution:

$$\rho(x,t) = \frac{N}{\sqrt{4\pi D t}} \exp\left(-\frac{x^2}{4Dt}\right). \tag{1.5}$$

The expression above for the probability density is a normal distribution with a mean of $\mu = 0$ and a variance of $\sigma^2 = 2Dt$. In his 1905 paper, Einstein considered a balance between the osmotic pressure acting on the Brownian particle (due to the concentration difference between the fluid and the Brownian particle itself) and the drag force, which gives the following relation:

$$D = \frac{k_B T}{6\pi\eta r} = \frac{RT}{6\pi\eta r N_A}. \tag{1.6}$$

Here,

- D: Diffusion coefficient of the Brownian particle, given by $D = \dfrac{k_B T}{\gamma} = \dfrac{k_B T}{6\pi\eta r}$.
- k_B: Boltzmann constant, which can be expressed as $k_B = \dfrac{R}{N_A}$, where R is the universal gas constant and N_A is the Avogadro number.

- η: Dynamic viscosity of the surrounding fluid.
- r: Radius of the spherical particle.

1.1.2.2 Langevin Model

Three years later, Paul Langevin described the Brownian motion using a different approach. He described the actual trajectory of a Brownian particle using Newton's second law of motion. In this model, he writes down Newton's equation of motion for the particle undergoing Brownian motion.

$$m\dot{v}(t) = F(t), \tag{1.7}$$

where $F(t)$ is the total force on the particle. We can write

$$F(t) = F_{\text{int}}(t) + F_{\text{ext}}(t). \tag{1.8}$$

Where $F_{\text{ext}}(t)$ is the resultant of all external, applied forces, while $F_{\text{int}}(t)$ is the internal force arising from the collisions of molecules of the fluid. $F_{\text{int}}(t)$ is the random force. It is random because we focus solely on the Brownian particle, disregarding the details of the velocities of each individual fluid molecule. It turns out that $F(t)$ can be written as:

$$F_{\text{int}} = \zeta(t) + F_{\text{sys}}(t). \tag{1.9}$$

Here $\zeta(t)$ is a truly random force and $F_{\text{sys}}(t)$ is a systematic random force that depends upon the velocity of the Brownian particle and

$$F_{\text{sys}}(t) = -\gamma v(t). \tag{1.10}$$

In the absence of any external forces,

$$m\,\frac{dv(t)}{dt} = -\gamma\, v(t) + \zeta(t). \tag{1.11}$$

Where $\zeta(t)$ is Gaussian white noise with zero mean and delta correlations, i.e.,

$$\langle \zeta(t) \rangle = 0, \qquad \langle \zeta(t)\zeta(t') \rangle = A\,\delta(t - t'),$$

and A is the (unknown) noise amplitude. This is the famous Langevin equation. It is a stochastic differential equation. The beauty of this equation lies in the fact that by solving it and applying the condition of equilibrium, specifically the equipartition theorem, Langevin was able to derive the same results that Einstein obtained through his theory. Thus, the random force is related to the damping coefficient γ and the temperature T of the medium through the fluctuation-dissipation theorem. Let us show the details of the solution of the Langevin equation.

Formal solution for $v(t)$ Rewrite Eq. 1.11 as

$$\dot{v}(t) + \frac{\gamma}{m} v(t) = \frac{1}{m}\zeta(t).$$

This is a linear inhomogeneous ODE. The integrating factor is $\exp(\gamma t/m)$. Multiplying and integrating from 0 to t gives

$$v(t)\, e^{\gamma t/m} - v(0) = \frac{1}{m}\int_0^t e^{\gamma s/m}\, \zeta(s)\, ds,$$

where $v(0)$ is the velocity of the particle at $t = 0$. Hence

$$v(t) = v(0)e^{-\gamma t/m} + \frac{1}{m}\int_0^t e^{-\frac{\gamma}{m}(t-s)}\, \zeta(s)\, ds\,. \tag{1.12}$$

Mean velocity and stationary limit Taking the ensemble average $\langle\cdot\rangle$ and using $\langle\zeta(t)\rangle = 0$ we get,

$$\langle v(t)\rangle = \langle v(0)\rangle e^{-\gamma t/m} \xrightarrow{t\to\infty} 0.$$

Velocity autocorrelation We define velocity autocoorelation by $C_v = \langle v(t)v(t')\rangle$. This quantity measures the correlation between the velocity of a particle at a later time and its velocity at an earlier time. So, the velocity autocorrelation measures the memory of the particle, i.e., how long the particle remembers about its past motion.

$$\langle v(t)v(t')\rangle = \langle v^2(0)\rangle e^{-\gamma(t+t')/m} + \frac{1}{m^2}\int_0^t ds \int_0^{t'} ds'\, e^{-\frac{\gamma}{m}(t-s)} e^{-\frac{\gamma}{m}(t'-s')} \langle\zeta(s)\zeta(s')\rangle.$$

In the long-time equilibrium limit, the contribution from initial conditions vanishes. Insert this into the stationary velocity autocorrelation (for $t \geq t'$):

$$\langle v(t)v(t')\rangle_{\text{eq}} = \frac{A}{m^2} e^{-\frac{\gamma}{m}(t+t')} \int_0^{t'} e^{-\frac{\gamma}{m}(t'-s)} e^{-\frac{\gamma}{m}(t'-s)} \delta(s-s')\, ds.$$

Carrying out the integrals properly (Details of these calculations are given in the appendix) yields the result

$$C_v(|t-t'|) \equiv \langle v(t)v(t')\rangle_{\text{eq}} = \frac{A}{2m\gamma}\, e^{-\frac{\gamma}{m}|t-t'|}\,,$$

where $|t-t'|$ denotes the time lag. In particular $\langle v^2(t)\rangle_{\text{eq}}$ is given by:

$$\langle v^2(t)\rangle_{\text{eq}} = \frac{A}{2m\gamma}. \tag{1.13}$$

Equipartition and determination of A From the equipartition theorem, we know that:

$$\frac{1}{2} m \langle v^2\rangle_{\text{eq}} = \frac{1}{2} k_B T.$$

Thus,

$$\frac{A}{2m\gamma} = \frac{k_B T}{m} \quad \Rightarrow \quad A = 2\gamma k_B T.$$

Thus, the noise correlator must be

$$\langle \zeta(t)\zeta(t')\rangle = 2\gamma k_B T\, \delta(t-t'),$$

which is the (classical) fluctuation-dissipation relation: the noise strength is fixed by the friction γ and the temperature T.

Diffusion coefficient Diffusion constant D is defined by:

$$D = \lim_{t\to\infty} \frac{\langle [x(t)-x(0)]^2\rangle}{t}. \tag{1.14}$$

Integrating the expression of $v(t)$, the mean-square displacement (MSD) is given by:

$$\langle [x(t) - x(0)]^2 \rangle = \frac{2k_B T}{\gamma} \left[t - \frac{m}{\gamma} \left(1 - e^{-\frac{\gamma t}{m}} \right) \right]. \tag{1.15}$$

For long times $t \gg m/\gamma$ (the diffusive regime), the exponential term is negligible and

$$\langle [x(t) - x(0)]^2 \rangle \simeq \frac{2k_B T}{\gamma} t \equiv 2Dt.$$

Hence, the diffusion coefficient is

$$D = \frac{k_B T}{\gamma}.$$

Stokes' friction and the Stokes–Einstein–Sutherland relation For a spherical particle of radius r moving in a viscous fluid of viscosity η under low-Reynolds-number conditions (Stokes flow), the friction coefficient is

$$\gamma = 6\pi\eta r \ .$$

Substituting into the expression for D gives the Stokes-Einstein-Sutherland [12] relation[3]

$$D = \frac{k_B T}{6\pi\eta r} \ .$$

Remarks and limiting cases:

- *Overdamped limit:* If inertia is negligible ($m \to 0$), the Langevin equation reduces to the overdamped form $0 = -\gamma v + \zeta$, and using the FDT immediately gives the Brownian diffusion $D = k_B T/\gamma$.
- *Short-time ballistic regime:* For $t \ll m/\gamma$, the MSD expands as $\langle \Delta x^2 \rangle \approx (k_B T/m)\, t^2$ (ballistic motion).
- *Long-time diffusive regime:* For $t \gg m/\gamma$, $\langle \Delta x^2 \rangle \approx 2Dt$.

[3]The well-known Stokes–Einstein relation was independently derived by William Sutherland in 1905, around the same time as Einstein's theory of Brownian diffusion. Although Sutherland's formulation correctly connected diffusion, viscosity, temperature, and particle size, his contribution is often less recognized, leading the relation to be commonly referred to only by Einstein and Stokes in the literature.

- The key physical content of the fluctuation–dissipation theorem is that thermal fluctuations (noise) and dissipation (friction) are not independent: equilibrium thermodynamics fixes the noise amplitude once γ and T are known.

1.1.3 The Research Frontiers: Micro- & Nanofluidics

Inspired by biological nanopores, the study of transport phenomena in artificial micro- and nanochannels has become a profoundly influential field of research. A dual motivation drives this growing interest: (i) the fundamental need to understand and replicate the precise transport mechanisms inherent in biological systems, and (ii) the immense technological promise of harnessing these phenomena to create novel engineered systems. The ambition to translate biological principles into technological advantages has propelled the development of microfluidics [13, 14, 15] and nanofluidics [16, 17], the study of fluid behaviour in confined geometries. The transport phenomena observed in ion channels of cell membranes are a remarkable example of nature's exploitation of nanoscale transport, which researchers have sought to emulate in artificial devices [18, 19].

Nanofluidics, in particular, investigates the behavior of fluids confined within nanometer-scale geometries (typically 1-100 nm). Confinement at these scales can give rise to transport properties that differ dramatically from those observed in bulk systems. Due to their small channel sizes, nanofluidic systems provide exquisite control over flow through surface fluctuations and modulations, enabling applications that require handling minute fluid volumes. These include chemical and particulate separation [20, 21], biomolecular analysis involving DNA and proteins [22, 23, 24, 25, 26, 27], cell capture and counting, and the development of micropumps and lab-on-a-chip devices [28, 29]. The Coulter counter [30] is a classic example of nanofluidic sensing technology that operates on these principles. Beyond biosensing and separation, nanofluidics also finds applications in nano-optics for fabricating tunable microlenses and detecting viruses and nanoparticles [31], as well as in biotechnology and molecular diagnostics [32].

In recent years, carbon nanotubes (CNTs) have emerged as highly efficient nanochannels capable of ultra-fast transport of water and gas molecules, with flow rates far exceeding theoretical predictions [33, 34]. Owing to their exceptional mechanical, electrical, and thermal properties [35, 36, 37], CNTs are now widely studied for desalination and water purification

applications. Moreover, analogies between fluid flow in nanochannels and charge carrier motion in semiconductor devices have inspired the design of nanofluidic rectifiers, transistors, and current modulators [38].

A key theoretical foundation for understanding fluid motion at these scales lies in classical low-Reynolds-number hydrodynamics [39, 40, 41]. In this regime, viscous forces dominate over inertial ones, resulting in laminar, predictable flow. This property enables the analytical treatment of flow using perturbation methods and lubrication theory. Studies of low-Reynolds-number flows have provided deep insights into the microscale manipulation of fluids [42], underpinning advances in lab-on-a-chip systems [43] and drug delivery devices [44].

The inversion symmetry breaking required for ratcheting can also be achieved in micro- and nanofluidic channels if the surfaces are elastic or semi-flexible, capable of supporting oscillations or stationary wave modes. Constructing such asymmetric boundary conditions enables the induction of surface-driven ratcheting [45, 46]. A foundational theoretical advance in the study of transport properties was made by Marbach et al. [47], who developed a framework for analyzing particle transport through nanochannels with fluctuating walls. Their work demonstrated that geometric features such as surface undulations can alter a particle's effective diffusion coefficient, leading to the emergence of entropic forces that can bias transport. Building upon this insight, this thesis explores how surface-driven entropic effects can be harnessed to produce flashing ratchet transport, revealing a potential pathway for passive particle filtration and separation at the nanoscale. Surface-driven flow mechanisms have also been explored from a broader hydrodynamic standpoint. Jaffrin and Shapiro [48] described peristaltic pumping, where progressive waves of contraction and expansion travel along a flexible wall to transport fluid—an effect ubiquitous in physiology. Recently, Kurzthaler et al. [49] have shown that even static surface corrugations can give rise to helical flow structures near soft boundaries. These findings highlight the crucial role of boundary geometry and elasticity in regulating nanoscale transport phenomena. The coexistence of multiple driving mechanisms, such as a bulk pressure gradient and surface undulations, in confined geometries can give rise to competing flow structures, in which different fractions of the fluid may move in opposite directions within a single nanochannel. Such effects are unique to low-Reynolds-number flows in soft micro- and nanoconfinements and would not be observed in wider geometries. These complex flow behaviors have promising implications for particle separation, trapping, and filtration applications [50, 51, 20, 52, 53, 54, 55, 21]. The combina-

tion of entropic transport, ratchet mechanisms, and surface dynamics in nanofluidic systems thus provides a rich and evolving framework for understanding and manipulating transport at the most minor scales. The interplay between geometry, forcing, and fluid properties governs the emergence of directed flow in the absence of net pressure gradients. Developing a detailed analytical approach to capture these effects in the low-Reynolds-number regime is crucial for uncovering the underlying principles governing nanoscale transport and enabling the design of next-generation nanofluidic devices for selective separation, filtration, and flow rectification.

Although extensive research has been conducted on ratcheting in microfluidic systems, its detailed exploration at the nanometer scale remains comparatively limited, despite its direct relevance to biological transport.

1.1.4 The Brownian Motor: Rectifying Noise with Ratchets

One of the most fascinating challenges in microfluidics and nanofluidics is to achieve directed transport without a net external pressure gradient, analogous to many biological systems. This phenomenon can be explained using the ratchet principle, which converts random Brownian motion into directed transport by breaking spatial and temporal symmetries [56, 57]. The essential ingredients are a broken spatial symmetry (e.g., an asymmetric potential) and a broken temporal symmetry (e.g., a non-equilibrium drive). These mechanisms can enable a diffusing particle to move against a potential or even against the bulk flow of a fluid [58, 59]. Experimental studies have demonstrated particle separation using micro-ratchet devices with periodically arranged, triangular-shaped obstacles [60, 61]. Ratcheting principles have also been applied to self-propel fluids, direct cell motion, and transport particles through micro-ratchet structures without the need for external power sources [62].

Researchers have developed a variety of passive and active methods for particle separation. Passive methods rely on geometric design and hydrodynamic forces, whereas active methods utilize external fields, such as electric or magnetic forces. For instance, Sajeesh et al. [50] reviewed both diagnostics and environmental monitoring strategies. Slapik et al. [51] exploited negative mobility, where particles move against an applied force, enabling tunable sorting of submicrometer particles. Derényi and Astumian [20] introduced transverse drift in asymmetric two-dimensional systems using AC forces to separate particles according to their

diffusion coefficients. Gorre-Talini et al. [52] demonstrated dielectrophoresis in asymmetric potentials for size-based particle sorting. Keller et al. [54] optimized particle separation using geometric ratchets and obstacle arrays, while Yamada et al. [55] achieved continuous size-based separation in laminar flows without external fields. Chacron et al. [63] and Caballero et al. [64] further demonstrated how temporal ratchets or mechanical asymmetries can trap particles or even guide cancer cells selectively.

The Paradox: Getting Order from Chaos The Second law of thermodynamics forbids us to get the directed motion from a system at thermal equilibrium. The Brownian ratchet, also known as the Feynman-Smoluchowski ratchet, is a device that appears to violate the second law of thermodynamics. It was first analyzed by Marian Smoluchowski [65] in a thought experiment in 1912, and then popularized by Richard Feynman [66].[4] The figure below shows a schematic of a Brownian ratchet.

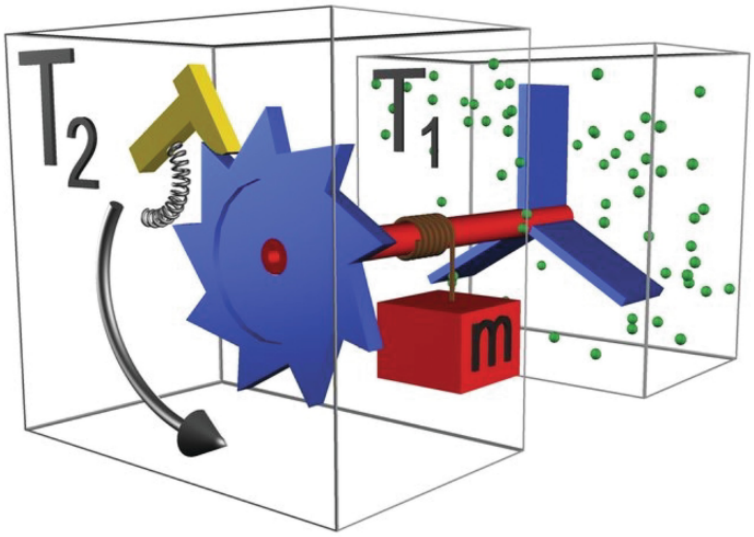

Figure 1.4: A schematic diagram of a Feynman-Smoluchowski ratchet. T_1 and T_2 represent two thermal baths at different temperatures. A weight m is attached to the shaft, which is driven by the rotation of the saw-tooth wheel (gear). The pawl prevents backward rotation, rectifying random thermal fluctuations into directed motion that lifts the weight m. Source: Reproduced from Suárez et al. (2016) [67], licensed under CC BY 3.0.

The device consists of a gear known as a ratchet, which can rotate freely in one direction

[4]Smoluchowski proposed the idea of a thermal ratchet more than fifty years before Feynman popularized it in his lectures. Feynman later admitted that he arrived at his conclusion without initially knowing Smoluchowski had already resolved the paradox historically.

but cannot rotate in the opposite direction due to the presence of a pawl. This ratchet and pawl arrangement is immersed in a heat bath of temperature T_2. This ratchet is connected to a shaft which connects to a paddle wheel immersed in a heat bath at a temperature T_1. A mass m hangs from the shaft. Initially, if both heat baths are at the same temperature, $T_1 = T_2 = T$, the devices appear to work by rectifying thermal motion due to the pawl. The collision due to the bath molecule will try to move the whole device in both directions with equal probability. However, due to the pawl, the ratchet can move only in one direction, apparently showing the rectification of thermal motion of molecules. It was demonstrated by Feynman, using quantitative analysis based on the Maxwell-Boltzmann distribution, in 1962, through detailed calculations, that the above devices cannot function unless both heat baths are at different temperatures, i.e., $T_1 \neq T_2$.

The basic argument for why the above device does not work for equal temperature baths is as follows: If the two baths are at the same temperature, then the pawl, which is also immersed in the heat bath, is at the same temperature. Due to this, the pawl will also perform a random motion in the up-and-down direction. This will allow the ratchet to move randomly in both clockwise and counterclockwise directions. Hence, the device doesn't work when the baths are at equal temperatures. If, on the other hand, the two baths are at different temperatures, then nothing prevents them from doing valuable work. Energy will be extracted from the temperature gradient between the two baths, and some waste heat will be generated and dumped into the lower temperature heat bath by the pawl. In this case, the device can function as a miniature engine in perfect accordance with the second law of thermodynamics.

In 1950, Brillouin [68] discussed the electrical circuit version of the ratchet device. This device uses a diode (a device that allows current to pass only in one direction by providing a very high resistance in the opposite direction). The device shows how to rectify the thermal current (Johnson Noise). Again, the detailed calculation showed that thermal fluctuations within the diode itself will cancel out the voltage from rectified current fluctuations.[5] Thus, again, this device will not produce any practical work if the components are at thermal equilibrium.

However, nothing prevents us from extracting useful work from the system when it is

[5]Brillouin referred to his electrical ratchet model as a diode rectifying thermal noise as a "thermodynamical demon," consciously poking fun at Maxwell's famous demon. His own calculations later showed the demon has no magical powers when at thermal equilibrium.

driven out of equilibrium. In the past, researchers have developed numerous methods to harness nonequilibrium forcing to produce useful work from a heat bath. Some of which are mentioned below.

Consider a Brownian particle of mass m under the potential $V(x,t)$ in a heat bath at temperature T. The Langevin equation for the Brownian particle can be written as:

$$m\frac{d^2x}{dt^2} = -\frac{\partial}{\partial x}V(x,t) - \gamma\frac{dx}{dt} + \sqrt{2\gamma k_B T}\xi(t). \tag{1.16}$$

Here $\xi(t)$ represents the Gaussian white noise with zero mean and unit variance. That is

$$\langle \xi(t) \rangle = 0 \tag{1.17}$$

and

$$\langle \xi(t)\xi(t') \rangle = \delta(t-t'). \tag{1.18}$$

For systems where viscous effects are more significant than inertial effects, the dynamics given by the above equation simplify to overdamped dynamics, i.e., the inertia term $m\ddot{x}$ becomes negligible. Thus, we arrive at:

$$\gamma\dot{x} = -\frac{\partial}{\partial x}V(x,t) + \sqrt{2\gamma k_B T}\xi(t), \tag{1.19}$$

which can also be written as:

$$\frac{dx}{dt} = -\frac{1}{\gamma}\frac{\partial}{\partial x}V(x,t) + \sqrt{2D}\xi(t). \tag{1.20}$$

The conditions on the potential $V(x,t)$ to show the ratcheting effect are as:

- Breaking Thermal Equilibrium: The system cannot be at a uniform temperature or in a state of rest. You must continuously feed energy into it to keep it out of equilibrium. This crucial step makes the Second Law's "loophole" possible.
- Breaking Spatial Symmetry: The potential must have a broken symmetry in x. There are many ways to achieve this. This condition, in some sense, produces the anisotropy in the spatial direction.

Depending on the ways to drive the system out of equilibrium, there are different types of ratchets studied in the literature. Mainly, there are two different types of ratchets:

- Flashing Ratchet (On-Off Ratchet): In these ratchets, the spatial part of the potential $V(x)$ oscillates in time between its maximum and minimum value. This amounts to choosing a term like $\sin^2(\omega t)$ for the time-dependent part $T(t)$ in the potential $V(x,t)$, where ω is the angular frequency of oscillation of the potential.
- Rocking Ratchet (Tilting Ratchet): In these types of ratchets, the spatial potential $V(x)$ performs a rock and roll kind of motion between a maximum and a minimum value. This basically amounts to adding a term of the form $c_0 x \sin(\omega t)$. Here ω is the frequency of the rocking of the potential.

In both of the above cases of ratchet potentials, the spatial part is of the form:

$$V(x) = V_0\left[\sin\left(\frac{2\pi x}{L}\right) + \frac{1}{4}\sin\left(\frac{4\pi x}{L}\right)\right]. \tag{1.21}$$

Figure 3.3 shows a graph of the above potential. Now, let us examine the working of the

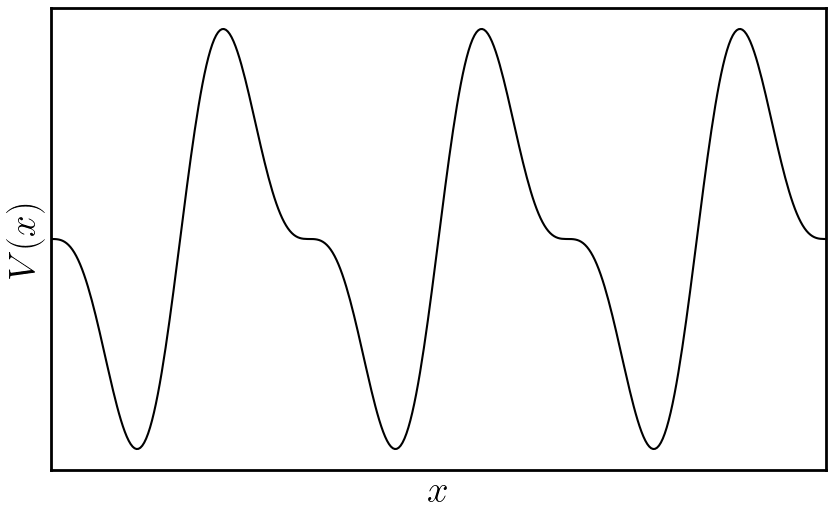

Figure 1.5: A snapshot of the ratchet potential $V(x,t)$

most commonly used flashing ratchet in detail. Imagine initially that the potential is ON

and particles are localized near the minima of the potential wells, as shown in the figure. In the presence of thermal noise, the particles undergo small fluctuations but are unable to cross the potential barriers.

When the potential switches OFF, the barriers disappear and particles diffuse freely, spreading symmetrically in both directions. Upon switching the potential back ON, the redistributed particles are recaptured into nearby wells. Due to the asymmetric shape of the potential, the distances and barrier slopes on either side of a minimum are unequal, leading to unequal probabilities of recapture in the forward and backward directions. As a result, a fraction of particles preferentially move to neighboring wells in one direction. Repeating this switching cycle leads to a net directed transport of particles.

It is important to note that spatial asymmetry of the potential is an essential ingredient for directed transport in a flashing ratchet. During the OFF phase, diffusion is unbiased and does not generate net motion. Directed transport arises only during the recapture step when the potential is switched back ON. In the absence of spatial asymmetry, the recapture process would be symmetric, and no net transport would occur even under temporal modulation.

1.1.5 Brownian Motors in Nature and Technology

In biological systems, Brownian motors exist in various forms, primarily as proteins. Well-known examples include ATP synthase, which operates as a rotary motor, and myosin II, a linear motor that plays a central role in muscle contraction.

Other important motor proteins found in living cells are kinesin and dynein. These proteins convert chemical energy into mechanical motion through the hydrolysis of adenosine triphosphate (ATP). Kinesin is a motor protein complex that moves along microtubule filaments, using ATP as its energy source. This directed motion enables kinesin to participate in essential cellular processes such as meiosis, mitosis, and the intracellular transport of vesicles and other cargo.

Inside a cell, small molecules such as gases and glucose can reach their targets via diffusion. In contrast, larger biomolecules are synthesized near the cell body, and intracellular structures, such as vesicles and organelles, are too large—and the cytosol too crowded—for efficient diffusion to occur. Consequently, active transport mechanisms are required. Motor

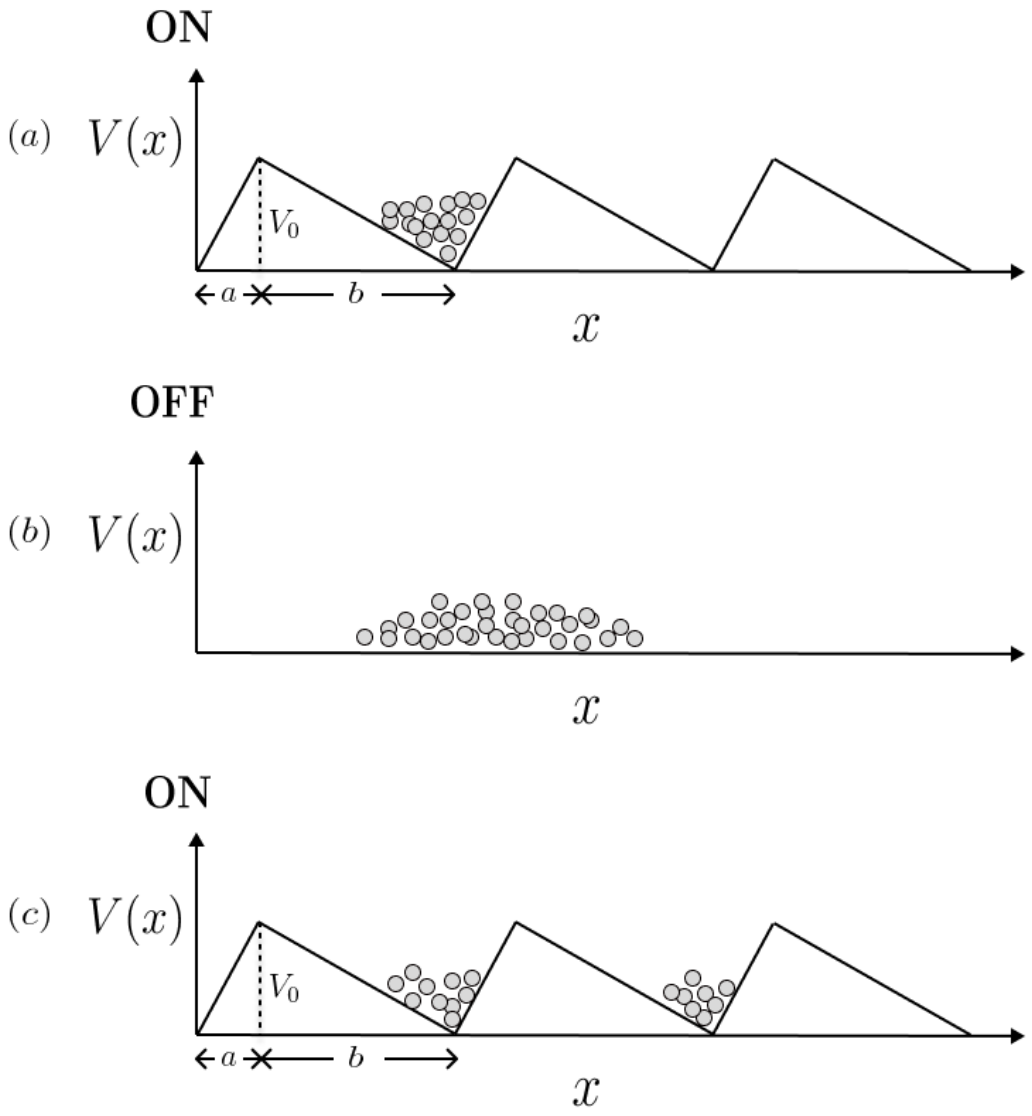

Figure 1.6: Schematic representation of particle transport in a flashing ratchet. (a) When the potential is "ON", particles remain trapped in the potential wells, as thermal fluctuations are not sufficient for them to overcome the barrier. (b) When the potential is switched "OFF", particles diffuse freely in both directions. (c) When the potential is switched "ON" again, a fraction of particles gets trapped in the next well, resulting in directed transport.

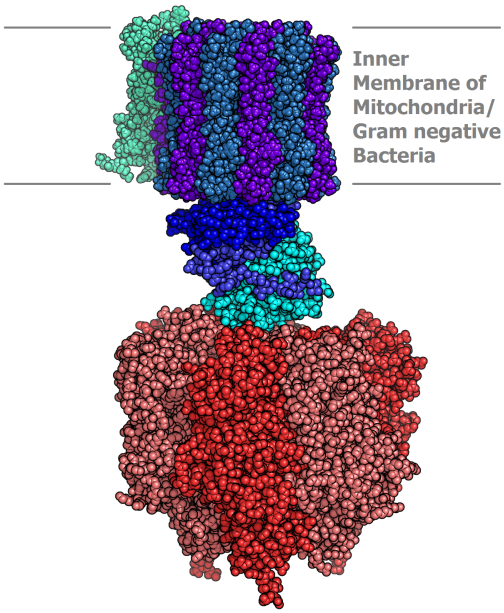

Figure 1.7: Structure of ATP synthase (using PDB data and PyMOL). Source: Alex_X, Wikimedia Commons, licensed under CC BY-SA 3.0 [69].

proteins fulfill this role by carrying large cargoes to specific destinations within the cell. Kinesins transport cargo unidirectionally along microtubule tracks, consuming one ATP molecule per step. A schematic representation of kinesin motility along a microtubule is shown in Figure 1.8. Recent experimental studies have enabled the direct observation of kinesin motion in real time, revealing a "hand-over-hand" walking mechanism in which the two motor heads alternate between leading and trailing positions during successive steps.

It was initially assumed that each forward step of kinesin was directly powered by the energy released during ATP hydrolysis. However, an alternative mechanism has been proposed in which the motor head undergoes thermally driven diffusion, and directional movement arises when binding to the next microtubule site biases this diffusion, effectively pulling the attached cargo forward.

Dyneins form another class of motor proteins that move toward the minus end of microtubules. As a result, dyneins transport cellular components from the cell's periphery toward its interior.

Brownian motors are nanoscale machines that exploit chemical energy to generate di-

rected motion. At such small length scales, viscous forces dominate over inertia, and thermal fluctuations play a central role, rendering conventional mechanical strategies ineffective. The concept of Brownian motors was introduced by Peter Hänggi [70]. These motors provide a framework for understanding various biological processes that require directional motion, including protein synthesis and muscle contraction. A seminal contribution to the theoretical understanding of Brownian motors was made by Dean Astumian and Peter Hänggi, who described the thermodynamics of noise-driven transport in an influential article published in Physics Today [57, 70].

In the years following this theoretical development, researchers successfully constructed artificial Brownian motors. In 2018, IBM demonstrated a practical realization of an artificial Brownian motor by engineering a nanofluidic slit with a carefully designed energy landscape. By applying time-dependent potentials in conjunction with oscillating electric fields, they achieved controlled and directed motion of nanoparticles. In a striking demonstration, particles were guided along trajectories forming the IBM logo, representing a significant milestone in the experimental implementation of Brownian motors at the nanoscale.

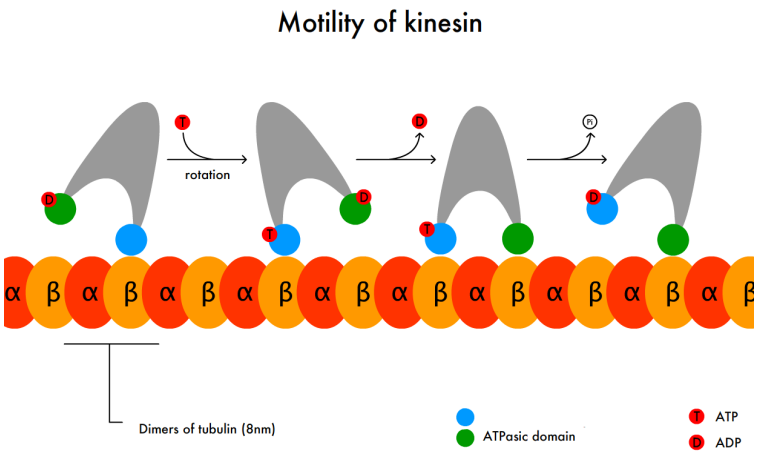

Figure 1.8: Schematic of the movement of kinesin along a microtubule. Source: Slagt (modified by Bcjordan), Wikimedia Commons, Public Domain [71].

1.2 Problem Statement

The preceding sections demonstrate that, while ratcheting principles are well-established and the importance of soft nanochannels is recognized, a detailed theoretical framework connecting them is lacking. This is especially true for transport driven by entropic effects from fluctuating, elastic walls. Therefore, this thesis aims to bridge this gap by addressing the following key question: How do surface undulations in soft micro- and nanochannels help in transport, and how can they be modeled to predict and optimize particle transport for filtration and separation?

The primary contribution of this thesis lies not in introducing a fundamentally new physical principle, but in developing a quantitative and physically consistent framework to understand how time-dependent boundary deformations generate velocity fields that can induce directed transport.

1.3 Overview of the thesis

This thesis is divided into six chapters and an appendix. The present chapter, Chapter 1, introduces the research motivation, provides an overview of existing work in the field, and sets the stage for the subsequent analysis. Chapter 2 focuses on the essential theoretical foundations for this research. It covers the Navier-Stokes equation, low-Reynolds-number hydrodynamics, and fundamental concepts of fluid-particle interaction, including Stokesian dynamics, Langevin dynamics, and Brownian dynamics. This chapter also details the numerical methods used to integrate stochastic differential equations, such as the Euler-Maruyama and Stochastic Heun methods. Finally, it introduces the basic concepts of the Fokker-Planck equation. Chapter 3 presents the first research project, which utilizes a Fokker-Planck formalism to establish the velocity profile experienced by a tracer particle due to surface undulation within a nanochannel. This chapter lays the groundwork for understanding transport in nanochannels. This chapter demonstrates that broken symmetric surface undulations can lead to transport in nanochannels. Subsequently, Chapter 4 discusses the application of low-Reynolds-number hydrodynamics to understand fluid flow in a nanochannel affected by surface undulations. This chapter examines the effect of surface undulations on the velocity profile in an undulating nanochannel, thereby establishing a distinction between

surface-driven and pressure-driven flows. Chapter 5 develops an analytical theory for the hydrodynamic ratchet. Provides a detailed theoretical treatment of fluid field flow, the associated surface model, and the transport of tracer particles within a soft microchannel. Chapter 6 summarizes the research work, discusses prospects, and concludes the thesis. In the end, we have attached an appendix containing the details of various concepts necessary to understand certain topics or to provide the missing information in the thesis.

2

Theoretical Background and Methods

In this chapter, we introduce the governing equations of fluid dynamics, the Navier-Stokes equation. We present it in a general form and then reduce it to the case of the low-Reynolds-number regime, which is relevant to this thesis. We discuss the associated boundary conditions, followed by a discussion on the validity of the Navier-Stokes equations for micro- and nanofluidics systems, which are the relevant systems for this thesis. Next, we present the equations governing the dynamics of a particle in a fluid, specifically the Langevin equation and the Fokker-Planck equation. Finally, we present some basics of stochastic calculus necessary to understand the mathematics, including the concept of the Wiener process, stochastic differential equations (SDEs), and numerical schemes for solving the SDEs.

The concepts and methods introduced in this chapter will be used extensively in later chapters. In particular, the Navier-Stokes formulation developed in this chapter is applied in Chapters 4 and 5, while the framework of stochastic processes introduced in this chapter will form the basis of particle transport modeling in Chapters 3 and 5.

2.1 The Navier–Stokes Equation

The behavior of a viscous fluid (liquids and gases) is described by the Navier-Stokes equation.[1] These equations mathematically describe the momentum balance for fluids. Navier-Stokes equations are Partial differential equations describing the behavior of the velocity

[1]The Navier–Stokes equations are named after Claude-Louis Navier (1822) and George Gabriel Stokes (1845), who independently formulated the viscous momentum equation.

field $\boldsymbol{u}(\boldsymbol{r}, t)$ of the fluid. Navier-Stokes equations can be described as a particular form of the Cauchy momentum equation, which, in the form of material derivative, is given by:

$$\rho \frac{D\boldsymbol{u}}{Dt} = \nabla \cdot \boldsymbol{\sigma} + \boldsymbol{f}_{\text{ext}}. \tag{2.1}$$

Here $\boldsymbol{\sigma}$ is the Cauchy stress tensor, which is a sum of the viscosity term $\boldsymbol{\tau}$ (deviatoric stress) and the pressure term $-p\mathbb{I}$ ($\mathbb{I}$ is Identity tensor). Writing $\boldsymbol{\sigma}$ in terms of viscosity and pressure, the Cauchy momentum equation becomes:

$$\rho \left(\frac{\partial \boldsymbol{u}}{\partial t} + (\boldsymbol{u} \cdot \nabla)\boldsymbol{u} \right) = -\nabla p + \nabla \cdot \boldsymbol{\tau} + \boldsymbol{f}_{\text{ext}} \tag{2.2}$$

This is known as Navier-Stokes equation. In the above equation, the stress terms p and $\boldsymbol{\tau}$ are still unknown, so this equation alone cannot be used to solve the problems. A force model is needed relating the stresses to the velocity field. For a Newtonian fluid, $\boldsymbol{\tau}$ is given by

$$\boldsymbol{\tau} = \lambda \operatorname{tr}(\boldsymbol{\varepsilon})\mathbb{I} + 2\eta\boldsymbol{\varepsilon}, \tag{2.3}$$

where $\boldsymbol{\varepsilon}$ is known as rate of strain tensor and λ and η are respectively known as second viscosity and dynamic viscosity of fluid. Writing $\boldsymbol{\varepsilon}$ in terms of velocity gradient:

$$\boldsymbol{\varepsilon} = \frac{1}{2}\left(\nabla \boldsymbol{u} + (\nabla \boldsymbol{u})^T\right). \tag{2.4}$$

In Eq. 2.2

- ρ is the mass density.
- $\boldsymbol{u}$ is the flow velocity vector.
- $\dfrac{D}{Dt}$ is the material derivative, defined as $\dfrac{\partial}{\partial t} + \boldsymbol{u} \cdot \nabla$.
- ∇ is the nabla operator.
- p is the pressure.
- t is time.
- $\boldsymbol{\tau}$ is the deviatoric stress tensor.

- $\boldsymbol{f}_{\text{ext}}$ is the external force per unit volume.

Since $\text{tr}(\boldsymbol{\varepsilon}) = \nabla \cdot \boldsymbol{u}$, therefore

$$\boldsymbol{\sigma} = -p\mathbb{I} + \lambda(\nabla \cdot \boldsymbol{u})\mathbb{I} + \eta(\nabla \boldsymbol{u} + (\nabla \boldsymbol{u})^T). \tag{2.5}$$

Introducing the bulk viscosity $\zeta = \lambda + \frac{2}{3}\eta$, we get the Linear stress constitutive equation, which is used for fluids:

$$\boldsymbol{\sigma} = -p\mathbb{I} + \eta(\nabla \boldsymbol{u} + (\nabla \boldsymbol{u})^T) + \big(\zeta - \frac{2}{3}\eta\big)(\nabla \cdot \boldsymbol{u})\mathbb{I}. \tag{2.6}$$

Thus, the most general Navier-Stokes equation is:

$$\rho\bigg(\frac{\partial \boldsymbol{u}}{\partial t} + (\boldsymbol{u} \cdot \nabla)\boldsymbol{u}\bigg) = -\nabla p + \nabla \cdot \bigg\{\eta\Big[\nabla \boldsymbol{u} + (\nabla \boldsymbol{u})^T - \frac{2}{3}(\nabla \cdot \boldsymbol{u})\mathbb{I}\Big]\bigg\} + \nabla\big(\zeta\,(\nabla \cdot \boldsymbol{u})\big) + \boldsymbol{f}_{\text{ext}}. \tag{2.7}$$

Finally, the associated continuity equation expressing the conservation of mass is given by:

$$\frac{\partial \rho}{\partial t} + \nabla \cdot (\rho \boldsymbol{u}) = 0. \tag{2.8}$$

If we assume the constant viscosity and incompressibility of the fluid, i.e., $\dfrac{d\rho}{dt} = 0$. The above equation becomes:

$$\nabla \cdot \boldsymbol{u} = 0. \tag{2.9}$$

And the Navier-Stokes equation reduces to :

$$\rho\bigg(\frac{\partial \boldsymbol{u}}{\partial t} + (\boldsymbol{u} \cdot \boldsymbol{\nabla})\boldsymbol{u}\bigg) = -\nabla p + \eta\nabla^2 \boldsymbol{u} + \boldsymbol{f}_{\text{ext}}. \tag{2.10}$$

In cylindrical coordinates

$$\begin{aligned}
\rho\left(\frac{\partial u_r}{\partial t} + u_r\frac{\partial u_r}{\partial r} + \frac{u_\theta}{r}\frac{\partial u_r}{\partial \theta} - \frac{u_\theta^2}{r} + u_z\frac{\partial u_r}{\partial z}\right) &= -\frac{\partial p}{\partial r} + \eta\left[\nabla^2 u_r - \frac{u_r}{r^2} - \frac{2}{r^2}\frac{\partial u_\theta}{\partial \theta}\right] + f_r,\\
\rho\left(\frac{\partial u_\theta}{\partial t} + u_r\frac{\partial u_\theta}{\partial r} + \frac{u_\theta}{r}\frac{\partial u_\theta}{\partial \theta} + \frac{u_r u_\theta}{r} + u_z\frac{\partial u_\theta}{\partial z}\right) &= -\frac{1}{r}\frac{\partial p}{\partial \theta} + \eta\left[\nabla^2 u_\theta - \frac{u_\theta}{r^2} + \frac{2}{r^2}\frac{\partial u_r}{\partial \theta}\right] + f_\theta,\\
\rho\left(\frac{\partial u_z}{\partial t} + u_r\frac{\partial u_z}{\partial r} + \frac{u_\theta}{r}\frac{\partial u_z}{\partial \theta} + u_z\frac{\partial u_z}{\partial z}\right) &= -\frac{\partial p}{\partial z} + \eta\nabla^2 u_z + f_z \qquad \text{and,}
\end{aligned} \tag{2.11}$$

$$\frac{1}{r}\frac{\partial(ru_r)}{\partial r} + \frac{1}{r}\frac{\partial u_\theta}{\partial \theta} + \frac{\partial u_z}{\partial z} = 0, \tag{2.12}$$

where

$$\nabla^2 = \frac{1}{r}\frac{\partial}{\partial r}\left(r\frac{\partial}{\partial r}\right) + \frac{1}{r^2}\frac{\partial^2}{\partial \theta^2} + \frac{\partial^2}{\partial z^2}. \tag{2.13}$$

This governing equation forms the foundation for the analysis of fluid flow in undulating nanochannels presented in Chapter 4 and is further extended in the hydrodynamic ratchet model for fluid flow in undulating microchannels in Chapter 5.

2.1.1 Non-dimensionalization of Navier-Stokes Equation

In fluid dynamics, it is often helpful to nondimensionalize the Navier-Stokes equation, making the problem at hand easy to analyse by reducing the number of parameters. Non-dimensionalisation of the Navier-Stokes equation depends upon the various scales representing typical physical quantities. These scales are selected based on the specific problem at hand. For the case of fluid flow without heat transfer, the non-dimensionalised equation depends only on the Reynolds number Re. The table shown below represents the non-dimensionalization of various variable by the typical scales. In terms of dimensionless variables, the incompressible Navier-Stokes equation becomes:

$$\frac{\partial \boldsymbol{u}^*}{\partial t^*} + (\boldsymbol{u}^* \cdot \nabla^*)\boldsymbol{u}^* = -\nabla^* p^* + \frac{1}{\mathrm{Re}}\nabla^{*2}\boldsymbol{u}^* + \boldsymbol{f}'_{\mathbf{ext}}. \tag{2.14}$$

Table 2.2: Comparison of flow regimes based on Reynolds number.

Regime	**Reynolds Number (Re)**	**Typical Systems**
Low Reynolds Number ($\mathrm{Re} \ll 1$)	Viscous forces dominate	Microchannels, nanochannels, bacterial swimming, intracellular transport
High Reynolds Number ($\mathrm{Re} \gg 1$)	Inertial forces dominate	Airplanes, cars, ocean currents, blood flow in large arteries

Table 2.1: Non-dimensionalization of variables based on characteristic length, velocity, time, and pressure scales.

Scale	**Dimensionless Variable**
Length L	$\boldsymbol{r}^* = \dfrac{\boldsymbol{r}}{L}, \qquad \nabla^* = L\nabla$
Flow velocity U	$\boldsymbol{u}^* = \dfrac{\boldsymbol{u}}{U}$
Time L/U	$t^* = \dfrac{t}{L/U}$
Pressure (high Re)	Dynamic-dominated flows: $p^* = \dfrac{p}{\rho U^2}$
Pressure (low Re)	Viscous-dominated creeping flows: $p^* = \dfrac{pL}{\mu U}$

In the above equation, Re is a dimensionless number known as the Reynolds number. Its value measures the relative importance of inertia compared to viscosity small Re values represent the viscosity-dominated flows, and a high value of Re represents the inertia-dominated flows. In terms of typical scales of the system Re can be expressed as:

$$\mathrm{Re} = \frac{\rho U L}{\eta}. \tag{2.15}$$

The Reynolds number thus quantifies the relative importance of inertial and viscous effects in the flow. In the limit $\mathrm{Re} \ll 1$, viscous forces dominate, leading to laminar and reversible flow, characteristic of micro- and nanofluidic systems. In contrast, for $\mathrm{Re} \gg 1$, inertial effects become significant, often resulting in complex and potentially turbulent flow behavior.

In this thesis, we are primarily concerned with the low-Reynolds-number regime, where the Navier–Stokes equation simplifies significantly. The low-Reynolds-number approximation derived here is central to the perturbative analysis of flow in confined geometries discussed

in Chapter 4 and Chapter 5.

2.1.2 Boundary Conditions Used in Fluid Dynamics

To determine the solution of the Navier-Stokes equation uniquely and to impose the physical constraints on the dynamics of fluid, we use boundary conditions. Let us study the most commonly used boundary conditions in fluid dynamics.

2.1.2.1 No-Slip Boundary Condition

In fluid dynamics, the no-slip boundary condition[2]is a boundary condition that ensures the tangential component of the relative velocity of the fluid with respect to the wall's velocity is zero. Mathematically, it says:

$$(\boldsymbol{u} - \boldsymbol{U}_{\text{wall}}) \cdot \hat{\boldsymbol{t}} = 0 \tag{2.16}$$

The no-slip condition is an empirical observation that is useful in modeling many macroscopic experiments. When the molecules of fluid closer to the walls have a stronger adhesive force with the wall molecules compared to the cohesive forces between water molecules, the no-slip assumption holds. There are physical scenarios in which it fails. For sufficiently rarefied flow, the no-slip condition is inaccurate.

2.1.2.2 Kinematic Boundary Condition

In any fluid dynamics problem involving boundaries, it is essential to define how the fluid interacts with its confining surfaces. The kinematic boundary condition is a fundamental statement that applies to impermeable boundaries, whether they are stationary or in motion.

Conceptually, the kinematic boundary condition states that a fluid particle located at a boundary must remain at that boundary. In other words, the fluid cannot flow through an impermeable surface. This implies that the component of the fluid's velocity normal to the boundary must be equal to the component of the boundary's own velocity normal to itself. This condition is purely kinematic, as it deals with motion and geometry, and is independent

[2]The no-slip condition was initially controversial, Maxwell argued fluids may slip at walls, and even today slip lengths become significant at the nanoscale.

of the fluid's properties, like viscosity. Mathematically, it says:

$$(\boldsymbol{u} - \boldsymbol{U}_{\text{wall}}) \cdot \hat{\boldsymbol{n}} = 0 \tag{2.17}$$

Suppose the boundary can be represented by the function

$$F(x, y, z, t) = 0, \tag{2.18}$$

so that a point (x, y, z) lies on the surface if and only if it satisfies $F = 0$. Since fluid particles on the surface stay on the surface, the total (time) derivative of F following the surface must vanish:

$$\frac{DF}{Dt} = 0. \tag{2.19}$$

Since,

$$\frac{DF}{Dt} = \frac{\partial F}{\partial t} + u\frac{\partial F}{\partial x} + v\frac{\partial F}{\partial y} + w\frac{\partial F}{\partial z}, \tag{2.20}$$

where (u, v, w) are the components of the fluid velocity field $\boldsymbol{u} = (u, v, w)$, the kinematic boundary condition becomes

$$\frac{\partial F}{\partial t} + \boldsymbol{u} \cdot \nabla F = 0 \quad \text{on } F = 0. \tag{2.21}$$

This is the most general expression of the kinematic boundary condition. When it is possible to describe the surface as a height function:

$$z = \eta(x, y, t),$$

that is,

$$F(x, y, z, t) = z - \eta(x, y, t) = 0.$$

Then kinematic boundary condition can be simplified as:

$$\frac{\partial F}{\partial t} = -\frac{\partial \eta}{\partial t}, \qquad \nabla F = \left(-\frac{\partial \eta}{\partial x}, -\frac{\partial \eta}{\partial y}, 1\right).$$

Substituting into Eq. 2.21,

$$-\eta_t - u\,\eta_x - v\,\eta_y + w = 0, \tag{2.22}$$

or equivalently,

$$\frac{\partial \eta}{\partial t} + u\frac{\partial \eta}{\partial x} + v\frac{\partial \eta}{\partial y} = w \quad \text{at } z = \eta(x, y, t). \tag{2.23}$$

These boundary conditions are directly employed in modeling the undulating channel walls in Chapter 4 and in constructing the hydrodynamic ratchet mechanism in Chapter 5.

2.1.3 Validity of the Navier-Stokes Equations in Micro- and Nanofluidics

The Navier–Stokes equations are the cornerstone of classical fluid dynamics, but their application to micro- and nanofluidic systems requires careful consideration. Their validity hinges on a fundamental assumption known as the *continuum assumption*. The continuum assumption treats a fluid as a continuous medium rather than as a collection of discrete molecules. This assumption holds true only when the characteristic length scale of the system is significantly larger than the average distance molecules travel between collisions, known as the mean free path, denoted by λ.

2.1.3.1 The Knudsen Number: A Measure of Continuum Validity

To quantify the validity of the continuum assumption, we use a dimensionless parameter called the *Knudsen number* (Kn)[3], defined as the ratio of the mean free path to the characteristic length scale of the system (L):

$$\mathrm{Kn} = \frac{\lambda}{L}. \tag{2.24}$$

Here, L typically represents the channel diameter or height. The value of the Knudsen number determines which physical description of the flow is appropriate. The flow is generally categorized into four regimes based on the value of Kn.

Continuum Flow Regime ($\mathrm{Kn} < 0.01$) In this regime, the characteristic length of the system is at least 100 times larger than the mean free path. Intermolecular collisions are

[3]The concept of the Knudsen number was introduced by Martin Knudsen in 1909 while studying rarefied gas dynamics.

far more frequent than collisions with the channel walls. The fluid behaves as a continuous medium, and the Navier–Stokes equations are fully valid. The standard no-slip boundary condition, which assumes the fluid velocity at the wall is zero, can be applied. This regime covers most microfluidic systems (typically with dimensions greater than 1 μm) and nanofluidic systems handling liquids, where the mean free path is extremely small (on the order of angstroms).

Slip-Flow Regime ($0.01 < \mathrm{Kn} < 0.1$) When the channel dimensions shrink, the region near the wall where the continuum assumption is weakest becomes significant. Molecules colliding with the wall may travel a considerable distance before colliding with another molecule, resulting in a non-zero fluid velocity at the surface. The Navier-Stokes equations are still applicable in the bulk of the fluid, but the continuum assumption breaks down near the boundary. The no-slip condition must be replaced with a *slip boundary condition*, which allows a finite velocity at the wall proportional to the shear rate at the surface.

Transition Flow Regime ($0.1 < \mathrm{Kn} < 10$) In this regime, the mean free path is comparable to the characteristic length scale of the system. Collisions between molecules and channel walls become as frequent as collisions between molecules. The fluid can no longer be treated as a continuum throughout the entire channel. The Navier-Stokes equations are no longer valid, and their solutions can lead to significant errors. Numerical methods are often used to simulate such systems.

Free Molecular Flow Regime ($\mathrm{Kn} > 10$) Here, the channel dimensions are much smaller than the mean free path. Intermolecular collisions are rare and can be neglected. The transport is dominated entirely by molecule-wall collisions. The continuum concept completely fails, and the Navier-Stokes equations are entirely inapplicable. The flow must be described by treating molecules individually.

For most liquid flows in micro- and nanochannels, the system operates in either the continuum ($\mathrm{Kn} < 0.01$) or slip-flow ($0.01 < \mathrm{Kn} < 0.1$) regimes. Therefore, the Navier–Stokes equations remain a valid framework, possibly with slip boundary conditions under very high confinement.

2.2 Governing Equation for Particle Motion

For a particle in a fluid, the equation of motion refers to Newton's second law applied to the particle, taking into account the forces affecting the motion of the particle. Depending on the level of complexity in describing particle dynamics, various approaches are presented in the literature, some of which are mentioned below.

2.2.1 Stokesian Dynamics

For a particle of mass m in a viscous fluid, its equation of motion can be written as:

$$\boldsymbol{m}\frac{d\boldsymbol{U}}{dt} = \boldsymbol{F}^{\mathrm{H}} + \boldsymbol{F}^{\mathrm{B}} + \boldsymbol{F}^{\mathrm{P}} \tag{2.25}$$

where $\boldsymbol{U}$ is the translational/rotational velocity vector of the particles, $\boldsymbol{F}^{\mathrm{H}}$ are the hydrodynamic forces. $\boldsymbol{F}^{\mathrm{B}}$ is the stochastic Brownian forces due to the thermal motion of fluid particles. $\boldsymbol{F}^{\mathrm{P}}$ is a non-hydrodynamic deterministic force, which may be any form of inter-particle or external force, for example, electric interaction between charged particles.

2.2.2 The Langevin Dynamics

In Langevin dynamics, the effect of the solvent is not directly taken into account. The damping term $-\gamma\boldsymbol{v}$ and the noise term $\boldsymbol{\xi}(t)$ take into account the effect of the solvent. In this approach, the hydrodynamic interactions are neglected. The equation of motion of a particle is given by:

$$m\frac{d^2\boldsymbol{r}}{dt^2} = -\nabla U(\boldsymbol{r},t) - \gamma\frac{d\boldsymbol{r}}{dt} + \sqrt{2\gamma k_B T}\boldsymbol{\xi}(t), \tag{2.26}$$

where $\boldsymbol{\xi(t)}$ represents the Gaussian white noise with zero mean and delta correlations, that is

$$\langle\boldsymbol{\xi}(t)\rangle = \mathbf{0} \qquad \text{and} \qquad \langle\xi_\alpha(t)\,\xi_\beta(t')\rangle = \delta_{\alpha\beta}\delta(t-t'). \tag{2.27}$$

Here:

- m is the mass of the particle.
- γ is the damping constant, in units of *mass/time.*
  - For spherical particles of radius r in the limit of low Reynolds number, Stokes law gives $\gamma = 6\pi\eta r$.

2.2.3 The Brownian Dynamics

In Brownian dynamics or the overdamped Langevin dynamics[4], the inertial force term is much smaller than the other forces and can be ignored. Which reduces the above equation to:

$$\mathbf{0} = -\nabla U(\boldsymbol{r}, t) - \gamma \frac{d\boldsymbol{r}}{dt} + \sqrt{2\gamma k_B T}\boldsymbol{\xi}(t). \tag{2.28}$$

Using Stokes-Einstein relation and defining the translational diffusion constant $D = \dfrac{k_B T}{\gamma}$, we get

$$\frac{d\boldsymbol{r}}{dt} = -\frac{1}{\gamma}\nabla U(\boldsymbol{r}, t) + \sqrt{2D}\boldsymbol{\xi}(t), \tag{2.29}$$

with

$$\langle \boldsymbol{\xi}(t) \rangle = \mathbf{0} \qquad \text{and} \qquad \langle \xi_\alpha(t)\, \xi_\beta(t') \rangle = \delta_{\alpha\beta}\delta(t - t'). \tag{2.30}$$

2.2.4 Characteristic Time Scales in Langevin Dynamics

(a) **Collision Duration (τ_{col}):** This is the time a single molecular collision lasts, i.e., the duration during which two molecules interact. It can be estimated as

$$\tau_{\text{col}} \sim \frac{\sigma}{v_{\text{th}}},$$

where σ is the molecular diameter and $v_{\text{th}} = \sqrt{3k_B T/m_{\text{mol}}}$ is the thermal speed. For water at room temperature:

$$\sigma \sim 3 \times 10^{-10}\,\text{m}, \quad v_{\text{th}} \sim 600\,\text{m/s} \Rightarrow \tau_{\text{col}} \sim 5 \times 10^{-13}\,\text{s}.$$

[4]Langevin himself referred to dropping inertia as "mathematically ugly but physically correct" for microscopic particles.

(b) **Mean Collision Time (τ_c):** The average time interval between two successive collisions. It is given by

$$\tau_c = \frac{\lambda}{v_{\text{th}}},$$

where λ is the mean free path. In liquids, $\lambda \sim \sigma$, so τ_c is of the same order as τ_{col}, typically

$$\tau_c \sim 10^{-12}\,\text{s}.$$

(c) **Noise Correlation Time (τ_ζ):** The random force $\zeta(t)$ has a finite correlation time approximately equal to the collision time:

$$\tau_\zeta \sim \tau_c.$$

In the Markov (white noise) approximation, one assumes $\tau_\zeta \to 0$.

(d) **Fluid (Hydrodynamic) Relaxation Time (τ_f):** The time for momentum to diffuse in the fluid over a distance equal to the particle size a:

$$\tau_f = \frac{\rho_f a^2}{\eta},$$

where ρ_f is the fluid density and η is its viscosity. For a particle of radius $a = 1\,\mu$m in water,

$$\tau_f \sim 10^{-6}\,\text{s}.$$

(e) **Velocity Relaxation Time (τ_v):** From the deterministic part of the Langevin equation,

$$m\frac{dv}{dt} = -\gamma v \quad \Rightarrow \quad v(t) = v_0 e^{-t/\tau_v},$$

with

$$\tau_v = \frac{m}{\gamma}.$$

This is the time over which the particle loses memory of its initial velocity. For a micron-sized particle in water,

$$\tau_v \sim 10^{-7}\,\text{s}.$$

(f) **Diffusion (Position Relaxation) Time (τ_D):** The time for a particle to diffuse a

distance comparable to its own radius:

$$\tau_D = \frac{a^2}{D},$$

where $D = k_B T/\gamma$ is the diffusion coefficient. For $a = 1\,\mu$m,

$$\tau_D \sim 1\,\text{s}.$$

Typical Hierarchy of Time Scales (for a 1 μm Particle in Water)

$$\tau_{\text{col}} \sim 10^{-13}\,\text{s} < \tau_c \sim 10^{-12}\,\text{s} < \tau_f \sim 10^{-6}\,\text{s} < \tau_v \sim 10^{-7}\,\text{s} \ll \tau_D \sim 1\,\text{s}.$$

The following table illustrates the various time scales and their corresponding values involved in particle dynamics.

Table 2.3: Characteristic time scales in particle dynamics along with their physical interpretations and typical magnitudes.

Time Scale	**Symbol**	**Typical Value**	**Meaning**
Collision duration	τ_{coll}	$10^{-13}\,\text{s}$	Duration of one molecular collision
Mean collision time	τ_c	$10^{-12}\,\text{s}$	Interval between collisions
Noise correlation	τ_ζ	$10^{-12}\,\text{s}$	Random force memory
Fluid relaxation	τ_f	$10^{-6}\,\text{s}$	Fluid inertia decay
Velocity relaxation	τ_v	$10^{-7}\,\text{s}$	Momentum relaxation
Diffusion time	τ_D	$1\,\text{s}$	Displacement $\sim a$

Physical Significance The Langevin equation assumes that many molecular collisions occur during any observable time interval, i.e., $\tau_c \ll t \ll \tau_v$. Thus, the random force can be treated as *white noise* with zero correlation time. In the **overdamped (Smoluchowski)** limit, when $t \gg \tau_v$, inertia is negligible.

This Langevin and Brownian dynamics framework is used to model tracer particle dynamics in fluctuating nanochannels in Chapter 3 and in the hydrodynamic ratchet model for undulating microchannel in Chapter 5.

2.3 The Statistical Description

Since the description of the particle motion is stochastic, it is natural to ask if there is a description evolving the probability density of the particle rather than the actual trajectory. This section introduces the Fokker-Planck equation as an alternative approach, studying the dynamics of the particle's probability density.

2.3.1 Fokker-Planck Equation

Since the overdamped equation for the motion of a Brownian particle is first-order, it describes the Markovian evolution of the particle's position, which is future-dependent only on the current state and not on the past. Let $P(x,t|x_0,t_0)$ denote the conditional probability density that the system is at position x at time t given that it started at x_0 at time t_0. The Markov property implies the following equation for the probability density, known as the Chapman-Kolmogorov equation

$$P(x_2,t_2|x_0,t_0) = \int_{-\infty}^{\infty} dx_1\, P(x_2,t_2|x_1,t_1)\, P(x_1,t_1|x_0,t_0), \tag{2.31}$$

for any intermediate time $t_0 < t_1 < t_2$. For convenience, let us use the probability distribution $P(x,t)$ to represent $P(x,t|x_0,t_0)$. That is

$$P(x,t) \equiv P(x,t|x_0,t_0). \tag{2.32}$$

Now write the Chapman-Kolmogorov equation over a small time increment δt:

$$P(x,t+\delta t) = \int_{-\infty}^{\infty} dx'\, P(x,t+\delta t|x',t)\, P(x',t). \tag{2.33}$$

Now writing

$$P(x,t+\delta t|x',t) = T(x|x';\delta t) \tag{2.34}$$

we get

$$P(x, t+\delta t) = \int_{-\infty}^{\infty} dx'\, T(x|x';\delta t)\, P(x', t), \tag{2.35}$$

where $T(x|x';\delta t)$ is the transition probability density from x' to x during δt.

For a continuous-time Markov jump process, we write

$$T(x|x';\delta t) = \left[1 - \delta t \int dy\, W(y|x')\right] \delta(x - x') + \delta t\, W(x|x') + O(\delta t^2), \tag{2.36}$$

where $W(x|x')$ is the transition rate per unit time from x' to x. Inserting into the Chapman-Kolmogorov equation and taking the limit $\delta t \to 0$ yields the **master equation**:

$$\frac{\partial}{\partial t} P(x,t) = \int_{-\infty}^{\infty} dx' \left[W(x|x')P(x',t) - W(x'|x)P(x,t)\right] \tag{2.37}$$

which expresses the gain and loss of probability from all other states. We now rewrite the master equation in terms of the jump size $r = x - x'$, so that $x' = x - r$:

$$\frac{\partial}{\partial t} P(x,t) = \int dr \left[w(x-r;r)\, P(x-r,t) - w(x;r)\, P(x,t)\right], \tag{2.38}$$

where $w(x;r) \equiv W(x+r|x)$ is the rate of jumps of size r. Assuming small jumps, we expand in a Taylor series:

$$w(x-r;r)\, P(x-r,t) = \sum_{n=0}^{\infty} \frac{(-r)^n}{n!} \frac{\partial^n}{\partial x^n} \left[w(x;r)P(x,t)\right]. \tag{2.39}$$

Inserting into the master equation gives the **Kramers–Moyal expansion**:

$$\frac{\partial}{\partial t} P(x,t) = \sum_{n=1}^{\infty} \frac{(-1)^n}{n!} \frac{\partial^n}{\partial x^n} \left[a_n(x)P(x,t)\right] \tag{2.40}$$

where the Kramers–Moyal coefficients are the conditional jump moments:

$$a_n(x) \equiv \int dr\, r^n w(x;r). \tag{2.41}$$

The Pawula theorem[5] states that a finite truncation of the Kramers–Moyal expansion is

[5]Pawula's theorem states that to preserve the positivity of the probability density, either the sequence $D_1,\ D_2,\ D_3 \ldots$ becomes zero at the third term, or all its even terms are positive.

mathematically consistent only if it ends at $n = 2$. Thus, we retain only the first two coefficients:

$$A(x) \equiv a_1(x), \qquad B(x) \equiv a_2(x),$$

representing the drift and diffusion coefficients, respectively. We then obtain the **Fokker-Planck equation**:

$$\frac{\partial}{\partial t}P(x,t) = -\frac{\partial}{\partial x}\big[A(x)P(x,t)\big] + \frac{1}{2}\frac{\partial^2}{\partial x^2}\big[B(x)P(x,t)\big] \tag{2.42}$$

which governs the time evolution of the probability density. Above equation corresponds to the following stochastic differential equation:

$$dX_t = A(X_t,t)\,dt + \sqrt{B(X_t,t)}\,dW_t, \tag{2.43}$$

where W_t is a Wiener process. Thus:

$$\text{SDE (trajectory view)} \quad \Longleftrightarrow \quad \text{Fokker-Planck equation (probability view).}$$

The overdamped Langevin equation for a Brownian particle moving in a potential $U(x,t)$ is

$$\frac{dx}{dt} = -\frac{1}{\gamma}\frac{\partial U(x,t)}{\partial x} + \sqrt{2D}\xi(t), \tag{2.44}$$

where γ is the friction coefficient and $\xi(t)$ is a Gaussian white noise with zero mean and delta correlations. Here $D = \dfrac{k_B T}{\gamma}$. The probability density $P(x,t)$ corresponding to the stochastic dynamics above evolves according to the Fokker-Planck equation

$$\frac{\partial P(x,t)}{\partial t} = -\frac{\partial}{\partial x}\left[-\frac{1}{\gamma}\frac{\partial U(x,t)}{\partial x}\,P(x,t)\right] + D\,\frac{\partial^2 P(x,t)}{\partial x^2}. \tag{2.45}$$

The Fokker–Planck formalism developed here is employed in Chapter 3 to derive the effective transport properties of particles in undulating nanochannels. The standard Fokker-Planck equation describes the time evolution of probability densities for overdamped systems where inertia is neglected. However, when inertial effects are important, the full phase space dynamics involving both position x and velocity v must be considered. This leads to the *Klein-Kramers equation*, also known as the *phase-space Fokker-Planck equation*.

We begin with the underdamped Langevin equation for a particle of mass m in a potential $U(x)$ subjected to viscous friction and thermal noise:

$$\dot{x} = v, \tag{2.46}$$

$$m\dot{v} = -\gamma v - \partial U(x,t)/\partial x + \sqrt{2\gamma k_B T}\,\xi(t), \tag{2.47}$$

where γ is the friction coefficient and $\xi(t)$ is Gaussian white noise with

$$\langle \xi(t) \rangle = 0, \qquad \langle \xi(t)\xi(s) \rangle = \delta(t-s).$$

The probability density $P(x, v, t)$ in phase space then satisfies the following phase space Fokker-Planck equation:

$$\frac{\partial P}{\partial t} = -\frac{\partial}{\partial x}(vP) + \frac{\partial}{\partial v}\left[\left(\frac{\partial U(x,t)/\partial x}{m} + \frac{\gamma}{m}v\right)P\right] + \frac{\gamma k_B T}{m^2}\frac{\partial^2 P}{\partial v^2} \tag{2.48}$$

This is the Klein-Kramers or underdamped Fokker-Planck equation.

At thermal equilibrium, $\partial_t P = 0$. The stationary solution must satisfy detailed balance and is given by the Maxwell–Boltzmann distribution:

$$P_{\mathrm{st}}(x, v) = \frac{1}{\mathcal{N}} \exp\left[-\frac{U(x)}{k_B T} - \frac{mv^2}{2k_B T}\right] \tag{2.49}$$

where $\mathcal{N}$ is the normalization constant. This factorizes naturally into a Boltzmann distribution in position and a Maxwellian distribution in velocity. In the strong friction limit ($\gamma \gg m$), velocity relaxes much faster than position. Eliminating v adiabatically yields the overdamped Langevin equation and the standard Fokker–Planck equation.

2.4 Basics of Stochastic Calculus

This section introduces the mathematical framework for studying Stochastic differential equations, their solutions, and their numerical simulations. We present a basic existence and uniqueness theorem for stochastic differential equations. We introduce the concept of the Wiener process and state its useful properties (without proof).

2.4.1 Stochastic Differential Equations (SDEs)

Stochastic differential equations extend ordinary differential equations by including stochastic (random) terms to model systems influenced by noise. Such equations are essential when the evolution of a system is subject to random fluctuations, for example, in the Brownian motion of colloidal particles in a fluid, the dynamics of molecules in a gas, or even in financial market fluctuations. One of the most studied stochastic differential equations in physics is the Langevin equation. A general SDE can be written in the form:

$$dX_t = a(X_t, t)\, dt + b(X_t, t)\, dW_t. \tag{2.50}$$

Here, a is known as drift and b represents the strength of noise. The term dW_t, which is equal to $W_{t+dt} - W_t$, is the increment of the Wiener process W_t. Let us briefly study what a Wiener process is and some of its properties to gain a better understanding of stochastic differential equations.

2.4.2 The Wiener Process (Mathematical Brownian Motion)

The Wiener process W_t[6] is characterized by the following properties:

- $W_0 = 0$ almost surely.[7] *(A Brownian particle is assumed to start from a well-defined initial position.)*
- It has independent increments: for every $t > 0$, the future increments $W_{t+u} - W_t$ for $u \geq 0$ are independent of the past values W_s for $s < t$. *(The particle's future motion does not depend on its past-memoryless random collisions lead to Markovian dynamics.)*
- It has Gaussian increments, i.e., for all $t \geq 0$ and $u \geq 0$,

$$W_{t+u} - W_t \sim \mathcal{N}(0, u).$$

[6] Norbert Wiener rigorously constructed Brownian motion in 1923, decades after Einstein and Smoluchowski derived its physical properties, a famous example of mathematics arriving later than physics.

[7] The phrase "almost surely" has a precise technical meaning in probability theory: an event occurs with probability 1. For our purposes, it is sufficient to interpret it as happening with certainty.

Here, $\mathcal{N}(0, u)$ denotes the normally distributed random variable with 0 mean and variance equal to u. *(Displacements over any time interval arise from a large number of microscopic collisions, giving Gaussian statistics via the central limit theorem.)*

- It has almost surely continuous paths; that is, W_t is almost surely continuous in t. *(The particle does not teleport or jump-its position changes continuously, consistent with physical motion in space.)*

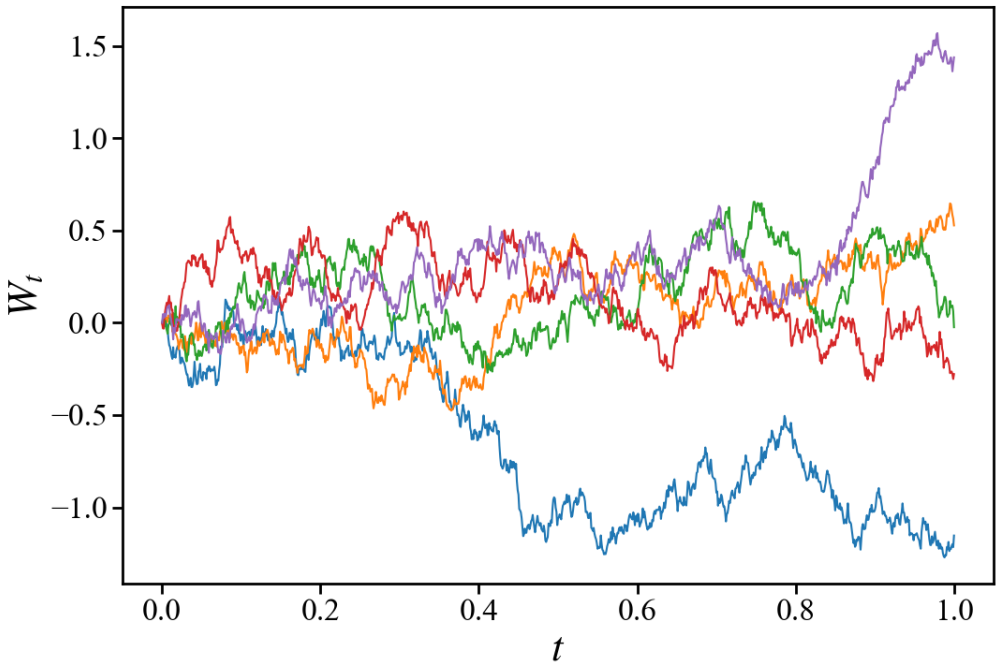

Figure 2.1: Five different realizations of the Wiener process

Figure 2.1 shows the five different realizations of the Wiener process. The paths of the Wiener process exhibit many counterintuitive properties, unlike the smooth and regular functions encountered in physics. To highlight the mathematical nature of the paths of Brownian motion, we state some of the properties of the Wiener process without proof. These properties underline why classical calculus fails for Brownian motion and motivate the development of stochastic calculus for stochastic differential equations.

- For every $\varepsilon > 0$, the function W_t takes strictly positive and strictly negative values in the interval $(0, \varepsilon)$. *(A Brownian particle immediately explores both sides of its initial position, reflecting the unbiased nature of thermal noise.)*

- The function W_t is continuous everywhere but differentiable nowhere (similar to the Weierstrass function). *(Particle trajectories do not possess well-defined instantaneous velocities-a key departure from the deterministic trajectories.)*

- For any $\varepsilon > 0$, W_t is almost surely not $\left(\frac{1}{2} + \varepsilon\right)$-Hölder continuous, and almost surely $\left(\frac{1}{2} - \varepsilon\right)$-Hölder continuous. *(The motion exhibits strong small-scale roughness, consistent with rapid, random collisions with surrounding molecules.)*

- The Points at which W_t takes local maximum form a dense countable set; the maximum values are pairwise distinct. Each local maximum is sharp in the following sense: if W_t has a local maximum at t, then

$$\lim_{s \to t} \frac{|W_s - W_t|}{|s - t|} = \infty.$$

  The same holds for local minima. *(Brownian trajectories exhibit infinitely sharp, jagged turning points, consistent with continual momentum randomization.)*

- The function W_t has no points of local increase; that is, no $t > 0$ follows the condition for a sustained monotonic rise. The same holds for local decrease. *(There are no smooth trends-a particle cannot maintain motion in one direction without being rapidly scattered.)*

- The function W_t is of unbounded variation on every interval. *(The total length of the Brownian trajectory is effectively infinite - the particle takes arbitrarily many tiny zig-zag steps.)*

- The quadratic variation of W_t over $[0, t]$ is t. *(This is the fundamental origin of diffusion scaling: $\langle W_t^2 \rangle = t$, or equivalently, $\langle x^2 \rangle \propto t$-a central result in statistical mechanics. Here $\langle \dots \rangle$ denotes the ensemble averaging notation. For a nice discussion about various types of averaging, the reader is advised to refer to Appendix A.)*

- The zeros of W_t form a nowhere dense perfect set of Lebesgue measure zero and Hausdorff dimension $\frac{1}{2}$. *(A particle returns infinitely often to its starting position, but the set of such return times is highly irregular, reflecting recurrent diffusion.)*

- **Law of the iterated logarithm** Almost surely,

$$\limsup_{t \to +\infty} \frac{|W_t|}{\sqrt{2t \log \log t}} = 1.$$

(Brownian displacement grows roughly like $\sqrt{t}$ but exhibits occasional rare but statistically predictable large excursions.)

Basic and Deducible Properties of Wiener Process (W_t)

1. **Distribution at fixed time:**

$$f_{W_t}(x) = \frac{1}{\sqrt{2\pi t}} e^{-x^2/(2t)}, \quad \text{i.e., } W_t \sim \mathcal{N}(0, t).$$

2. **Expectation:** $\langle W_t \rangle = 0$.

3. **Variance:** $\mathrm{Var}(W_t) = t$.

4. **Decomposition:** For $s \leq t$,

$$W_t = W_s + (W_t - W_s),$$

where the increment $(W_t - W_s)$ is independent of W_s and normally distributed as $\mathcal{N}(0, t - s)$.

5. **Covariance and correlation:** For $s \leq t$,

$$\mathrm{Cov}(W_s, W_t) = \min(s, t) = s, \qquad \mathrm{Corr}(W_s, W_t) = \frac{s}{\sqrt{s\,t}} = \sqrt{\frac{s}{t}}.$$

6. **Increment relation for simulation:** For $t_1 < t_2$,

$$W_{t_2} = W_{t_1} + \sqrt{t_2 - t_1}\, Z,$$

where $Z \sim \mathcal{N}(0, 1)$ is independent of W_{t_1}.

7. **Scale invariance:** If W_t is a Wiener process then for any nonzero constant α, $\alpha^{-1} W_{\alpha^2 t}$ is also Wiener process.

8. **Time reversal:** The process $V_t = W_{1-t} - W_1$ for $0 \leq t \leq 1$ is distributed like W_t for $0 \leq t \leq 1$.

9. **Time Inversion:** The process $V_t = t W_{1/t}$ is also distributed like W_t.

2.4.3 Numerical Solution of SDEs

Stochastic differential equations play a crucial role in modeling physical systems across various disciplines, including physics and chemistry. Unlike ordinary differential equations, linear stochastic equations sometimes do not allow closed-form solutions, except in a few instances (such as the Ornstein–Uhlenbeck process and geometric Brownian motion). The functional form of the coefficients in the stochastic differential equation determines whether the SDE admits a solution or not, and if the solution exists, is it unique? (For a friendly introduction about the existence and uniqueness theorem of SDE, the reader is advised to refer to Appendix D). Therefore, in most cases, one must rely heavily on numerical schemes to solve stochastic differential equations. We present two of the simplest and most commonly used numerical schemes for solving stochastic differential equations below, namely the Euler–Maruyama method and the stochastic Heun method.

Euler-Maruyama Method The Euler-Maruyama method is the simplest numerical method used to approximate the solution of a stochastic differential equation (SDE). This method is a generalization of the Euler method for ordinary differential equations to stochastic differential equations. It is named after Leonhard Euler and Gisiro Maruyama. Consider the following stochastic differential equation.

$$dX_t = a(X_t, t)\ dt + b(X_t, t)\ dW_t, \tag{2.51}$$

with $X_0 = x_0$ and W_t denotes the standard Wiener process. To solve the above stochastic differential equation numerically in the time interval $[0, T]$, we define a Markov chain[8] Y that approximates the true solution X_t.

- First, divide the time interval $[0, T]$ into N equal subintervals of width δt:

$$0 = t_0 < t_1 < t_2 < \cdots < t_N = T, \qquad \delta t = \frac{T}{N}.$$

- Set the initial condition:

$$Y_0 = x_0.$$

[8] A Markov chain is a stochastic process in which the future state depends only on the present state and not on the full history of the process.

- Define the Markov chain:

$$Y_{n+1} = Y_n + a(Y_n, t_n)\,\delta t + b(Y_n, t_n)\,\delta W_n,$$

where

$$\delta W_n = W_{t_{n+1}} - W_{t_n} \sim \mathcal{N}(0, \delta t), \qquad \delta t = t_{n+1} - t_n = T/N.$$

Then Y_n approximates the true solution $X_{t=t_n}$.

Stochastic Heun Method The stochastic Heun method is an extension of Heun's method for ordinary differential equations. This method is an improvement over the Euler-Maruyama method. The stochastic Heun method is a type of predictor-corrector method. Consider the following stochastic differential equation:

$$dX_t = a(X_t, t)\ dt + b(X_t, t)\ dW_t \tag{2.52}$$

with $X_0 = x_0$ and W_t is the standard Wiener process. The algorithm to numerically integrate SDE is as:

- First, divide the time interval $[0, T]$ into N equal subintervals of width δt:

$$0 = t_0 < t_1 < t_2 < \cdots < t_N = T, \qquad \delta t = \frac{T}{N}.$$

- Set the initial condition:

$$Y_0 = x_0.$$

- Define the Markov chain:

$$\tilde{Y}_n = Y_n + a(Y_n, t_n)\,\delta t + b(Y_n, t_n)\,\delta W_n,$$

$$Y_{n+1} = Y_n + \tfrac{1}{2}\left\{a(Y_n, t_n) + a(\tilde{Y}_n, t_{n+1})\right\}\,\delta t + \tfrac{1}{2}\left\{b(Y_n, t_n) + b(\tilde{Y}_n, t_{n+1})\right\}\,\delta W_n.$$

In the case of additive noise (when b is constant), the scheme simplifies to

$$Y_{n+1} = Y_n + \tfrac{1}{2}\left\{a(Y_n, t_n) + a(\tilde{Y}_n, t_{n+1})\right\}\,\delta t + b\,\delta W_n,$$

where

$$\delta W_n = W_{t_{n+1}} - W_{t_n} \sim \mathcal{N}(0, \delta t).$$

Convergence of Numerical Schemes When we solve ordinary differential equations using numerical methods, we require that the numerical solution approaches the exact trajectory as the time step of the simulation becomes increasingly smaller, a phenomenon known as convergence. But for stochastic differential equations, because of the randomness involved, we care about two different goals:

1. We may demand the average of the difference between the numerical solution and the exact trajectory at any time t to go to zero in the limit of small time steps. This is known as *strong convergence*. Mathematically, we demand

$$\langle |X_t - Y_t| \rangle \to 0 \quad \text{as} \quad \delta t \to 0. \tag{2.53}$$

2. If, on the other hand, we demand the difference of the average values of some observable, say ϕ, to go to zero as the time step goes to zero, then this is known as *weak convergence*. Mathematically,

$$\big|\langle \phi(X_t) \rangle - \langle \phi(Y_t) \rangle\big| \to 0 \quad \text{as} \quad \delta t \to 0. \tag{2.54}$$

Strong convergence implies weak convergence, but the opposite is not always true.

Order of Convergence The order of convergence of a numerical method indicates how fast the numerical method solution approaches the exact solution as the time step δt becomes smaller. A method with strong order γ satisfies

$$\langle |X_T - Y_T| \rangle = O\left((\delta t)^\gamma\right) \quad \text{as} \quad \delta t \to 0, \tag{2.55}$$

which measures how well individual sample paths are approximated.

Similarly, a method with weak order β satisfies

$$|\langle \phi(X_T) \rangle - \langle \phi(Y_T) \rangle| = O\left((\delta t)^\beta\right) \quad \text{as} \quad \delta t \to 0, \tag{2.56}$$

which measures how well the probability distribution of the exact solution is captured. Thus, higher-order methods yield smaller errors for the same time step size, and strong convergence implies weak convergence, but not vice versa.

Table 2.4: Comparison of strong and weak convergence orders for two commonly used numerical schemes for stochastic differential equations. Higher orders indicate faster decay of the numerical error as the timestep decreases.

Numerical Method	**Strong Order**	**Weak Order**
Euler–Maruyama Method	$\frac{1}{2}$	1
Stochastic Heun Method	1	2

Higher-order methods, such as stochastic Runge-Kutta, e.g., stochastic RK4, also exist in the literature.

For the standard Langevin equation given below

$$\frac{dx}{dt} = \frac{1}{\gamma}F(x,t) + \sqrt{2D(x,t)}\xi(t), \tag{2.57}$$

the numerical Euler-Maruyama scheme can be derived as: The Langevin equation given above can be written in terms of a stochastic differential equation as:

$$dX_t = F(X_t,t)\ dt + \sqrt{2D(X_t,t)}\ dW_t \tag{2.58}$$

where $dW_t = \xi(t)\ dt$ and

$$\xi(t) = \frac{dW_t}{dt}. \tag{2.59}$$

To numerically solve the Langevin equation, the Euler-Maruyama algorithm, which can be easily derived from the above stochastic differential equation solution algorithm, is:

$$\delta X_t = F(X_t,t)\delta t + \sqrt{2D(X_t,t)}\delta W_t \tag{2.60}$$

Since $\delta W_t = W_{t+\delta t} - W_t \sim \mathcal{N}(0,\delta t) = \sqrt{\delta t}\mathcal{N}(0,1)$, we have

$$X_{t+\delta t} = X_t + F(X_t,t)\delta t + \sqrt{2D(X_t,t)\delta t}\ \mathcal{N}(0,1) \tag{2.61}$$

The above equation can be used directly to numerically integrate the Langevin equation.

Using the properties of the Wiener process W_t, we can deduce the following property[9] of the Gaussian white noise $\xi(t)$

$$\langle \dot{W}_t \dot{W}_s \rangle = \frac{\partial}{\partial t}\frac{\partial}{\partial s}\langle W_t W_s \rangle = \frac{\partial}{\partial t}\frac{\partial}{\partial s}\min(t,s) = \delta(t-s). \tag{2.62}$$

Generation of Gaussian Random numbers In most programming languages, such as `C++` and `Fortran`, inbuilt Gaussian random number generators are not available. Thus, we use indirect techniques to generate Gaussian random numbers. One of the most commonly used techniques is known as the Box-Muller transform[10]. It is commonly used to generate normally distributed random numbers from uniformly distributed random numbers. Suppose U_1 and U_2 are independent random variables uniformly distributed in the interval $(0, 1)$, i.e.,

$$U_1 \sim \text{Uniform}(0,1), \qquad U_2 \sim \text{Uniform}(0,1).$$

Then write,

$$Z_1 = \sqrt{-2\ln U_1}\cos(2\pi U_2), \tag{2.63}$$

and

$$Z_2 = \sqrt{-2\ln U_1}\sin(2\pi U_2). \tag{2.64}$$

Then Z_1 and Z_2 are independent random variables following the standard normal distribution. That is,

$$Z_1 \sim \mathcal{N}(0,1) \qquad \text{and} \qquad Z_2 \sim \mathcal{N}(0,1).$$

Polar Form The polar form of the Box–Muller transform, also known as the Marsaglia polar method, is an alternative and computationally more efficient way of generating Gaussian-distributed random numbers. Unlike the standard Box–Muller transform, which involves evaluating trigonometric functions, the polar method eliminates the need for such operations. In this approach, two independent uniformly distributed random numbers U_1 and U_2

[9] In physics, Gaussian white noise $\xi(t)$ is often used formally with $\langle \xi(t)\xi(s)\rangle = \delta(t-s)$. However, such white noise is not a well-defined function in the classical sense; it is mathematically understood as a generalized function that represents the formal time derivative of a Wiener process: $\xi(t) = \frac{dW_t}{dt}$. For this reason, mathematicians prefer to work directly with the Wiener process W_t, which is rigorously defined.

[10] George Box and Mervin Muller devised this transformation in 1958 while discussing Monte Carlo simulations over drinks at a conference.

in the interval $(-1, 1)$ are generated, and the quantity $S = U_1^2 + U_2^2$ is computed. If $S \geq 1$ or $S = 0$, the pair is rejected and new values of U_1 and U_2 are generated. For accepted pairs, the normally distributed random variables are obtained as

$$Z_1 = U_1 \sqrt{\frac{-2 \ln S}{S}}, \qquad Z_2 = U_2 \sqrt{\frac{-2 \ln S}{S}}.$$

The variables Z_1 and Z_2 are independent and follow the standard normal distribution, that is $Z_1, Z_2 \sim \mathcal{N}(0, 1)$. Since the polar method avoids the computational cost of trigonometric evaluations, it is generally faster and more suitable for numerical simulations in programming languages, where built-in Gaussian random number generators are not always available. Despite being based on a rejection scheme, the method remains highly efficient because only about 21% of the generated pairs are typically discarded. For a historical account of the Box–Muller method and its variants, the reader is referred to [72, 73, 74].

2.5 Summary

In summary, this chapter has introduced the theoretical and computational tools required for the analysis of fluid and particle transport in confined geometries. The Navier–Stokes framework developed here is applied to derive flow fields in Chapters 4 and 5, while the stochastic descriptions based on Langevin and Fokker–Planck equations are used to analyze particle transport and ratcheting phenomena in Chapters 3 and 5.

3

An Entropic Flashing Ratchet for Particle Transport

In the previous chapter, we established the mathematical and computational framework for analyzing particle transport, including the Langevin and Fokker-Planck equations. We now apply this framework to investigate a specific, biologically-inspired mechanism for generating directed transport: an entropic ratchet.

Marbach et al. developed a foundational method for analyzing particle transport in undulating nanochannels [47]. Their work, which utilizes the lubrication approximation, captures the 'diffusivity renormalization' of a test particle and provides the essential tools for this analysis. In the present chapter, we will use the relations they derived to model the overdamped dynamics of a test particle. We will demonstrate that by introducing a local inversion-asymmetric surface fluctuation, we can induce a ratcheting effect.

This chapter numerically explores ratcheting in nano-meter-sized tubes (about 100 nm radius) with flexible confining surfaces. The goal is to demonstrate that for specific surface undulations (wavelength of approximately 400 nm, amplitude of approximately 20 nm), particles of approximately 10 nm in size can achieve a significant ratcheting velocity (several hundred nanometers per second) at room temperature. We will also demonstrate that this mechanism is highly adjustable, allowing for velocity reversal by tuning the surface modes. This result is significant, as it indicates a mechanism for filtering particles that are much smaller than the pore radius of the nanochannel.

The contents of this chapter are based on the work [75]. First, we present the salient steps of the calculations by Marbach et al. [47] to derive the general velocity dynamics. We then demonstrate how these overdamped dynamics lead to ratcheting in the presence of an inversion-symmetry-broken surface patterning. Finally, we present the detailed numerical results of this ratcheting process and conclude with a discussion of the model.

3.1 Theoretical Foundation: Effective Particle Dynamics in Fluctuating Nanochannels

For the sake of completeness in the presentation, we first present the basic analysis as done by Marbach et al. [47] to set up the stage for the analysis of ratcheting. The dynamics of probability density $p(\boldsymbol{r},t)$ of a tracer particle in the presence of velocity field $\boldsymbol{u}(\boldsymbol{r}$,t) is governed by the Fokker-Planck equation

$$\frac{\partial p(\boldsymbol{r},t)}{\partial t} = D_0 \nabla^2 p(\boldsymbol{r},t) - \nabla \cdot [\boldsymbol{u}(\boldsymbol{r},t) p(\boldsymbol{r},t)]. \tag{3.1}$$

In Fig. 3.1, we have shown the geometry of a nanochannel with an undulating upper surface. Let $h_u(\boldsymbol{x},t)$ be the upper surface profile, where $\boldsymbol{x} = (x,\ y)$ is the coordinate of the 2D plane at a fixed height z and $h_u(\boldsymbol{x},t) = H + h(\boldsymbol{x},t)$. Where H is the mean height of an upper fluctuating surface and $h(\boldsymbol{x},t)$ is the height variation over the mean height. Here, the lower surface confining the fluid layer is considered to be fixed without any loss of generality. Therefore z lies between 0 and $h_u(\boldsymbol{x},t)$. The marginal probability distribution function $p^*(\boldsymbol{x},t)$ is then defined as :

$$p^*(\boldsymbol{x},t) = \int_0^{h_u(\boldsymbol{x},t)} dz\, p(\boldsymbol{r},t). \tag{3.2}$$

Now integrating both sides of the Fokker-Planck Eq. 3.1 from 0 to $h_u(\boldsymbol{x},t)$ while using the Leibnitz rule and then simplifying, one obtains an equation for the marginal probability distribution as

$$\frac{\partial p^*(\boldsymbol{x},t)}{\partial t} = D_0 \nabla_{||}^2 p^*(\boldsymbol{x},t) - \nabla_{||} \cdot [\boldsymbol{v}(\boldsymbol{x},t) p^*(\boldsymbol{x},t)], \tag{3.3}$$

where

$$\nabla_{||} = \hat{i}\frac{\partial}{\partial x} + \hat{j}\frac{\partial}{\partial y}, \tag{3.4}$$

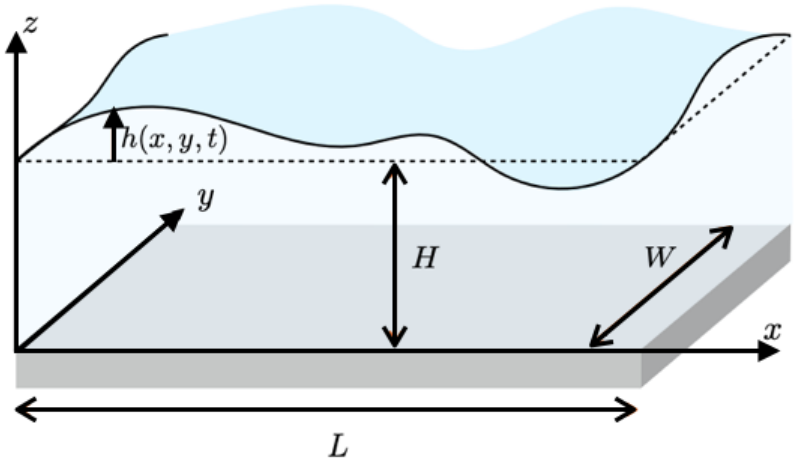

Figure 3.1: Schematic of a nanochannel with surface undulations $h(x, y, t)$. The average height of the undulating surface is denoted by H. The channel extends along the x-axis, while the height is measured along the z-axis. Source: Adapted from. [47]

$$\nabla_{||}^2 = \frac{\partial^2}{\partial x^2} + \frac{\partial^2}{\partial y^2}, \tag{3.5}$$

and

$$\boldsymbol{v}(\boldsymbol{x}, t) = D_0 \frac{\nabla_{||} h(\boldsymbol{x}, t)}{h_u(\boldsymbol{x}, t)} + \frac{1}{h_u(\boldsymbol{x}, t)} \int_0^{h_u(\boldsymbol{x},t)} dz\, \boldsymbol{u}_{||}(\boldsymbol{r}, t) \tag{3.6}$$

is the effective velocity field that a tracer particle experiences. Equation 3.6 for the effective velocity will be important for later discussions. In deriving Eq. 3.6, one makes use of the following boundary conditions.

1. Kinematic Boundary condition: It implies that the velocity of the fluid at the boundary is zero with respect to the boundary.

$$u_z(\boldsymbol{x}, h_u(\boldsymbol{x}, t), t) - \frac{\partial}{\partial t} h_u(\boldsymbol{x}, t) - \boldsymbol{u}_{||}(\boldsymbol{x}, h_u(\boldsymbol{x}, t), t) \cdot \nabla_{||} h_u(\boldsymbol{x}, t) = 0. \tag{3.7}$$

   Here $(\nabla_{||}, \frac{\partial}{\partial z})$ and $(\boldsymbol{u}_{||}, u_z)$ denote in-plane and out-of-plane coordinates, respectively.

2. Conservation of probability at $z = 0$:

$$\frac{\partial}{\partial z} p(\boldsymbol{x}, z = 0) = 0. \tag{3.8}$$

3. Conservation of probability at $z = h_u(\boldsymbol{x}, t)$:

$$\nabla p(\boldsymbol{x}, z)|_{z=h_u(\boldsymbol{x},z)} \cdot \boldsymbol{n} = 0. \tag{3.9}$$

Now we will briefly sketch the derivation of Eq. 3.3 and 3.6. Integrating Eq. 3.1 from 0 to $h_u(\mathbf{x}, t)$ and using the above three boundary conditions, one obtains the following equation for marginal probability density $p^*(\boldsymbol{x}, t)$:

$$\frac{\partial}{\partial t}p^*(\boldsymbol{x}, t) = D_0\, \nabla_\parallel^2 p^*(\boldsymbol{x}, t) - D_0\, \nabla_\parallel \cdot \big[\, p\big(\boldsymbol{x}, h_u(\boldsymbol{x}, t), t\big)\, \nabla_\parallel h_u(\boldsymbol{x}, t)\big] \\ - \nabla_\parallel \cdot \int_0^{h_u(\boldsymbol{x},t)} dz\; \boldsymbol{u}_\parallel\big(\boldsymbol{r}, t\big)\, p\big(\boldsymbol{r}, t\big). \tag{3.10}$$

But this equation is not in terms of marginal probability density $p^*(\boldsymbol{x}, t)$ only. It also contains terms involving $p(\mathbf{r}, t)$. However, if one makes use of the Lubrication approximation [1] as is shown by Marbach et al. [47], then one can assume the equilibrium in the z direction and that it is uniformly distributed. Then, using the normalization, one can write $p(\boldsymbol{x}, z, t) \approx f(\boldsymbol{x}, t)$. This relation greatly simplifies the above equation, and one gets:

$$p^*(\boldsymbol{x}, t) \approx \int_0^{h_u(\boldsymbol{x},t)} dz\; f(\boldsymbol{x}, t) = h_u(\boldsymbol{x}, t) f(\boldsymbol{x}, t). \tag{3.11}$$

Therefore we have the following equation for marginal probability density $p^*(\boldsymbol{x}, t)$:

$$\frac{\partial}{\partial t}p^*(\boldsymbol{x}, t) = D_0 \nabla_\parallel^2 p^*(\boldsymbol{x}, t) - D_0 \nabla_\parallel \cdot \Big[\, p^*(\boldsymbol{x}, t), t)\, \nabla_\parallel \ln(h_u(\boldsymbol{x}, t))\, \Big] \\ - \nabla_\parallel \cdot \Big[\, p^*(\boldsymbol{x}, t)\, \overline{\boldsymbol{u}}_\parallel(\boldsymbol{x}, t)\, \Big], \tag{3.12}$$

[1] The use of the lubrication approximation is justified based on the geometric and dynamical parameters of the system. The characteristic channel height in our model is $H \sim 100\,\text{nm}$ and the axial length scale is given by the wavelength of surface undulations which in our model is $L \sim 400\,\text{nm}$, yielding an aspect ratio $\epsilon = H/L \sim 0.25$, corresponding to a moderately slender geometry.

The wall profile varies smoothly, with a typical slope $|\partial h/\partial x| \sim k\delta h \sim 0.1$, where $\delta h \sim 10\,\text{nm}$ is the amplitude of surface undulations. This satisfies the small-slope requirement underlying the lubrication approximation.

Furthermore, the Reynolds number is extremely small, $\text{Re} \sim 10^{-7}$, indicating that the flow is strongly dominated by viscous forces. Taken together, these estimates justify the use of the lubrication approximation as a leading-order description of the flow in the present system.

where $\overline{\boldsymbol{u}}_{||}(\boldsymbol{x},t)$ is average velocity defined by:

$$\overline{\boldsymbol{u}}_{||}(\boldsymbol{x},t) = \frac{1}{h_u(\boldsymbol{x},t)} \int_0^{h_u(\boldsymbol{x},t)} dz\, \boldsymbol{u}_{||}(\boldsymbol{x},z,t). \tag{3.13}$$

Finally, the following equation is obtained for the marginal probability density

$$\frac{\partial p^*(\boldsymbol{x},t)}{\partial t} = D_0 \nabla_{||}^2 p^*(\boldsymbol{x},t) - \nabla_{||}.[\boldsymbol{v}(\boldsymbol{x},t) p^*(\boldsymbol{x},t)], \tag{3.14}$$

where

$$\boldsymbol{v}(\boldsymbol{x},t) = D_0 \frac{\nabla_{||} h(\boldsymbol{x},t)}{h_u(\boldsymbol{x},t)} + \frac{1}{h_u(\boldsymbol{x},t)} \int_0^{h_u(\boldsymbol{x},t)} dz\, \boldsymbol{u}_{||}(\boldsymbol{r},t) \tag{3.15}$$

is the effective velocity field with which the tracer particle is moving.

Let us examine the above equation more closely to understand the necessity of invoking the ratcheting mechanism in this context. The first term on the RHS of this equation is proportional to the gradient of the surface fluctuation at a point in space at an instant of time and is of entropic origin. The gradient of surface fluctuations is, in general, a function of space and time and does not result in a unidirectional transport. This is exactly why the ratcheting mechanism is needed for a sustained directed transport of particles against the hydrodynamic flow in such systems. For simplicity, we will consider the motion of a tracer particle in a one-dimensional nanochannel. In one dimension, the equation for marginal probability density and effective velocity becomes:

$$\frac{\partial p^*(x,t)}{\partial t} = D_0 \frac{\partial^2 p^*(x,t)}{\partial x^2} - \frac{\partial}{\partial x}\big(v(x,t) p^*(x,t)\big), \tag{3.16}$$

$$v(x,t) = D_0 \frac{\frac{\partial}{\partial x} h(x,t)}{h_u(x,t)} + \frac{1}{h_u(x,t)} \int_0^{h_u(x,t)} u_{\parallel}(x,z,t)\, dz. \tag{3.17}$$

Fig. 3.2 shows a schematic of a nanochannel, illustrating only the x direction for simplicity. Now, a tracer particle in a nanochannel with height undulations given by $h_u(x,t)$ in the presence of a velocity field represented by Eq. 3.6 follows the following Langevin equation:

$$\frac{dx}{dt} = v(x,t) + \sqrt{2D_0}\xi(t), \tag{3.18}$$

where D_0 is the diffusion constant (and is given by $D_0 = \frac{k_B T}{6\pi\eta r}$ using the Stokes-Einstein relation) of the tracer particle, and $\xi(t)$ is Gaussian white noise with zero mean and delta

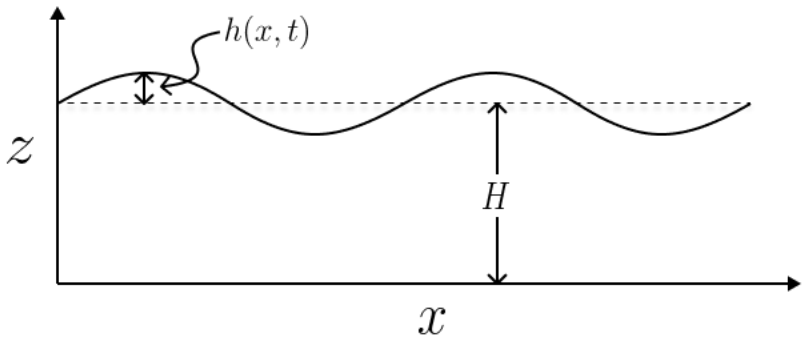

Figure 3.2: Schematic of a 1D nanochannel with surface undulations $h(x,t)$. The average height of the undulating surface is denoted by H. The channel extends along the x-axis, while the height is measured along the z-axis.

correlations. That is,

$$\langle \xi(t) \rangle = 0, \tag{3.19}$$

$$\langle \xi(t)\, \xi(t') \rangle = \delta(t - t'). \tag{3.20}$$

3.2 The Entropic Ratchet Model

Let us examine how surface fluctuations induced ratcheting can occur in nanofluid systems. Under the lubrication approximation, the velocity of the diffusing particle is

$$\frac{dx}{dt} = D_0 \frac{\frac{\partial}{\partial x} h(x,t)}{H + h(x,t)} + \frac{1}{H + h(x,t)} \int_0^{H+h(x,t)} dz\, u(x,z,t), \tag{3.21}$$

where we have considered only one of the planar coordinates (x, y) for simplicity. In the above equation, there are two terms on the RHS of which the first term gives the average velocity induced by diffusion and surface gradients, and the second term stands for the

advection of the particle by the fluid of velocity $u(x, z, t)$. If the first term can produce a velocity that is opposite in direction to the second term and can overcome the advection, then the particle can actually move in the opposite direction to the fluid flow, resulting in enhanced filtration. However, this will require a breaking of inversion symmetry at smaller scales.

To have an understanding of the surface-driven ratcheting phenomenon, for the sake of simplicity, let us drop the advection part from Eq. 3.21 and plug in a stochastic noise of strength consistent with the diffusivity D_0. We employ the simplest model here for analysis to primarily investigate the role of the surface fluctuation-driven entropic force term in the possible ratcheting phenomenon, and if so, whether that ratcheting could be a significant contributor to particle transport. Thus, in the presence of diffusive coupling along with Gaussian white noise with zero mean and unit variance position of the particle obeys the following Stochastic differential equation :

$$\frac{dx}{dt} = \frac{D_0}{H}\frac{\partial}{\partial x}h(x,t) + \sqrt{2D_0}\,\xi(t). \tag{3.22}$$

We have gone by the assumption $H \gg h(x,t)$, which is the lubrication approximation. The $\xi(t)$ is Gaussian white noise with zero mean, unit variance, and delta correlations. Comparing the above equation with the standard overdamped Langevin equation:

$$\frac{dx}{dt} = -\frac{1}{\gamma}\frac{\partial V(x,t)}{\partial x} + \sqrt{2D_0}\xi(t) \tag{3.23}$$

Therefore, we have,

$$-\frac{1}{\gamma}\frac{\partial V(x,t)}{\partial x} \leftrightarrow \frac{D_0}{H}\frac{\partial h(x,t)}{\partial x} \tag{3.24}$$

with $D_0 = \frac{k_B T}{\gamma}$. Thus, the equation for the tracer particle is the overdamped dynamics of a particle in the potential $-\frac{D_0}{H}h(x,t)$. Thus, the height undulations act as a potential landscape for the motion of the tracer particle in the nanochannel. The potential experienced by the tracer particle is:

$$V(x,t) = -\frac{k_B T}{H}h(x,t). \tag{3.25}$$

We model surface undulations $h(x,t)$ by the superposition of two traveling waves moving in

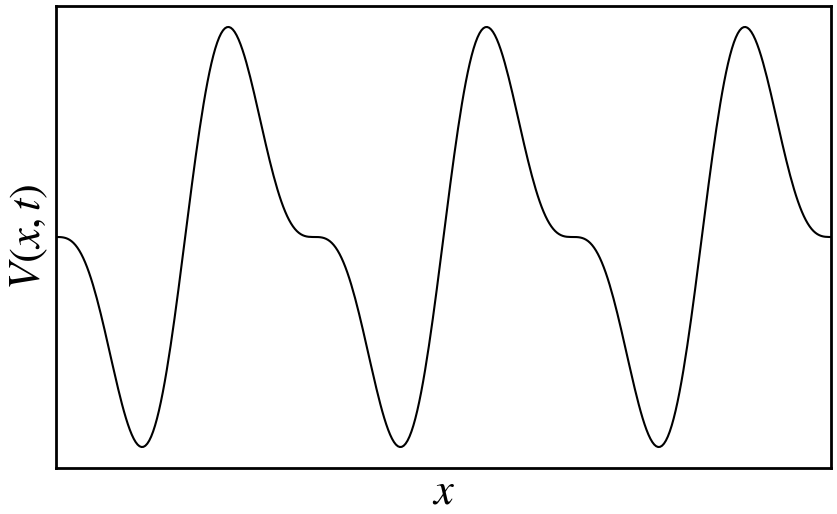

Figure 3.3: Snapshot of ratcheting undulations showing the broken inversion symmetry

opposite directions with frequency ω and wave number k.

$$h(x,t) = h_0 \, \sin(\omega_0 t + \phi) \left[\sum_{n=1}^{2} (-1)^n \frac{\sin(\omega t + nkx)}{n} - \sum_{n=1}^{2} (-1)^n \frac{\sin(\omega t - nkx)}{n} \right]. \tag{3.26}$$

Each of the individual waves is nothing but the two-term truncation of a Fourier series of a saw-tooth profile. The first term of $h(x,t)$ provides a global oscillation with frequency ω and phase ϕ. This particular $h(x,t)$ profile provides the essential ingredient of ratcheting, i.e., breaking of inversion symmetry. In Fig. 3.3, we have plotted the $h(x,t)$ profile at an instant showing broken symmetry. After simplifying the above expression for $h(x,t)$ using trigonometric identities, one can obtain the following expression for $h(x,t)$:

$$h(x,t) = h_0 \, \sin(\omega t + \phi) \left[\cos(\omega t) \, \sin(2kx) - 2 \cos(\omega t) \, \sin(kx) \right] \tag{3.27}$$

$$= h_0 \, \sin(\omega t + \phi) \cos(\omega t) \left[\sin(2kx) - 2 \sin(kx) \right]. \tag{3.28}$$

The term in square brackets,

$$\sin(2kx) - 2\sin(kx),$$

defines the spatial shape of the driving potential. The numerical coefficient (here, the factor 2) controls the relative weight of the first and second spatial harmonics. Changing this coefficient breaks the left-right symmetry of the potential, thereby producing an asymmetric

profile. In general,

$$\sin(2kx) - A\,\sin(kx),$$

generates a family of asymmetric periodic potentials, where $A = 2$ gives a moderately asymmetric potential, while choosing a larger value (e.g. $A = 4$) increases the steepness of one side of the potential and enhances the rectification ability of the ratchet. After substituting the expression for $h(x,t)$ in Eq. 3.22, one can obtain the following Stochastic equation of motion for a particle :

$$\frac{dx}{dt} = 2kD_0\frac{h_0}{H}\,\sin(\omega t+\phi)\cos(\omega t)\,[\cos(2kx) - 2\cos(kx)] + \sqrt{2D_0}\,\xi(t). \tag{3.29}$$

The flashing ratchet model, as given by Eq. 3.29, is somewhat different from the paradigm. This is a special ratchet model in the sense that the force term (the first term on the RHS of Eq. 3.29 is proportional to the diffusion constant, i.e., proportional to the ambient temperature for a given particle in a particular solvent. This nature of the driving term is due to its entropic origin in the context of nanofluidics, as is mentioned in detail in [47]. *The local inversion symmetry broken non-equilibrium forcing strength being coupled to diffusion strength, it is reasonable to check if such a system could result in meaningful ratcheting transport because one cannot control the driving here independently of the stochastic noise strength.*

In the following, we present the results of numerical investigations of this model to identify the regime of most efficient ratcheting at and around room temperature for a nanochannel with a typical pore radius of approximately 100 nm.

3.3 Results and Analysis

In this section, we present the numerical results obtained from the Langevin dynamics simulations of the entropic flashing ratchet model. We analyze the trajectories of the tracer particles to quantify the ratcheting velocity and investigate its dependence on various system parameters such as temperature, surface undulation amplitude, and frequency. Furthermore, we evaluate the efficiency of this transport mechanism to identify the optimal conditions for particle filtration at the nanoscale.

3.3.1 Ratcheting Trajectories and Velocity

In Fig. 3.4, we show the ratcheting trajectories as obtained from the direct simulation of Eq. 3.29. Here we have plotted x vs t for $D_0 = 10$, 12, 24 and 44 μm^2 s^{-1}, $h_0/H = 0.2$ (i.e. considering $h_0 = 20$ nm and $H = 100$ nm), $\omega = 2000$ rad s^{-1} and $\phi = \pi/2$ rad. The time step for the simulation is $\Delta t = 10^{-5}$ s, and we have employed the Stochastic-Heun method for numerical integration. We have calculated the velocity of Brownian particles by taking an ensemble average of over 2000 realizations. The typical ratcheting velocity we obtain is 0.4-0.8 μm/s per second.

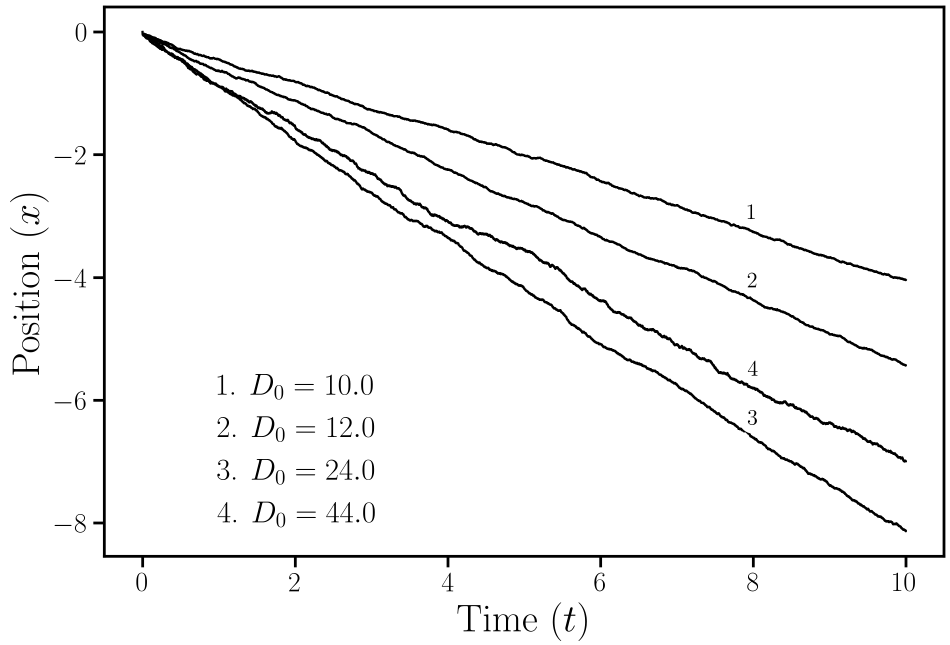

Figure 3.4: Position of the particle showing directed motion. Here, x is the distance in the unit of μm and t is in seconds. Parameters used are: $h_0/H = 0.2$, $\omega = 2000$ rad/s, and $\phi = \pi/2$ rad.

To interpret our results in terms of the room temperature (~ 300 K), we will make use of the Stokes-Einstein relation in what follows. Since ratcheting is a weakly non-equilibrium phenomenon, essentially in the slow dynamics regime, utilizing the Stokes-Einstein relation is appropriate in this context. The Stokes-Einstein relationship is

$$D_0 = \frac{k_B T}{6\pi\eta r}, \tag{3.30}$$

which gives the diffusion constant of the Brownian particle in terms of the temperature T, the radius of the particle r, and the viscosity of the medium η. In the Stokes-Einstein relation, k_B is the Boltzmann constant. One can estimate the temperature of the medium over which this ratcheting happens, corresponding to a reasonably fixed r and η for a given D_0. Similarly, by the same argument, one can see that for a given particle size, a continuous range of temperatures T exists for which ratcheting will occur at different λ values, and, of course, room temperature is just a particular case. For example, substituting the typical viscosity, $\eta = 10^{-3}$ Pa s and a typical radius of the Brownian particle to be 10 nm for $D_0 = 22\ \mu\text{m}^2/\text{s}$ by choosing $\lambda \approx 400.0$ nm, we get $T \approx 300$ K.

3.3.2 Parametric Dependence of Transport

In Fig. 3.5(a) we have kept $\lambda \approx 400$ nm, $\eta = 10^{-3}$ Pa s and $r = 10$ nm. We can see that the magnitude of ratcheting velocity first increases with the increase in T, attains a maximum, and then finally decreases. The maximum of v occurs around $T \approx 380$ K which is close to room temperature (≈ 300 K), which is quite a remarkable observation from the point of view of biological systems. We have studied the effect of global phase ϕ on the ratcheting velocity v, which shows a periodic change in the ratcheting velocity as shown in Fig. 3.5(b) changing from negative to positive, i.e., direction reversal of the average motion due to ratcheting of the Brownian particle can be achieved by adjusting the phase of standing waves on the surface. The reversal of ratcheting velocity $\langle v \rangle$ by the change of phase can be understood from Eq. 3.29 by using the fact that the expression of forcing in that equation changes sign as the phase angle ϕ changes from 0 to 2π.

The size of surface undulations compared to the nanotube diameter plays a crucial role in ratcheting. In Fig. 3.5(c) we have kept $T = 300$ K, $\lambda \approx 400$ nm, $\eta = 10^{-3}$ Pa s and $r = 10$ nm. One can see from Fig. 3.5(c) that the magnitude of the ratcheting velocity increases with increasing h_0/H; however, the limitation to the h_0/H scale arises in the present model from the lubrication approximation. It is due to the underlying lubrication approximation that we have maintained h_0/H between 0.2 and 0.3, and have not increased it to higher values; however, this is a very reasonable range for the amplitude of undulation of the surface confining the nanofluid, considering the phenomenon of ratcheting. Finally in Fig. 3.5(d) we have kept $T = 300$ K, $\lambda \approx 400$ nm, $\eta = 10^{-3}$ Pa s and $r = 10$ nm. We have studied the effect of frequency on the ratcheting velocity. When the applied frequency is

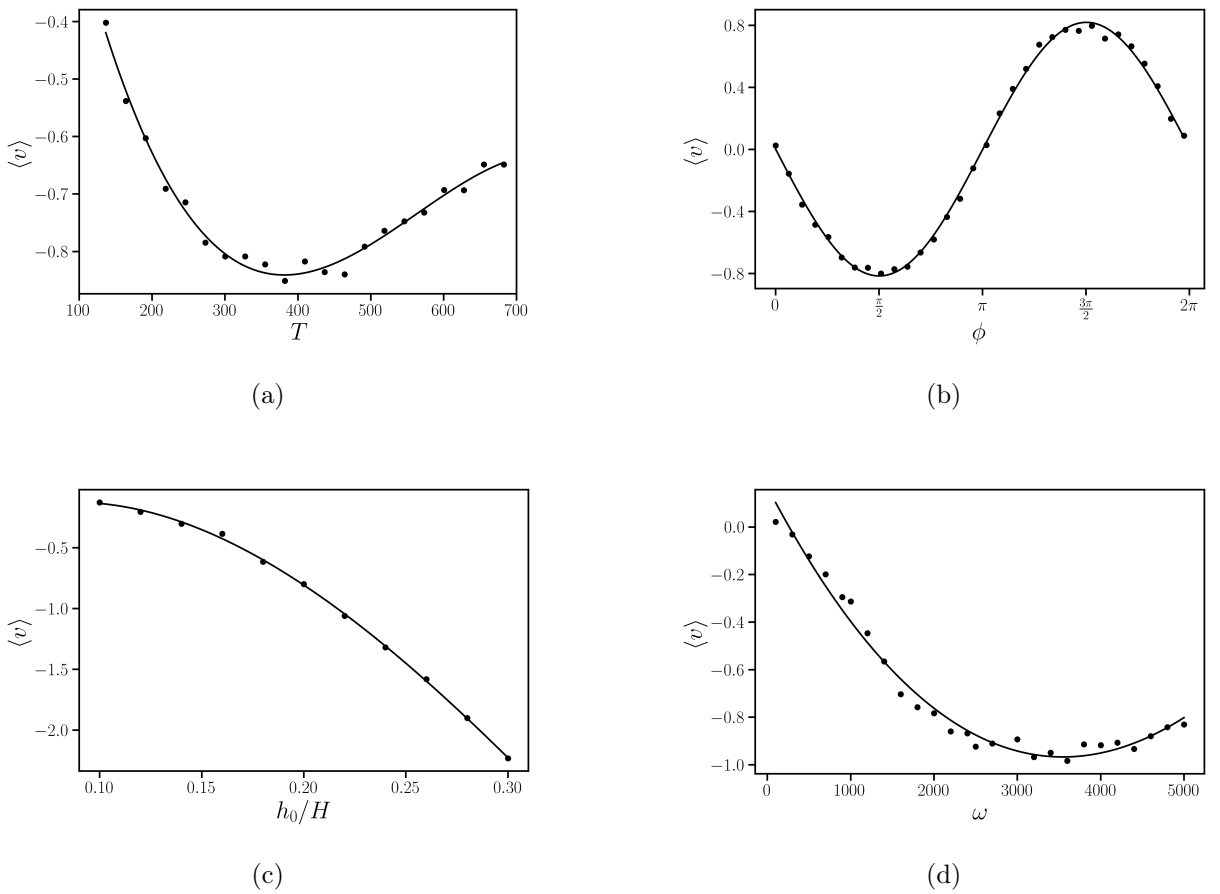

Figure 3.5: (a) Variation of the average velocity $\langle v \rangle$ with temperature T ($\langle v \rangle$ in μm s^{-1}, T in K) for $h_0/H = 0.2$, $\omega = 2000$ rad/s, and $\phi = \pi/2$.

(b) Variation of $\langle v \rangle$ with phase ϕ ($\langle v \rangle$ in μm s^{-1}, ϕ in radians) for $h_0/H = 0.2$, $\omega = 2000$ rad/s, and $T = 300$ K.

(c) Variation of $\langle v \rangle$ with the wall undulation ratio h_0/H ($\langle v \rangle$ in μm s^{-1}) for $T = 300$ K, $\omega = 2000$ rad/s, and $\phi = \pi/2$.

(d) Variation of $\langle v \rangle$ with the oscillation frequency ω ($\langle v \rangle$ in μm s^{-1}, ω in rad/s) for $h_0/H = 0.2$, $T = 300$ K, and $\phi = \pi/2$.

small (corresponding to a time period that is high), the tracer particle gets sufficient time to equilibrate and is transported. Similarly, if the applied frequency is high, the tracer particle will not be able to respond to the surface undulations, and its motion will simply average out, resulting in very small transport. Thus, the applied frequency will attain a maximum for ratcheting velocity, as shown in Fig. 3.5(d).

Although the results in this work are presented in dimensionful form to retain direct physical interpretability and facilitate comparison with experimentally relevant parameter regimes, the underlying behavior can be understood in terms of a few key dimensionless groups. In particular, the transport is governed by the ratio of the driving timescale to the diffusive timescale, characterized by the dimensionless frequency $\Omega = \omega\tau_D$, where $\tau_D \sim L^2/D$ is the diffusion time over a characteristic length scale L. Similarly, thermal effects enter through the ratio of the potential energy scale to thermal energy, $\Delta U/k_BT$. The observed non-monotonic dependence of transport on frequency can be interpreted as a consequence of this timescale competition: for $\Omega \ll 1$, the system approaches quasi-equilibrium and transport vanishes, while for $\Omega \gg 1$, the system cannot respond to rapid modulation. Optimal transport occurs for $\Omega \sim \mathcal{O}(1)$, corresponding to a matching between driving and diffusion timescales.

3.3.3 Efficiency of the Entropic Ratchet

Defining the efficiency ($\mathcal{E}$) of ratcheting particles that actually do not work against a conservative force has been discussed by Derényi et al in [76]. In the spirit of what is defined as an effective efficiency of transport in the generalized case by Derényi et al in [76], efficiency in the present case could be considered in a more revealing form to be $\mathcal{E} = \frac{\gamma\langle v\rangle^2}{\gamma\langle v_0^2\rangle}$ where $\langle v\rangle$ is the average velocity (directional) of the particle and $\langle v_0^2\rangle$ is the mean square velocity imparted on the particle by the surface fluctuations. The γ, being the damping constant, is multiplied in the numerator and denominator to make the expression of the efficiency manifestly a ratio of output to input power. However, the damping constant does not explicitly appear in the expression for efficiency, and it becomes the ratio of the average velocity squared to the average of the undulation velocity (v_0) squared.

In the present case, such efficiency of ratcheting should actually be used. This efficiency can also be viewed as a ratio of kinetic energies, where the mass of the particle cancels out, as it is present in both the numerator and denominator. In overdamped dynamics, the mass of the particle is not defined, and in the ratio of kinetic energies, the mass term safely cancels out. Moreover, a cross-check of the parameter regime over which the lubrication approximation remains intact could be defined to be the regime within which this efficiency remains below unity, i.e., the Carnot limit.

Thus, we define the efficiency $\mathcal{E}$ of ratcheting by the ratio of the square of the mean velocity of the Brownian particle to the mean square velocity of undulating surface fluctuation. Note that the energy is spent mostly by an external agent to create the surface undulations, and that is why we define efficiency in this way. The thermal energy essentially assists in the process of ratcheting by providing the required jitters without contributing much energetically, as is done by the non-equilibrium forcing

$$\mathcal{E} = \frac{\langle v \rangle^2}{\omega^2 h_0^2/2}. \tag{3.31}$$

The value of h_0 in the denominator is determined by considering $H = 100$ nm in the following analysis. In the simulation, we practically use the ratio h_0/H throughout. The denominator in the expression of efficiency 3.31 is the mean square velocity of the oscillatory motion imposed on the particle at a position in space by the undulating surface. We study the variation of efficiency $\mathcal{E}$, with temperature T, dynamic viscosity η, wavelength λ of surface undulations, and the size of the Brownian particle r to find out the most efficient surface-driven channel of the ratcheting transport at room temperature.

We have fixed the amplitude of driving to $h_0/H = 0.2$ and 0.25 for the results in Fig. 3.6, which depict the main results of our simulations aimed at identifying the nature of the fluid and the particle size that transports most efficiently at room temperature in such a nanochannel.

In Fig. 3.6(b), we have plotted the variation of efficiency ($\mathcal{E}$) with temperature (T). By Stokes-Einstein relation ($D_0 = k_B T/6\pi\eta r$), we see that if we fix λ, η and r then $D_0 \propto T$. We have fixed $\lambda = 400$ nm, $\eta = 10^{-3}$ Pa s and $r = 10$ nm. We find that the efficiency of ratcheting increases with increasing temperature (or the diffusion constant) and attains a maximum at $T \approx 380$ K and at $T \approx 400$ K, respectively, for parameters $h_0/H = 0.2$ and 0.25, after which it begins to decline, as shown in Fig. 3.6(b). The value of the room temperature, which is $T \approx 300$ K, depends on the choice of the wavelength λ, which has been fixed here to 400 nm. Consistent with Fig. 3.6(b), Fig. 3.6(c) shows a peak efficiency at a viscosity near the viscosity of water (actually a little lesser than the viscosity of water), and Fig. 3.6(d) identifies the radius of the particle at which the efficiency is maximum, and that radius is between 5 and 10 nm. It is important to note that the observed peak in efficiency near the viscosity of water arises from the specific parameter choices in the present model. In general, the optimal viscosity is not a universal property, but depends on the interplay

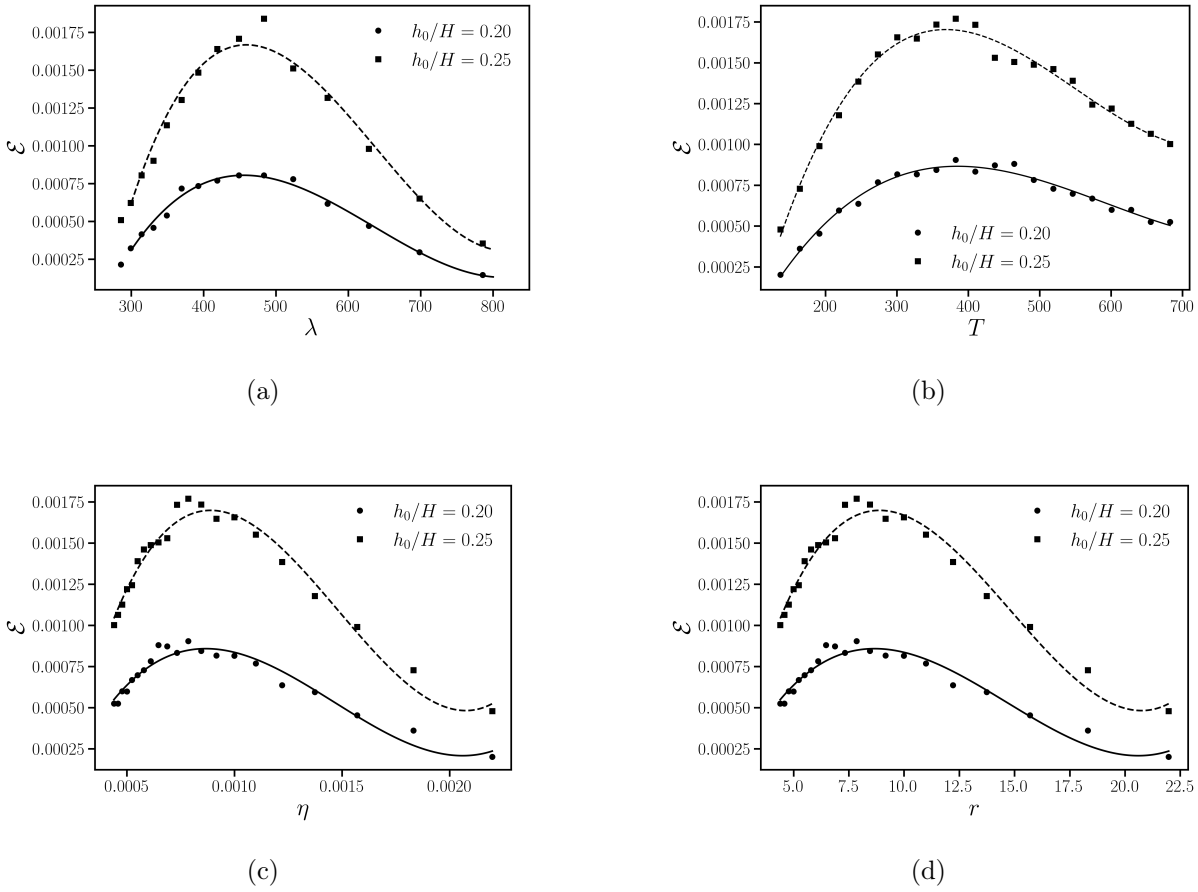

Figure 3.6: (a) Variation of efficiency $\mathcal{E}$ with wavelength λ (λ in nm, $\eta = 10^{-3}$ Pa·s, $r = 10$ nm, $T = 300$ K).

(b) Variation of $\mathcal{E}$ with temperature T (T in K, $\omega = 2000$ rad/s, $\phi = \pi/2$ rad, $\lambda = 400$ nm, $\eta = 10^{-3}$ Pa·s, $r = 10$ nm).

(c) Variation of $\mathcal{E}$ with viscosity η (η in Pa s, $\lambda = 400$ nm, $r = 10$ nm, $T = 300$ K).

(d) Variation of $\mathcal{E}$ with particle radius r (r in nm, $\lambda = 400$ nm, $\eta = 10^{-3}$ Pa s, $T = 300$ K).

between modulation frequency, channel geometry, and particle properties.

In the above figures, we note that the efficiency of this entropic ratchet is very low, i.e., the transport by this entropic ratchet is energetically very costly (the energy conversion from the nonequilibrium drive to directed motion is very low). However, the velocity generated by this mechanism is sufficient for use in the filtering process. Such examples are widespread in biological systems, where the mechanism is usually costly, but it can be used to generate substantial transport velocity. For example, intracellular transport by motor proteins like

kinesin and dynein is energetically very costly, but the velocity of a typical kinesin molecule is reasonably high.

Particular points to note from these efficiency graphs are (1) The value of the viscosity at which the efficiency peaks is quite close to that of water at room temperature, (2) The radius of the particle where the efficiency peaks being about 10 nm is quite consistent with the tube width of about 100 nm and undulation amplitude of a few tens of nanometer, (3) The efficiency falls quite rapidly for particle size less than about 5 nm and more than about 15 nm at room temperature. These plots reveal that, at room temperature, a window of ratcheting transport exists in water for particles about 10 nm in size, driven by surface modes with wavelengths of a few hundred nanometers and oscillation amplitudes of a few tens of nanometers.

As a sanity check, one can also estimate the efficiency of the flashing ratchet using a hand-waving argument. The efficiency of a flashing ratchet, defined as the ratio of useful output power ($f_{\text{load}} \cdot \langle v \rangle$) to input power ($\omega \Delta V$), reduces naturally to the dimensionless ratio $\eta \approx \langle v \rangle / \omega \ell$, the fraction of one spatial period traversed per flash cycle. For the present system, with $\langle v \rangle \approx 0.8\,\mu\text{m/s}$, $\omega \approx 2000\,\text{Hz}$, and $\ell \approx 400\,\text{nm}$, this gives $\eta \approx 0.8 \times 10^{-6}/(2000 \times 400 \times 10^{-9}) \sim 10^{-3}$, meaning only $\sim 0.8\,\text{nm}$ of directed displacement is achieved per flash cycle out of a possible 400 nm, with the remainder dissipated as heat.

This surface-driven ratcheting phenomenon therefore indicates the natural possibility of nanofiltration of particles with a radius of 10 nm or less through a nanochannel with a pore size much larger than the particle radius. This is the most significant revelation of the present analysis, which demonstrates the existence of a remarkable matching of scales in the nanometer regime for particle transport at room temperature.

3.4 Summary

We have demonstrated in this chapter that, based on a broader framework established by Marbach et al. [47], surface fluctuations can drive the ratcheting of Brownian particles in a nanofluidic channel in the presence of a water medium. The present observations are valid within the lubrication approximation. This ratcheting of particles can result in the velocity of particles against the advective motion of the particles in the fluid. This, in principle,

can result in the effective filtration of particles through a nanochannel, where the particles are significantly smaller than the pore size of the channel. The model we present here for the room temperature scenario, in particular, can be easily generalized to other fluids and corresponding temperatures as well using the same method.

Quantitatively, the main result of this work is that ratcheting velocity turns out to be $\sim$ 800 nanometers per second, which is a good number at room temperature. It turns out that water is the most suitable fluid for ratcheting in nanochannels at room temperature for particles with a diameter of approximately 10 nm. Furthermore, this model explains the ratcheting of a wide range of particle sizes, as shown in Fig. 3.6. This is a remarkable effect that boundary undulations can produce, resulting in ratcheting for a very large spectrum of particle sizes typical of nanofluidic systems.

The present analysis is conducted on a single particle to demonstrate the mechanism's operation. In the presence of many particles, these results would be limited to inter-particle interactions no stronger than the strength of the ratcheting term proportional to $kD_0\frac{h_0}{H}$. Since the strength of the ratcheting term is proportional to the diffusivity D_0, the mechanism should work in a sparse distribution of particles where this parameter does not get altered too much due to induced hydrodynamic effects in the many-particle system. The present mechanism could also, in principle, apply to active matter systems where ratcheting has been seen to contribute a wide variety of motions [77, 78]. Self-modulation of particle activity coupled to surface fluctuations in nanochannels could enrich the process. However, careful identification of the entropic effect arising from the hydrodynamics of such active particles would be necessary.

This mechanism of ratcheting, which is possible in nanofluids under surface fluctuations, is a generic one. Most probably, such a mechanism could be in use in some biological systems where particle transport happens without any directional drive. The effects of other finer details on such transport can be addressed once the existence of the basic mechanism is established through experiments. We hope that the application of this mechanism in designing efficient filters is quite feasible, given the current ability to nanoscale engineer such channels.

The existence of such a robust mechanism in nanofluidics at room temperature suggests it may already be in operation in biological systems. Furthermore, its ability to cause particles to move against a bulk fluid flow, equivalent to a particle moving up a potential barrier,

makes it a prime candidate for developing a general mechanism of controlled filtration.

While the present analysis provides a comprehensive understanding of particle transport driven by entropic effects in fluctuating nanochannels, it is based on an effective description that does not explicitly account for the underlying fluid flow field. In realistic micro- and nanofluidic systems, however, particle dynamics is strongly influenced by the hydrodynamic environment, particularly in the presence of deformable or undulating boundaries. To address this, it is essential to analyze the fluid flow generated by such boundary modulations. This naturally leads to the formulation of the problem within the framework of low-Reynolds-number hydrodynamics. In the next chapter, we therefore investigate the interplay between pressure-driven bulk flow and surface-driven boundary flow in undulating nanochannels by directly solving the Navier–Stokes equations under appropriate approximations.

4

Interplay of Bulk and Boundary Flow in Nanochannels

In this chapter, we present a detailed analysis of the characterization of the flow regime of low Reynolds number through soft nanochannels, which creates opportunities for competing flow structures in different directions through a nanotube. In general, such flow structures can exist because the fluid is driven simultaneously by both bulk pressure gradients and surface undulations. Under such competing drives, a substantial fluid fraction might flow in opposite directions, which probably would not exist in wide geometries. This intriguing phenomenon could have potential applications in the separation, trapping, and filtration of particles.

These methods generally aim at particle manipulation, where in many cases, a detailed understanding of the underlying flow structures of the solvent in relation to the forcing is of crucial importance. The analytical approach to handling such flow scenarios that we develop in this chapter can be applied to any microfluidic or nanofluidic system that operates in a low Reynolds number regime, particularly when competing flows under bulk pressure gradients and surface undulations are to be understood. We provide a systematic method here for understanding and characterizing the competing flows in relation to the properties of the fluid and the driving forces.

In the low Reynolds number regime, we delve into understanding surface-fluctuations-driven fluid flow [47] through soft cylindrical nanochannels. The analysis decouples and distinguishes boundary layer flow structures from the bulk flow that exists due to a pressure

head. The effects of the non-linearity of the Navier-Stokes equation remain analytically manageable by the advantage of existing low Reynolds number [39, 41]. The perturbation approach developed in this chapter is a useful general method that can augment existing analyses of such flows through nanotubes with soft elastic walls. The surface-driven flow is explicitly characterized in terms of parameters such as the fluid's density and viscosity. Moreover, the competing and complementary influences of surface drive parameters, such as frequency, amplitude, and wavelength of forcing, are evident in the results.

In the perturbation analysis, we identify the zeroth-order flow as Poiseuille, i.e., driven by the pressure gradient. However, the advantage of the low Reynolds number shows up in the absence of coupling of this Poiseuille flow to the first-order flow fields present due to surface undulations. This decoupling of the zeroth-order and the first-order flows presents a wide avenue for the analytical study of surface-driven flows, which otherwise could appear too complex. In the first order, considering a traveling Fourier mode of surface undulation, corrections to the zeroth-order flow are found. This marks the possible tracking of the crossover in the radial directions between the Poiseuille flow and the flow induced by surface undulations. The characterization of this crossover in terms of the nature of surface drive and fluid is presented.

In the scope of this perturbation study, the effects of the nonlinearity of the Navier-Stokes equation are also captured. The effect of nonlinearity shows up in a nice way in the second order of the perturbation theory. The existence of flow in the first order in perturbations acting as a source in the second order induces finite secondary excitation to the soft boundary due to the nonlinearity of the Navier-Stokes dynamics. Our perturbation analysis, which is essentially linear, explores the effects of a single source mode of surface undulations. However, this is enough in the linear regime to represent the effects of all Fourier modes of surface undulations that could be present in complex surface undulations.

The contents of this chapter are based on the work [79]. First, we present the governing Navier-Stokes equation [80, 81] of fluid flow and the associated boundary conditions relevant to our model system. In this context, we consider the cylindrical geometry of the soft channel. Subsequently, we solve the Navier-Stokes equation under the low-Reynolds-number approximation. We identify the region in the channel where first-order corrections become comparable to the zeroth-order flow and describe the transition from pressure-driven to boundary-fluctuation-driven flow. Following that, we present the results of the second-order

perturbation, which captures the feedback effect of the first-order flow on the soft surface. In this way, we present the complete effect of a single mode of surface drive on the flow of liquid in the nanochannel. At the end of the chapter, we present discussions of our results.

4.1 Model Formulation

Our interest in this chapter is to gain a detailed understanding of the structure of fluid flow through a cylindrical geometry under the joint existence of a pressure gradient along the axis of the tube and surface fluctuations. For such flows through nanotubes, even when surface fluctuations occur at a frequency of several hundred Hertz, the flow remains in a low Reynolds number regime. Based on this, a perturbation analysis of the flow is developed. The dominant linearity of the theory, by virtue of the low Reynolds number, allows us to work with a single mode of surface fluctuations. This is a major advantage of having a theoretical method at hand, which can break down the complexity of the phenomenon in a systematic manner.

4.1.1 System Geometry and Coordinates

As shown schematically in Fig. 4.1, the model system we consider is fluid flow in a cylindrical nanotube of average radius R_0, whose walls, in general, can support undulations generated by oscillating one of the tube's edges. The diameter of the tube could be about hundreds of nanometers. We examine the effects of a sinusoidal forcing at frequency ω at the left edge of the tube, generating a traveling wave of wavenumber k (say) on the tube surface.

4.1.2 Governing Equations (Navier-Stokes & Continuity)

Navier-Stokes equation for the velocity profile $\boldsymbol{u}(\boldsymbol{r}, t)$ of a fluid flow is

$$\rho\left(\frac{\partial \boldsymbol{u}}{\partial t} + (\boldsymbol{u}.\nabla)\boldsymbol{u}\right) = -\nabla P + \eta\nabla^2\boldsymbol{u} + \left(\frac{1}{3}\eta + \zeta\right)\nabla(\nabla.\boldsymbol{u}) + \boldsymbol{f}_{\text{ext}}, \tag{4.1}$$

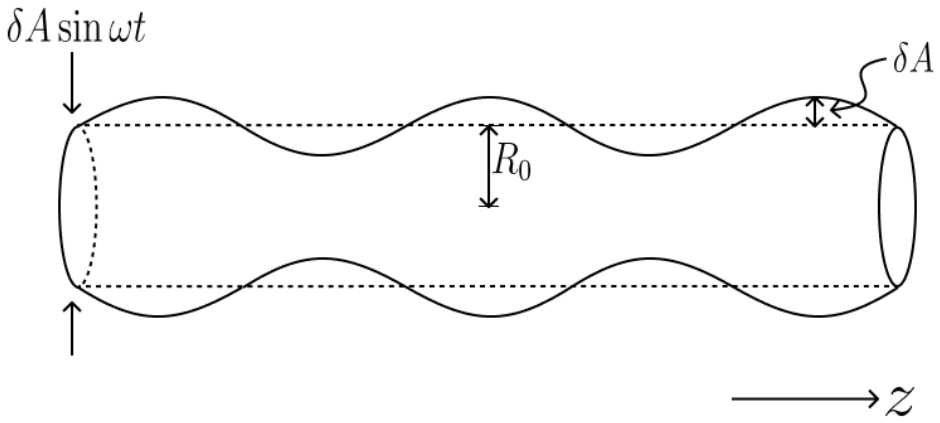

Figure 4.1: Schematic diagram of a nanochannel with undulating walls. Undulations are considered circular symmetric, generated by sinusoidally oscillating the left edge of the tube. Additionally, a pressure gradient is assumed to exist along the axis of the tube.

supplemented with the continuity equation:

$$\frac{\partial \rho}{\partial t} + \nabla.(\rho \boldsymbol{u}) = 0, \tag{4.2}$$

Where ρ and η are, respectively, the fluid's mass density and dynamic viscosity, and ζ is the fluid's second viscosity coefficient or bulk viscosity. In Eq. 4.1, $\boldsymbol{f}_{\text{ext}}$ is the body force acting on the fluid.

Throughout this chapter, we assume the incompressibility of fluid (i.e., $\frac{d\rho}{dt} = 0$), which gives $\nabla.\boldsymbol{u} = 0$ due to the continuity equation. Due to this assumption, the third term in the Navier-Stokes equation drops out for its dependence on the $\nabla \cdot \boldsymbol{u}$. Thus, the above equations reduce to the following form:

$$\rho \left(\frac{\partial \boldsymbol{u}}{\partial t} + (\boldsymbol{u}.\nabla)\boldsymbol{u} \right) = -\nabla P + \eta \nabla^2 \boldsymbol{u} + \boldsymbol{f}_{\text{ext}} \tag{4.3}$$

and

$$\nabla.\boldsymbol{u} = 0. \tag{4.4}$$

4.1.3 Boundary Conditions

To determine the solution uniquely, one needs to impose appropriate boundary conditions on the velocity profile. Boundary conditions describe the fluid behavior at boundaries that the solution must obey at all times. The velocity profile $\boldsymbol{u}(\boldsymbol{r}, t)$ of the fluid satisfies the following boundary condition (known as the Kinematic boundary condition):

$$v(r = R(z,t), z, t) - u(r = R(z,t), z, t)\frac{\partial R(z,t)}{\partial z} - \frac{\partial R(z,t)}{\partial t} = 0. \tag{4.5}$$

Since the boundary of the soft elastic tube undulates, the Kinematic boundary condition must be adopted, which sets the relative velocity of the fluid with the boundary to zero, making the boundary layers follow boundary modes.

4.2 Perturbation Analysis and Solution

In this section, we develop a systematic analytical framework to solve the governing equations of fluid motion. By employing a perturbation expansion in terms of the Reynolds number, we can decompose the complex, non-linear Navier-Stokes equations into a series of more manageable, linear problems. This approach allows us to investigate how bulk-driven flow and surface-driven undulations coexist and compete within the confined geometry of the nanochannel.

4.2.1 The Perturbation Scheme

We intend to solve for the velocity profile $\boldsymbol{u}$ by perturbation theory to make a comparison of different terms of the Navier-Stokes equation. We non-dimensionalise the equation by introducing $r' = r/R_0$, $t' = t/\tau$ ($\tau = 2\pi/\omega$), $\boldsymbol{u'} = \boldsymbol{u}/U$ ($U = R_0/\tau = \omega R_0/2\pi$), $P' = P/P_0$ ($P_0 = \eta U/R_0$) as dimensionless variables. With dimensionless quantities, the Eq. 4.3

becomes:

$$Re\left(\frac{\partial \boldsymbol{u'}}{\partial t'} + (\boldsymbol{u'}.\nabla')\boldsymbol{u'}\right) = -\nabla' P' + \nabla'^2 \boldsymbol{u'} + \boldsymbol{f}'_{\text{ext}}, \tag{4.6}$$

where $\text{Re} = \rho U R_0/\eta = \rho\omega R_0^2/2\pi\eta$ is Reynolds number and $\boldsymbol{f}'_{\text{ext}} = \frac{2\pi R_0}{\eta\omega}\boldsymbol{f}_{\text{ext}}$. Typical numerical values considered being $\rho \sim 10^3$ kg/m^3, $\omega \sim 100$ rad/s, $R_0 \sim 100$ nm, and $\eta \sim 10^{-3}$ Pa s, the Reynolds number is approximately $\text{Re} \sim 10^{-6}$, which is an extremely small number.

Since we are working in a low Reynolds number regime, Re serves as a perturbation parameter. Thus, replacing Re by ϵ Eq. 4.6 takes the shape:

$$\epsilon\left(\frac{\partial \boldsymbol{u'}}{\partial t'} + (\boldsymbol{u'}.\nabla')\boldsymbol{u'}\right) = -\nabla' P' + \nabla'^2 \boldsymbol{u'} + \boldsymbol{f}'_{\text{ext}}. \tag{4.7}$$

Moreover, the geometry of our system, being cylindrical with an undulating surface, makes it convenient to use cylindrical coordinates. In cylindrical coordinates $\boldsymbol{u} = v\hat{\boldsymbol{r}} + u\hat{\boldsymbol{z}}$ (assuming axis-symmetry).

By substituting expressions for Laplacian and convective derivatives in cylindrical coordinates and separating the vector Eq. 4.7 into its component equations, we get two equations. The equation for $\hat{\boldsymbol{z}}$-component is

$$\epsilon\left(\frac{\partial u'}{\partial t'} + u'\frac{\partial u'}{\partial z'} + v'\frac{\partial u'}{\partial r'}\right) = -\frac{\partial P'}{\partial z'} + \frac{\partial^2 u'}{\partial z'^2} + \frac{\partial^2 u'}{\partial r'^2} + \frac{1}{r'}\frac{\partial u'}{\partial r'} + f'_z \tag{4.8}$$

and that in $\hat{\boldsymbol{r}}$ direction is

$$\epsilon\left(\frac{\partial v'}{\partial t'} + v'\frac{\partial v'}{\partial r'} + u'\frac{\partial v'}{\partial z'}\right) = \frac{\partial^2 v'}{\partial z'^2} + \frac{\partial^2 v'}{\partial r'^2} + \frac{1}{r'}\frac{\partial v'}{\partial r'} - \frac{v'}{r'^2} + f'_r. \tag{4.9}$$

Here, we have used $\boldsymbol{f}'_{\text{ext}} = f'_r\hat{\boldsymbol{r}} + f'_z\hat{\boldsymbol{z}}$. This body force must be considered self-consistently because such a force in the bulk of the fluid would eventually be generated when the surface undulations are present. Expanding u' and v' in perturbation series:

$$u' = u'_0 + \epsilon u'_1 + \epsilon^2 u'_2 + \ldots, \tag{4.10}$$

$$v' = v'_0 + \epsilon v'_1 + \epsilon^2 v'_2 + \ldots, \tag{4.11}$$

Similarly, the radius of the nanochannel is expanded as:

$$R(z,t) = R_0 + \epsilon R_1(z,t) + \epsilon^2 R_2(z,t) + \ldots, \tag{4.12}$$

where R_0 is the average radius of the nanochannel. ϵR_1 and $\epsilon^2 R_2$ are, respectively, the first- and second-order undulations present on the surface of the nanochannel. In the context of the following analysis, the ϵR_1 component is considered created by an external agent by driving the surface at the left edge of the tube. As a result of this drive generating flows in the fluid, the non-linearity of the flow generates feedback oscillations $\epsilon^2 R_2$ in the second order. This is the scheme on which we base the perturbation analysis in a self-consistent manner.

4.2.2 Zeroth-Order Solution: The Pressure-Driven Bulk Flow

For the sake of completeness, let's first look at the zeroth-order structure of the solution. We assume that forces f_r and f_z, induced by boundary fluctuations, are order of magnitude smaller than the pressure gradient because these forces are generated by surface undulations of order ϵR_1. The leading order transport of fluid is due to the pressure gradient. Using Eq. 4.8 and 4.9 one can write out the zeroth order equations:

$$-\frac{\partial P'}{\partial z'} + \frac{\partial^2 u_0'}{\partial z'^2} + \frac{\partial^2 u_0'}{\partial r'^2} + \frac{1}{r'}\frac{\partial u_0'}{\partial r'} = 0, \tag{4.13}$$

and

$$\frac{\partial^2 v_0'}{\partial z'^2} + \frac{\partial^2 v_0'}{\partial r'^2} + \frac{1}{r'}\frac{\partial v_0'}{\partial r'} - \frac{v_0'}{r'^2} = 0. \tag{4.14}$$

Now, zeroth-order equations solve for steady flow along the z-direction in a much simpler setting

$$\frac{\partial u_0'}{\partial z'} = 0\ ,\ \frac{\partial^2 u_0'}{\partial z'^2} = 0 \text{ and } v_0' = 0. \tag{4.15}$$

Thus equation for u_0' becomes:

$$-\frac{\partial P'}{\partial z'} + \frac{\partial^2 u_0'}{\partial r'^2} + \frac{1}{r'}\frac{\partial u_0'}{\partial r'} = 0. \tag{4.16}$$

Assuming a constant pressure gradient, solving the equation above yields:

$$u_0' = C_1 + \frac{1}{4}\frac{\partial P'}{\partial z'} r'^2, \tag{4.17}$$

where C_1 is the integration constant. Restoring the dimensions of various quantities, we have:

$$\begin{aligned} u_0 &= U u_0' \\ &= U\left(C_1 + \frac{1}{4\eta}\frac{\partial P}{\partial z}\frac{R_0}{P_0} r^2 \frac{1}{R_0^2}\right) \\ &= C_2 + \frac{1}{4\eta}\frac{\partial P}{\partial z} r^2. \end{aligned} \tag{4.18}$$

Since $v_0' = 0$, we have

$$v_0 = 0, \tag{4.19}$$

where the direction of the longitudinal flow is determined by the pressure head, which could be chosen in either direction in order to make the direction of the bulk flow opposite to the direction of the surface-driven flow profile.

Now, applying the no-slip boundary condition to Eq. (4.18), we have $u_0 = 0$ at $r = R_0$ to give

$$u_0 = -\frac{1}{4\eta}\frac{\partial P}{\partial z}\left(R_0^2 - r^2\right), \tag{4.20}$$

which is the standard Poiseuille flow profile under a constant pressure gradient. Note that the zeroth-order solution is valid for any Reynolds number as long as conditions in Eq. (4.15) are met.

The continuity equation at zeroth order is

$$\frac{1}{r}\frac{\partial}{\partial r}(r v_0) + \frac{\partial u_0}{\partial z} = 0. \tag{4.21}$$

With these expressions for u_0 and v_0, the zeroth-order continuity equation trivially satisfies, as the pressure gradient $\partial P/\partial z$ is a constant. These are all quite well-known results.

4.2.3 First-Order Solution: The Surface-Driven Boundary Flow

First order equations obtained from Eq. (4.8) and (4.9) are:

$$\frac{\partial^2 u_1'}{\partial z'^2} + \frac{\partial^2 u_1'}{\partial r'^2} + \frac{1}{r'}\frac{\partial u_1'}{\partial r'} = -f_z'^{(1)}, \tag{4.22}$$

and

$$\frac{\partial^2 v_1'}{\partial z'^2} + \frac{\partial^2 v_1'}{\partial r'^2} + \frac{1}{r'}\frac{\partial v_1'}{\partial r'} - \frac{v_1'}{r'^2} = -f_r'^{(1)}, \tag{4.23}$$

where $f_z'^{(1)}$ and $f_r'^{(1)}$ respectively represent the z and r components of forces experienced by the fluid due to the surface undulations present on the walls of nanochannels. These forces are associated with a traveling waveform due to the existence of traveling wave modes on the fluid's surface; this connection will be self-consistently justified in what follows.

Note that, in these first-order equations, there appears to be no contribution from the zeroth-order Poissuille's flow due to the following reasons. At the zeroth order, the velocity u_0 (along the z-axis) is a function of r alone, and the radial velocity v_0 is zero. Therefore, the coupled term $v_0\frac{\partial u_0}{\partial r} = 0$ and, at the same time, all the terms involving the z derivative of u_0 are zero. Moreover, there does not exist any other contribution from terms containing $v_0 = 0$ in the first order. Identification of this decoupling of the zeroth-order Poissuille's flow (which is pressure driven) from the first-order velocity field, which is surface-undulations driven, presents remarkable simplicity in the small Reynolds number regime. This particular fact is beyond the scope of this simplified analysis of the surface-driven flow patterns in such systems.

Let us take $f_r' = \epsilon f_r'^{(1)} + \epsilon^2 f_r'^{(2)}$. We take $f_r'^{(1)} = f_1'(r')\cos(2\pi t' - k'z')$. Here $f_1'(r')$ is the r' dependent part of the forcing that has yet to be identified. Thus, Eq. 4.23 becomes:

$$\frac{\partial^2 v_1'}{\partial z'^2} + \frac{\partial^2 v_1'}{\partial r'^2} + \frac{1}{r'}\frac{\partial v_1'}{\partial r'} - \frac{v_1'}{r'^2} = f_1'(r')\cos(2\pi t' - k'z'), \tag{4.24}$$

where $k' = kR_0$. It is clear from above Eq. 4.24 that solution for v_1' will be of the form $v_1' = g(r')\cos(2\pi t' - k'z')$, where $g(r')$ is to be determined. Substituting this ansatz for v_1' in the above Eq. 4.24, we get an equation for $g(r')$.

$$\frac{d^2 g(r')}{dr'^2} + \frac{1}{r'}\frac{dg(r')}{dr'} - \left(k'^2 + \frac{1}{r'^2}\right) g(r') = -\frac{2\pi R_0}{\eta\omega} f_1'(r') \tag{4.25}$$

We take $f_1'(r') = 0$, thus above equation becomes:

$$\frac{d^2g(r')}{dr'^2} + \frac{1}{r'}\frac{dg(r')}{dr'} - \left(k'^2 + \frac{1}{r'^2}\right)g(r') = 0. \tag{4.26}$$

This is a modified Bessel's equation. Therefore, its solution is:

$$g(r') = c_1 I_1(k'r') + c_2 K_1(k'r'). \tag{4.27}$$

Where $I_1(k'r')$ and $K_1(k'r')$ are modified Bessel functions of first and second kinds, respectively. In the above equations, $r'R_0$ represents the radial distance in the nanochannel. We can use the approximation of r' being small to simplify expressions. Using the approximations of I_1 and K_1 for small arguments:

$$I_1(k'r') \sim \frac{k'r'}{2}, \tag{4.28}$$

$$K_1(k'r') \sim \frac{1}{k'r'} \tag{4.29}$$

Eq. 4.27 simplifies to

$$g(r') = c_1\left(\frac{k'r'}{2}\right) + c_2\left(\frac{1}{k'r'}\right). \tag{4.30}$$

Moreover the second term diverges at $r' = 0$, therefore we set $c_2 = 0$ to get:

$$g(r') = c_1\left(\frac{k'r'}{2}\right), \tag{4.31}$$

and

$$v_1' = c_1\left(\frac{k'r'}{2}\right)\cos(2\pi t' - k'z'). \tag{4.32}$$

Using the continuity equation in the first order, we find u_1' using the expression of v_1',

$$u_1' = c_1\Big(\sin(2\pi t' - k'z') - \sin(2\pi t')\Big). \tag{4.33}$$

Since $f_z = \epsilon f_z^{(1)} + \epsilon^2 f_z^{(2)}$, therefore,

$$\frac{\partial^2 u_1'}{\partial z'^2} + \frac{\partial^2 u_1'}{\partial r'^2} + \frac{1}{r'}\frac{\partial u_1'}{\partial r'} = -\frac{2\pi R_0}{\eta\omega} f_z^{(1)}. \tag{4.34}$$

Which gives,

$$f_z^{(1)} = c_1 \frac{\eta\omega k'^2}{2\pi R_0} \sin(2\pi t' - k'z'). \tag{4.35}$$

Now, after restoring the dimensions of various terms, we get,

$$u_1(r,z,t) = c_1 \frac{\omega R_0}{2\pi} \Big(\sin(\omega t - kz) - \sin(\omega t) \Big), \tag{4.36}$$

where the $u_1(r,z,t) = 0$ at $z = 0$. The longitudinal velocity at $z = 0$ vanishes because of the consideration of that edge being driven radially. The radial velocity has the expression

$$v_1(r,z,t) = c_1 \left(\frac{k\omega R_0}{4\pi} \right) r \cos(\omega t - kz), \tag{4.37}$$

and

$$f_z^{(1)} = \frac{\eta\omega k^2 R_0}{2\pi} \sin(\omega t - kz). \tag{4.38}$$

Finally, using the Kinematic boundary condition to find $R_1(z,t)$ we get,

$$R_1(z,t) = \frac{c_1 k R_0^2}{4\pi} \sin(\omega t - kz). \tag{4.39}$$

Calling the amplitude of the surface undulations $\frac{c_1 k R_0^2}{4\pi}$ as A_0, we have:

$$R_1(z,t) = A_0 \sin(\omega t - kz). \tag{4.40}$$

which is, for example, set due to the driving at the edge $z = 0$. This gives

$$c_1 = \frac{4\pi A_0}{k R_0^2}. \tag{4.41}$$

In terms of the drive amplitude A_0, we can now write,

$$u_1(r,z,t) = \frac{2\omega A_0}{k R_0} \Big(\sin(\omega t - kz) - \sin(\omega t) \Big) \tag{4.42}$$

and

$$v_1(r,z,t) = \frac{\omega A_0}{R_0} r \cos(\omega t - kz). \tag{4.43}$$

The amplitude of u_1 is constant while that of v_1 is linearly dependent on r, which is also

consistent with the fact that the v_1 mode must vanish at $r = 0$ due to symmetry.

From what is given above, we can calculate the expression of the ratio of amplitudes of u_1 and v_1 to get

$$\left|\frac{u_1}{v_1}\right| \sim \frac{4\frac{\omega}{k}\frac{A_0}{R_0}}{\frac{\omega A_0}{R_0}r}. \tag{4.44}$$

or,

$$\left|\frac{u_1}{v_1}\right| \sim \frac{1}{kr} \sim \frac{\lambda}{r}. \tag{4.45}$$

By simply increasing or decreasing the wavelength of surface undulations, one can tune the relative strength of transverse to longitudinal components at a given r.

4.2.4 Second-Order Solution: Non-linear Feedback Effects

Before concluding the chapter, we would like to digress a little by presenting the second-order equations and their solutions, as the effects of the time dependence and non-linearity of the Navier-Stokes equation will show up in second-order under this perturbation scheme. The boundary conditions considered here, as usual, take into account the soft boundary. In the second order, the flow will generate feedback to the boundary undulations considered in the previous order. The soft boundary admitting those feedback modes would keep the dynamics closed. Using Eq. 4.8 and 4.9, we obtain the second-order equations. Here, the right-hand side of the following equations is completely known in terms of previously calculated quantities and their derivatives.

$$\frac{\partial^2 u_2'}{\partial z'^2} + \frac{\partial^2 u_2'}{\partial r'^2} + \frac{1}{r'}\frac{\partial u_2'}{\partial r'} + \frac{2\pi R_0}{\eta\omega} f_z^{(2)} = \frac{\partial u_1'}{\partial t'} + u_0'\frac{\partial u_1'}{\partial z'} + v_1'\frac{\partial u_0'}{\partial r'}. \tag{4.46}$$

$$\frac{\partial^2 v_2'}{\partial z'^2} + \frac{\partial^2 v_2'}{\partial r'^2} + \frac{1}{r'}\frac{\partial v_2'}{\partial r'} - \frac{v_2'}{r'^2} + \frac{2\pi R_0}{\eta\omega} f_r^{(2)} = \frac{\partial v_1'}{\partial t'} + u_0'\frac{\partial v_1'}{\partial z'}. \tag{4.47}$$

In the absence of $f_r^{(2)}$, i.e., when $f_r^{(2)} = 0$, Eq. 4.47 becomes:

$$\frac{\partial^2 v_2'}{\partial z'^2} + \frac{\partial^2 v_2'}{\partial r'^2} + \frac{1}{r'}\frac{\partial v_2'}{\partial r'} - \frac{v_2'}{r'^2} = \frac{\partial v_1'}{\partial t'} + u_0'\frac{\partial v_1'}{\partial z'}. \tag{4.48}$$

Where $r' = r/R_0, t' = t/\tau$ and $k' = kR_0$ as before. Substituting the expressions for u_0' and v_1', above equation takes the form:

$$\frac{\partial^2 v_2'}{\partial z'^2}+\frac{\partial^2 v_2'}{\partial r'^2}+\frac{1}{r'}\frac{\partial v_2'}{\partial r'}-\frac{v_2'}{r'^2} = -c_1 k' \sin(2\pi t'-k'z')\times\left(\pi+\frac{1}{8}\frac{\partial P'}{\partial z'}k'\right)r'+\frac{1}{8}\frac{\partial P'}{\partial z'}c_1 k'^2\sin(2\pi t'-k'z')r'^3. \tag{4.49}$$

Which can also be written as

$$\frac{\partial^2 v_2'}{\partial z'^2}+\frac{\partial^2 v_2'}{\partial r'^2}+\frac{1}{r'}\frac{\partial v_2'}{\partial r'}-\frac{v_2'}{r'^2} = (Br'+Cr'^3)\times\sin(2\pi t'-k'z'). \tag{4.50}$$

With $B = -c_1 k'\left(\pi+\frac{1}{8}\frac{\partial P'}{\partial z'}k'\right)$ and $C = \frac{1}{8}\frac{\partial P'}{\partial z'}c_1 k'^2$.

Assuming a solution of the form $v_2' = h(r')\sin(2\pi t'-k'z')$ and substituting in the above equation, we get the following equations for $h(r')$:

$$\frac{d^2h(r')}{dr'^2}+\frac{1}{r'}\frac{dh(r')}{dr'}-\left(k'^2+\frac{1}{r'^2}\right)h(r') = Br'+Cr'^3. \tag{4.51}$$

The above equation can be solved using the method of variation of parameters, and the solution is $h(r') = \frac{B}{8}r'^3+\frac{C}{24}r'^5$. Thus,

$$v_2' = \left(\frac{B}{8}r'^3+\frac{C}{24}r'^5\right)\sin(2\pi t'-k'z'). \tag{4.52}$$

Restoring the dimensions gives:

$$v_2(r,z,t) = \frac{\omega R_0}{2\pi}\left(\frac{B}{8}\left(\frac{r}{R_0}\right)^3+\frac{C}{24}\left(\frac{r}{R_0}\right)^5\right)\times\sin(\omega t-kz). \tag{4.53}$$

To find out u_2, we use the continuity equation in the second order. The continuity equation in the second order is:

$$\frac{1}{r}\frac{\partial}{\partial r}(rv_2)+\frac{\partial u_2}{\partial z} = 0, \tag{4.54}$$

Which gives:

$$u_2(r,z,t) = \frac{\omega R_0}{2\pi}\left(\frac{B}{2kR_0}\left(\frac{r}{R_0}\right)^2+\frac{C}{4kR_0}\left(\frac{r}{R_0}\right)^4\right)\times\left(\cos(\omega t-kz)-\cos(\omega t)\right). \tag{4.55}$$

Here, $B = -c_1 k R_0 \left(\pi + \frac{\pi k R_0^2}{4\eta\omega}\frac{\partial P}{\partial z}\right)$ and $C = c_1 \frac{\pi k^2 R_0^3}{4\eta\omega}\frac{\partial P}{\partial z}$. Substituting the value of c_1 in terms of A_0 we obtain, $B = -\frac{4\pi^2 A_0}{R_0}\left(1 + \frac{k R_0^2}{4\eta\omega}\frac{\partial P}{\partial z}\right)$ and $C = \frac{k\pi A_0 R_0}{4\eta\omega}\frac{\partial P}{\partial z}$.

To find out the $R_2(z,t)$ we use Kinematic boundary condition in second order.

$$v_2 - u_1\frac{\partial R_1}{\partial z} - u_0\frac{\partial R_2}{\partial z} - u_2\frac{\partial R_0}{\partial z} - \frac{\partial R_2}{\partial t}\bigg|_{r=R_0} = 0. \tag{4.56}$$

Since $u_0 = 0$ at $r = R_0$ and R_0 is constant,

$$v_2 - u_1\frac{\partial R_1}{\partial z} - \frac{\partial R_2}{\partial t}\bigg|_{r=R_0} = 0. \tag{4.57}$$

At $r = R_0$, one gets:

$$\frac{\partial R_2}{\partial t} = \frac{\omega R_0}{2\pi}\left(\frac{B}{8} + \frac{C}{24}\right)\sin(\omega t - kz) + \frac{\omega A_0^2}{R_0} \times \sin(2\omega t - 2kz) - \frac{\omega A_0^2}{R_0}(\sin(kz) + \sin(2\omega t - kz)). \tag{4.58}$$

In the above structure, the third term gives the divergence. To avoid this divergence, we introduce a non-zero $f_r^{(2)}$ to exactly cancel out the divergent term. We take $f_r^{(2)} = k'^2\frac{\eta\omega}{R_0}\left(\frac{A_0}{R_0}\right)^2\sin(k'z')$. Thus, Eq. 4.47 becomes:

$$\frac{\partial^2 v_2'}{\partial z'^2} + \frac{\partial^2 v_2'}{\partial r'^2} + \frac{1}{r'}\frac{\partial v_2'}{\partial r'} - \frac{v_2'}{r'^2} = -2\pi k'^2\frac{A_0^2}{R_0^2}\sin(k'z') + \frac{\partial v_1'}{\partial t'} + u_0'\frac{\partial v_1'}{\partial z'}. \tag{4.59}$$

Where $r' = r/R_0, t' = t/\tau$ and $k' = kR_0$ as before. Substituting the expressions for u_0' and v_1', above equation takes the form:

$$\frac{\partial^2 v_2'}{\partial z'^2} + \frac{\partial^2 v_2'}{\partial r'^2} + \frac{1}{r'}\frac{\partial v_2'}{\partial r'} - \frac{v_2'}{r'^2} = -2\pi k'^2\frac{A_0^2}{R_0^2}\sin(k'z') - c_1 k'\sin(2\pi t' - k'z')\left(\pi + \frac{1}{8}\frac{\partial P'}{\partial z'}k'\right)r' + \frac{1}{8}\frac{\partial P'}{\partial z'}c_1 k'^2\sin(2\pi t' - k'z')r'^3. \tag{4.60}$$

Which can also be written as

$$\frac{\partial^2 v_2'}{\partial z'^2} + \frac{\partial^2 v_2'}{\partial r'^2} + \frac{1}{r'}\frac{\partial v_2'}{\partial r'} - \frac{v_2'}{r'^2} = -2\pi k'^2 \frac{A_0^2}{R_0^2}\sin(k'z') + (Br' + Cr'^3)\sin(2\pi t' - k'z'). \quad (4.61)$$

With $B = -c_1 k'\left(\pi + \frac{1}{8}\frac{\partial P'}{\partial z'}k'\right)$ and $C = \frac{1}{8}\frac{\partial P'}{\partial z'}c_1 k'^2$. Assuming a solution of the form $v_2' = h(r')\sin(2\pi t' - k'z') + 2\pi(A_0^2/R_0^2)\sin(k'z')$ and substituting in the above equation, we get the following equations for $h(r')$:

$$\frac{d^2h(r')}{dr'^2} + \frac{1}{r'}\frac{dh(r')}{dr'} - \left(k'^2 + \frac{1}{r'^2}\right)h(r') = Br' + Cr'^3. \quad (4.62)$$

The above equation can be solved using the method of variation of parameters, and the solution is $h(r') = \frac{B}{8}r'^3 + \frac{C}{24}r'^5$. Thus,

$$v_2' = \left(\frac{B}{8}r'^3 + \frac{C}{24}r'^5\right)\sin(2\pi t' - k'z') + 2\pi\frac{A_0^2}{R_0^2}\sin(k'z'). \quad (4.63)$$

Restoring the dimensions gives:

$$v_2(r,z,t) = \frac{\omega R_0}{2\pi}\left(\frac{B}{8}\left(\frac{r}{R_0}\right)^3 + \frac{C}{24}\left(\frac{r}{R_0}\right)^5\right)\sin(\omega t - kz) + \frac{\omega A_0^2}{R_0}\sin(kz). \quad (4.64)$$

To find out u_2, we use the continuity equation in the second order. The continuity equation in the second order is:

$$\frac{1}{r}\frac{\partial}{\partial r}(rv_2) + \frac{\partial u_2}{\partial z} = 0, \quad (4.65)$$

Which gives:

$$u_2(r,z,t) = \frac{\omega R_0}{2\pi}\left(\frac{B}{2kR_0}\left(\frac{r}{R_0}\right)^2 + \frac{C}{4kR_0}\left(\frac{r}{R_0}\right)^4\right)\times\left(\cos(\omega t - kz) - \cos(\omega t)\right). \quad (4.66)$$

Here, $B = -c_1 kR_0\left(\pi + \frac{\pi k R_0^2}{4\eta\omega}\frac{\partial P}{\partial z}\right)$ and $C = c_1\frac{\pi k^2 R_0^3}{4\eta\omega}\frac{\partial P}{\partial z}$. Substituting the value of c_1 in terms of A_0 we obtain, $B = -\frac{4\pi^2 A_0}{R_0}\left(1 + \frac{kR_0^2}{4\eta\omega}\frac{\partial P}{\partial z}\right)$ and $C = \frac{k\pi A_0 R_0}{4\eta\omega}\frac{\partial P}{\partial z}$.

Using the Kinematic boundary condition, we get,

$$R_2(z,t) = -\frac{R_0}{2\pi}\left(\frac{B}{8}+\frac{C}{24}\right)\cos(\omega t - kz) - \frac{A_0^2}{R_0}\sin\left(\frac{kz}{2}\right)\sin\left(2\omega t - \frac{3kz}{2}\right). \tag{4.67}$$

which finally results in

$$\begin{aligned} R(z,t) &= R_0 + Re\, R_1(z,t) + Re^2 R_2(z,t) \\ &= R_0 + Re\, A_0 \sin(\omega t - kz) - Re^2 \frac{R_0}{2\pi}\left(\frac{B}{8}+\frac{C}{24}\right)\cos(\omega t - kz) \\ &\quad - Re^2 \frac{A_0^2}{R_0}\sin\left(\frac{kz}{2}\right)\cos\left(2\omega t - \frac{3kz}{2}\right). \end{aligned} \tag{4.68}$$

or equivalently

$$\begin{aligned} R(z,t) &= R_0 + Re\, R_1(z,t) + Re^2\, R_2(z,t) \\ &= R_0 + Re\, A_0 \sin(\omega t - kz) + Re^2 \frac{R_0}{16}\left[4\pi\frac{A_0}{R_0} + \left(\pi - \frac{1}{12}\right)\frac{kA_0R_0}{\eta\omega}\frac{\partial P}{\partial z}\right]\cos(\omega t - kz) \\ &\quad - Re^2 \frac{A_0^2}{R_0}\sin\left(\frac{kz}{2}\right)\cos\left(2\omega t - \frac{3kz}{2}\right). \end{aligned} \tag{4.69}$$

In this structure of the surface undulations, the order Re term could be imagined to be the driving of the surface by some external agent with driving amplitude A_0. At the order Re^2, the first term is the feedback on the soft surface due to the dynamics, whereas the second term is due to the non-linearity of the N-S equation. Putting in place the expression for Re, one can now get the $R(z,t)$ in terms of all physical parameters as:

$$\begin{aligned} R(z,t) &= R_0 + Re\, R_1(z,t) + Re^2 R_2(z,t) \\ &= R_0 + \frac{\rho\omega R_0^2}{2\pi\eta}A_0 \sin(\omega t - kz) + \frac{\rho^2\omega^2 R_0^5}{64\pi^2\eta^2}\left[4\pi\frac{A_0}{R_0} + \left(\pi - \frac{1}{12}\right)\frac{kA_0R_0}{\eta\omega}\frac{\partial P}{\partial z}\right]\cos(\omega t - kz) \\ &\quad - \frac{\rho^2\omega^2 R_0^3 A_0^2}{4\pi^2\eta^2}\sin\left(\frac{kz}{2}\right)\cos\left(2\omega t - \frac{3kz}{2}\right). \end{aligned} \tag{4.70}$$

4.3 Results: Crossover of Flow Regimes

In this section, we present the key results of our perturbation analysis, focusing on the competition between the Poiseuille bulk flow and the surface-driven corrections. We specifically identify a critical radial position-the crossover radius-where these two flow regimes become comparable in magnitude. This characterization is crucial for understanding how boundary effects can significantly influence the overall transport properties near the channel walls.

4.3.1 Derivation of the Crossover Radius

The zeroth-order Poiseuille flow, direction of which could be altered by flipping the pressure head, falls quadratically near the average radius of the tube R_0. This is the region where the first-order correction to Poiseuille's flow becomes comparable to the pressure-driven flow. One can find out the crossover radius of these flows by comparing them in this boundary region.

To find out the value of r where first order correction u_1 becomes comparable to base flow u_0, we set,

$$|u_0|\Big|_{r=r_0} \approx Re|u_1|\Big|_{r=r_0}. \tag{4.71}$$

Which gives,

$$\frac{1}{4\eta}\left|\frac{\partial P}{\partial z}\right|(R_0^2 - r_0^2) \approx 4Re\frac{\omega}{k}\frac{A_0}{R_0} \tag{4.72}$$

or,

$$\frac{1}{4\eta}\left|\frac{\partial P}{\partial z}\right|\left(1 - \frac{r_0^2}{R_0^2}\right)R_0^2 \approx 4Re\frac{\omega}{k}\frac{A_0}{R_0}. \tag{4.73}$$

Solving the above equation gives:

$$\frac{r_0^2}{R_0^2} \approx 1 - Re\frac{16\omega A_0\eta}{kR_0^3}\left|\frac{\partial P}{\partial z}\right|^{-1}. \tag{4.74}$$

Since $Re = \rho\omega R_0^2/2\pi\eta$, therefore,

$$\frac{r_0^2}{R_0^2} \approx 1 - \frac{4\rho\omega^2 A_0\lambda}{\pi^2 R_0}\left|\frac{\partial P}{\partial z}\right|^{-1}. \tag{4.75}$$

Giving,

$$\frac{r_0}{R_0} \approx \sqrt{1 - \frac{4\rho\omega^2 A_0 \lambda}{\pi^2 R_0} \left|\frac{\partial P}{\partial z}\right|^{-1}}. \tag{4.76}$$

This gives the expression of the cross-over radius r_0 in terms of other parameters.

4.3.2 The Boundary-Driven Flow Parameter (Q_0)

We define Q_0 as the dimensionless ratio R_0/r_0, representing the extent to which the fluid flow is boundary-driven. A higher value of the R_0/r_0 ratio signifies a boundary-dominant flow, while a smaller value of Q_0 indicates a pressure-driven flow.

$$Q_0 = \frac{R_0}{r_0} \approx \left[1 - \frac{4\rho\omega^2 A_0 \lambda}{\pi^2 R_0} \left|\frac{\partial P}{\partial z}\right|^{-1}\right]^{-1/2} \tag{4.77}$$

4.3.3 Influence of Pressure Gradient and Forcing Parameters

From Eq. 4.76 we see that the fluid and forcing parameters i.e., ρ, ω and λ are restricted by the following constraint:

$$\frac{4\rho\omega^2 A_0 \lambda}{\pi^2 R_0} \left|\frac{\partial P}{\partial z}\right|^{-1} < 1. \tag{4.78}$$

In other words $\frac{4\rho\omega^2 A_0 \lambda}{\pi^2 R_0} \left|\frac{\partial P}{\partial z}\right|^{-1} = 1$ defines a surface in ρ, ω and λ space and for Eq. 4.76 to make sense, the parameters ρ, ω and λ have to satisfy Eq. 4.78.

In Fig. 4.2(a), we have presented a plot of λ and ω for three different values of pressure gradient $|\partial P/\partial z|$ as governed by Eq. 4.78. Similarly Fig. 4.2(b) shows the variation of λ vs ω for three different values of δA. We have assumed a fluid density of 1.0×10^3 kg/m^3 and used typical values for the other parameters, i.e., $R_0 = 100$ nm and $\delta A = 10$ nm. This plot essentially specifies the allowed range of driving parameters ω and λ required for Eq. 4.78 to be valid, i.e., the values of forcing parameters λ and ω should lie within the curves shown in Fig. 4.2(a) and 4.2(b). Corresponding to a particular driving frequency ω, the wavelength λ of the surface modes will essentially be selected by the nature of the elasticity of the surface.

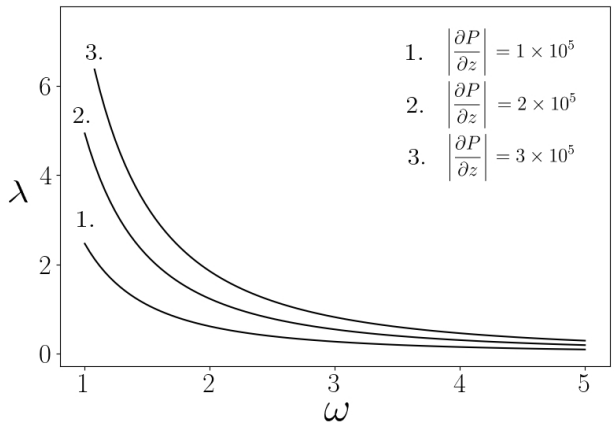

(a)

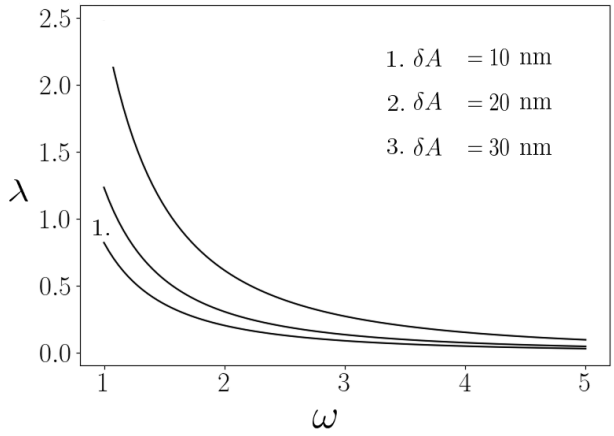

(b)

Figure 4.2: Variation of λ (in 100 nm) with ω (in 10^2 rad s^{-1}). (a) $\delta A(= \mathrm{Re}\, A_0) = 10$ nm; (b) $|\partial P/\partial z| = 10^5$ Pa/m. Other parameters: $R_0 = 100$ nm, $\rho = 1.0 \times 10^3$ kg/m^3.

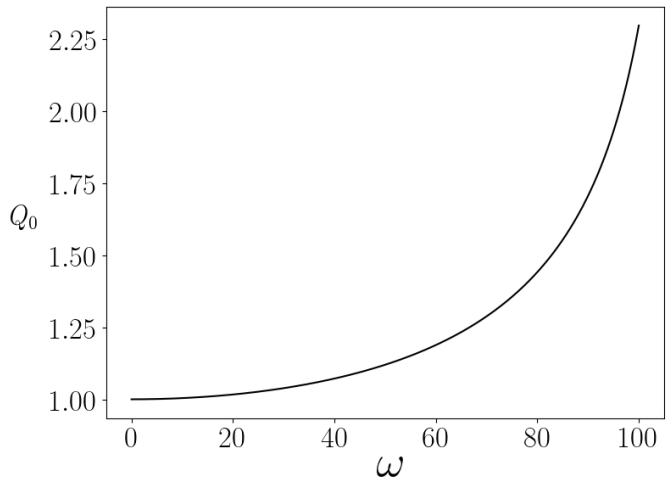

(a)

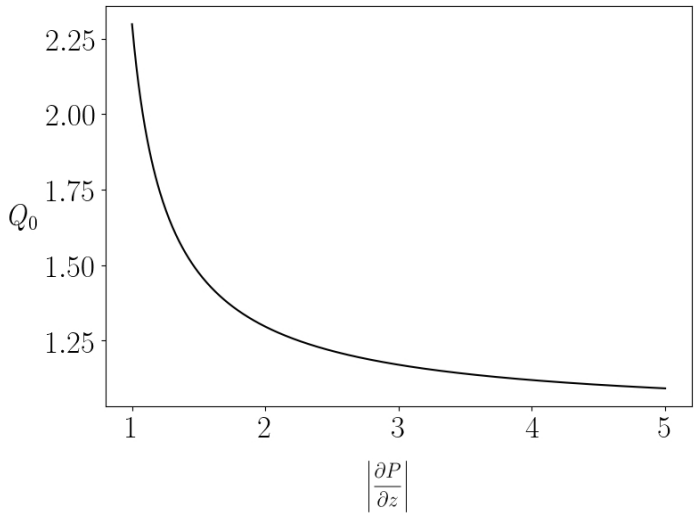

(b)

Figure 4.3: Variation of Q_0 with control parameters: (a) Variation of Q_0 with ω (in rad s^{-1}); (b) Variation of Q_0 with $|\partial P/\partial z|$ (in 10^5 Pa m^{-1}). The parameters used are $R_0 = 100$ nm, $\delta A (= \mathrm{Re}\, A_0) = 10$ nm, $|\partial P/\partial z| = 10^5$ Pa m^{-1} (for panel a), and $\rho = 1.0 \times 10^3$ kg m^{-3}.

Fig. 4.2(a) and 4.2(b) effectively quantify the possible range of elasticity characterizing the boundary surface of the fluid. This is a general result that identifies a typical range of surface types that would be useful for making surface-driven flows compete with the bulk flow in water.

In Fig. 4.3(a) and 4.3(b) we have presented the plots of dimensionless parameter Q_0 against ω and $|\partial P/\partial z|$ respectively taking the fluid density to be 1.0×10^3 kg/m^3. For this, we have taken typical values of other parameters, i.e., $R_0 = 100$ nm, $\lambda = 200$ nm, and $\delta A(= ReA_0) = 10$ nm. This plot essentially specifies the value of driving frequency ω and pressure gradient $|\partial P/\partial z|$ needed for a high value of Q_0, which corresponds to highly boundary-driven flow rather than pressure-driven.

4.4 Summary and Discussion

Within the framework of perturbation theory, we have explored the soft-surface-driven transport of a liquid in an undulating nanotube superposed on a flow driven by pressure. Employing the advantages of a low-Reynolds-number regime, we provide a detailed exploration of boundary-driven transport compared to pressure-driven one. The mechanism shown is significant for nanotubes in general. We have captured the conditions under which the surface-driven flow appreciably surpasses pressure-driven flow near the boundary of the channel and have explicitly quantified the dependence of these competing flows on the material properties of the tube, its driving mechanism, and the nature of the fluid. As shown in Chapter 5, the geometric term Itô in the Langevin equation for the dynamics of a tracer particle (arising due to curvilinear geometry) pushes the particle near the boundary of the channel. Since surface-driven flow is stronger near the channel boundary, the presence of surface undulations is crucial when studying fluid or particle transport in a channel. If one tunes the various parameters properly then these surface undulations can give rise to the transport in a direction opposite to bulk transport given by pressure gradient. Thus, these type of systems with undulating walls naturally finds application in filtration and are worth exploring for the same.

In this work, we have considered straight nanochannels with undulating walls. In a more general case of nonstraight channels, the presented analysis still holds, provided that the average radius of the nanochannel varies slowly with z. Since our work focuses on the low

Reynolds number regime, where the flow remains laminar, the model can be extended to non-straight channels as long as the Poiseuille flow profile is not significantly disturbed. Moreover, as a general case, in this present work, we have considered a semi-infinite channel, which required us to keep the average radius constant. However, a monotonic spatial variation in the average radius would require one to take into account a tube of finite length with appropriate boundary conditions. Such complex situations can be considered specific cases once the general method is established, which is why we have chosen the present model in geometry, which is amenable to simple calculations, to present the general method.

To quantify the surface-driven and pressure-driven flow characteristics in an undulating nanochannel, we have introduced the parameter Q_0, which would prove useful. The quantification by Q_0 is crucial from an engineering perspective. This single parameter takes into account the nature of the fluid present in the nanotube, specifically its density, as well as the frequency and wavelength of the applied forcing. The bound on the allowed regime of driving frequency and wavelength follows automatically from our analysis, which characterizes the possible surface conditions. Interestingly, the viscosity of the fluid does not feature in the parameter Q_0. It is the geometry of the tube and the density of water, apart from the force parameters on which Q_0 is dependent. The frequency of undulation of the surface when it crosses the range of about 50 Hz, Q_0, increases rapidly in a tube of radius 100 nm, where the density of the fluid is that of water at room temperature. Moreover, the non-linear suppression of Q_0 with the increase in the end-to-end pressure gradient, which drives the bulk flow, becomes more prominent in the same tube for the same density of liquid as the pressure gradient becomes more than 10^5 Pa m^{-1}. These numbers can change in other geometries of the flow, which could be a subject of future investigation.

In the present analysis, the method developed is elegant, besides being quite simple, allowing a deeper understanding of the interplay among competing/collaborating factors in flow through the soft nanotube. A complete analysis of pressure and surface undulations-driven flow for a single Fourier mode of the surface drive and its feedback is presented. In the linear regime of dynamics, this is enough to extend the analysis to all other modes. Very specific results are quantified in terms of the dependence of flows on the type of surface, the driving frequency, and the nature of the fluid. The method shown, being very general for the low Reynolds number regime, which is typical for nanochannels, holds promise for wider application.

In this chapter, we have developed a detailed hydrodynamic description of flow in undulating nanochannels, identifying the distinct roles of pressure-driven bulk flow and surface-driven boundary flow. The analysis reveals that surface undulations can generate non-trivial flow structures, particularly near the channel boundaries, which can significantly influence transport in confined systems. However, while the fluid velocity field has been characterized, the implications of these flow structures on the motion of tracer particles remain to be explored. In particular, it is of interest to understand whether such hydrodynamic effects can be harnessed to induce directed particle transport, analogous to ratchet mechanisms. In the next chapter, we address this question by coupling the hydrodynamic flow field with stochastic particle dynamics, leading to the formulation of a hydrodynamic ratchet model that enables controlled transport in micro- and nanochannels.

It is important to note that the characteristic frequency of wall modulation considered in this chapter differs from that used in Chapter 3. In Chapter 3, the transport mechanism is governed primarily by entropic effects and stochastic particle dynamics, where the relevant time scale is set by diffusion. This, in turn, determines the range of external frequencies required to effectively induce particle ratcheting. In contrast, the present chapter focuses on hydrodynamic effects arising from boundary-driven fluid flow. From the definition of the Reynolds number ($\mathrm{Re} = \rho\omega \mathrm{R}_0^2/2\pi\eta$) and the expression for the cross-over radius, it is clear that the chosen frequency must satisfy two conditions: the Reynolds number remains sufficiently small, and the cross-over radius does not become comparable to the radius of the nanochannel, so that surface-driven effects dominate. These considerations together determine the appropriate frequency scale in this model.

5

Hydrodynamic Ratchet Model

THIS chapter develops a detailed and consistent analytical method for the ratcheting of tracer particles [57, 82, 83, 84, 85] dragged by a local inversion symmetry broken axial velocity field in a microchannel. In this chapter, we explore the scope for a consistent analytical treatment of the problem, which is important in many respects. Such an analytical approach reveals a host of information on the details of the interdependence between ratcheting and the geometry, fluid type, and forcing parameters.

We demonstrate in detail that a local inversion symmetry-broken velocity field in a fluid can be perturbatively explored in the low-Reynolds-number regime. The analysis revealed the relationship between the velocity field and corresponding surface undulations, which is essential to know in order to implement subsequent numerical analysis for the motion of tracer particles in a fluid. In the absence of the known relationship between the fluid velocity and the undulating surface, the boundary condition for the tracer cannot be implemented properly. Such a velocity field, when coupled to the diffusing tracer particle, can transfer energy from its undulations to the tracer. Striking a balance between diffusion and the non-equilibrium drive on the particle can result in the particle ratcheting through the fluid. Existence of such a ratcheting of a tracer particle with respect to the fluid is very important in the sense that it would be possible to drive particles in the direction opposite to fluid flow, which is the basic ingredient for the process of filtration.

In the previous chapters, we focused on transport phenomena in nanochannels, where confinement and entropic effects play a dominant role. However, the hydrodynamic ratcheting mechanism considered in this chapter relies on flow fields generated by boundary undulations,

whose strength depends sensitively on the channel width and driving frequency. In particular, the amplitude of the induced flow increases strongly with the channel radius, making the effect significantly more pronounced at the microscale. In very narrow nanochannels, these hydrodynamic effects become extremely weak within the perturbative regime considered here, thereby limiting the efficiency of ratcheting transport. For this reason, we consider a microchannel geometry in this chapter, which allows for sufficiently strong flow-induced transport while still remaining within the low-Reynolds-number regime.

The contents of this chapter are based on the work [86]. First we present the governing Navier-Stokes equation [80, 87, 81, 88] and associated boundary conditions for the cylindrical geometry of our model soft channel. Subsequently, we solve the Navier-Stokes equation under the low Reynolds number approximation to find the velocity flow field. This field provides a ratcheting potential for the dynamics of a tracer particle whose transport we investigate. Then, we numerically solve [89] the Langevin equation [90, 91] for the dynamics of the tracer in the presence of the background velocity field and thermal noise. We present a numerical simulation of the tracer particle's transport properties. Finally, we discuss our results and conclude the chapter.

5.1 Theoretical Model and Formulation

In this section, we establish the theoretical foundation for our hydrodynamic ratchet model. We start by defining the governing equations of motion and the boundary conditions that characterize the fluid-structure interaction. This formulation is the first step toward understanding how spatiotemporal surface fluctuations translate into a directed driving force for tracer particles.

5.1.1 Navier-Stokes Equation and Perturbation Analysis

In this chapter, we study the transport properties of a tracer particle in the presence of fluid velocity flow inside a microchannel with spatiotemporally undulating walls. To this end, we aim to derive the velocity flow field and the associated boundary profile in the microchannel, whose structure will serve as a ratcheting potential for the tracer particle moving within

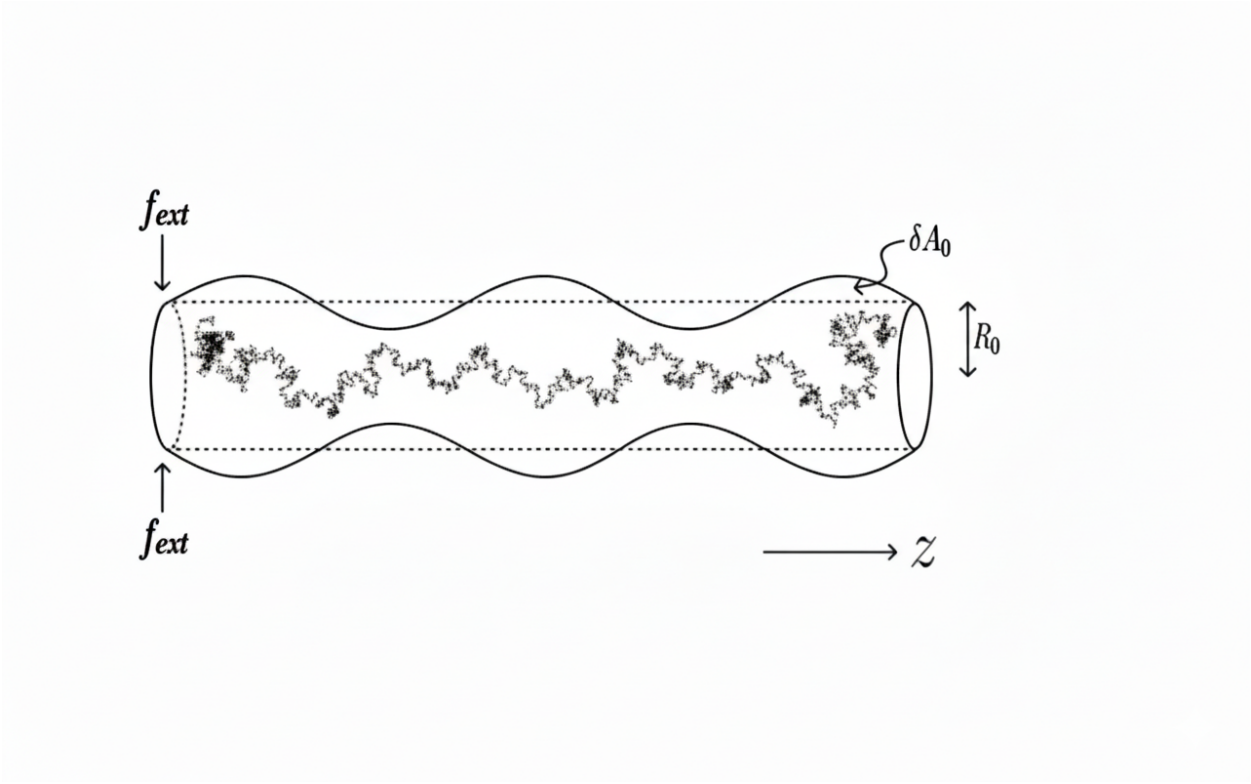

Figure 5.1: The schematic diagram of a microchannel with undulating walls that are circularly symmetric around the z-axis. The wall geometry is generated by an external forcing, and a pressure gradient is applied along the length of the tube.

this flow field. For such flows through microchannels, when surface fluctuations occur at frequencies of several tens of hertz, the flow is in a low Reynolds number regime. Based on this, a perturbation analysis of the flow is developed. The linearity of the problem allows us to analyze it analytically.

Finally, we aim to study the dynamics of a tracer particle moving under this velocity-flow field using a Langevin dynamics simulation. As shown schematically in Fig. 5.1, the model system we consider is a tracer particle evolving in a cylindrical channel of average radius R_0, whose walls, in general, can support undulations generated by oscillating one of the edges of the tube. The diameter of the tube could be about tens of micrometres. Our aim is to study the transport of a tracer particle in this flow field. Navier-Stokes equation for the velocity profile $\boldsymbol{u}(\boldsymbol{r}, t)$ of a fluid flow is

$$\rho\left(\frac{\partial \boldsymbol{u}}{\partial t} + (\boldsymbol{u}.\nabla)\boldsymbol{u}\right) = -\nabla P + \eta\nabla^2\boldsymbol{u} + \left(\frac{1}{3}\eta + \zeta\right)\nabla(\nabla.\boldsymbol{u}) + \boldsymbol{f}_{\text{ext}}, \tag{5.1}$$

supplemented with the continuity equation:

$$\frac{\partial \rho}{\partial t} + \nabla.(\rho \boldsymbol{u}) = 0. \tag{5.2}$$

Where ρ and η are, respectively, the mass density and dynamic viscosity of the fluid, and ζ is the second coefficient of viscosity of the fluid or the bulk viscosity. In Eq. 5.1, $\boldsymbol{f}_{\text{ext}}$ is the body force acting on the fluid (force per unit volume to be specific). Throughout this chapter, we assume the incompressibility of fluid (i.e., $\frac{d\rho}{dt} = 0$), which gives $\nabla.\boldsymbol{u} = 0$ due to the continuity equation. Due to this assumption, the third term in the Navier-Stokes equation drops out due to its dependence on $\nabla \cdot \boldsymbol{u}$. Thus, the above equations reduce to the following form:

$$\rho \left(\frac{\partial \boldsymbol{u}}{\partial t} + (\boldsymbol{u} \cdot \nabla)\boldsymbol{u} \right) = -\nabla P + \eta \nabla^2 \boldsymbol{u} + \boldsymbol{f}_{\text{ext}}. \tag{5.3}$$

and

$$\nabla.\boldsymbol{u} = 0. \tag{5.4}$$

We intend to solve for the velocity profile $\boldsymbol{u}$ using perturbation theory to make a comparison of different terms of the Navier-Stokes equation. We nondimensionalize the equation by introducing $r' = r/R_0$, $t' = t/\tau$ ($\tau = 2\pi/\omega$), $\boldsymbol{u}' = \boldsymbol{u}/U$ ($U = R_0/\tau = \omega R_0/2\pi$), $P' = P/P_0$ ($P_0 = \eta U/R_0$) as dimensionless variables. With dimensionless quantities, the Eq. 5.3 becomes:

$$\text{Re} \left(\frac{\partial \boldsymbol{u}'}{\partial t'} + (\boldsymbol{u}'.\nabla')\boldsymbol{u}' \right) = -\nabla' P' + \nabla'^2 \boldsymbol{u}' + \boldsymbol{f}'_{\text{ext}}, \tag{5.5}$$

where $\text{Re} = \rho U R_0/\eta = \rho \omega R_0^2/2\pi\eta$ is the Reynolds number and $\boldsymbol{f}'_{\text{ext}} = \frac{2\pi R_0}{\eta\omega} \boldsymbol{f}_{\text{ext}}$. Typical numerical values considered being $\rho \sim 10^3$ kg/m^3, $\omega \sim 10 - 100$ rad/s, $R_0 \sim 10$ μm, and $\eta \sim 10^{-3}$ Pa s, the Reynolds number is approximately $\text{Re} \sim 10^{-4} - 10^{-3}$, which is a very small number.

Since we are working in a low Reynolds number regime, Re serves as a perturbation parameter. Thus, replacing Re by ϵ Eq. 5.5 takes the shape:

$$\epsilon \left(\frac{\partial \boldsymbol{u}'}{\partial t'} + (\boldsymbol{u}'.\nabla')\boldsymbol{u}' \right) = -\nabla' P' + \nabla'^2 \boldsymbol{u}' + \boldsymbol{f}'_{\text{ext}}. \tag{5.6}$$

Moreover, the geometry of our system, being cylindrical with an undulating surface, makes it convenient to use cylindrical coordinates. In cylindrical coordinates $\boldsymbol{u} = v\hat{\boldsymbol{r}} + u\hat{\boldsymbol{z}}$ (assuming axis symmetry). By substituting expressions for Laplacian and convective derivatives in

cylindrical coordinates and separating the vector Eq. 5.6 into its component equations, we get two equations. The equation for the $\hat{\boldsymbol{z}}$-component is

$$\epsilon\left(\frac{\partial u'}{\partial t'}+u'\frac{\partial u'}{\partial z'}+v'\frac{\partial u'}{\partial r'}\right)=-\frac{\partial P'}{\partial z'}+\frac{\partial^2 u'}{\partial z'^2}+\frac{\partial^2 u'}{\partial r'^2}+\frac{1}{r'}\frac{\partial u'}{\partial r'}+f'_z, \tag{5.7}$$

and that in the $\hat{\boldsymbol{r}}$ direction is

$$\epsilon\left(\frac{\partial v'}{\partial t'}+v'\frac{\partial v'}{\partial r'}+u'\frac{\partial v'}{\partial z'}\right)=\frac{\partial^2 v'}{\partial z'^2}+\frac{\partial^2 v'}{\partial r'^2}+\frac{1}{r'}\frac{\partial v'}{\partial r'}-\frac{v'}{r'^2}+f'_r. \tag{5.8}$$

Here, we have used $\boldsymbol{f}'_{\text{ext}}=f'_r\hat{\boldsymbol{r}}+f'_z\hat{\boldsymbol{z}}$. This body force must be considered self-consistently because such a force in the bulk of the fluid would eventually be generated when the surface undulations are present. Expanding u' and v' in perturbation series:

$$u'=u'_0+\epsilon u'_1+\epsilon^2 u'_2+\ldots, \tag{5.9}$$

and

$$v'=v'_0+\epsilon v'_1+\epsilon^2 v'_2+\ldots. \tag{5.10}$$

Similarly, the radius $R(z,t)$ and external forcing $\boldsymbol{f}'_{\text{ext}}$ acting on the walls of the microchannel are expanded as:

$$R(z,t)=R_0+\epsilon R_1(z,t)+\epsilon^2 R_2(z,t)+\ldots, \tag{5.11}$$

$$f_z{}'=f_z{}'^{(0)}+\epsilon f_z{}'^{(1)}+\epsilon^2 f_z{}'^{(2)}+\ldots, \tag{5.12}$$

and

$$f_r{}'=f_r{}'^{(0)}+\epsilon f_r{}'^{(1)}+\epsilon^2 f_r{}'^{(2)}+\ldots. \tag{5.13}$$

Where R_0 is the average radius of the microchannel. ϵR_1 and $\epsilon^2 R_2$ are, respectively, the first- and second-order undulations present on the surface of the microchannel. In the context of the following analysis, the ϵR_1 component is considered created by an external agent by driving the surface at the left edge of the tube. As a result of this drive that generates flows in the fluid, the nonlinearity of the flow generates feedback oscillations $\epsilon^2 R_2$ in the second order. This is the scheme on which we base the perturbation analysis in a self-consistent manner. The details of the analysis can be found in [79].

5.1.1.1 Boundary condition for velocity fields

To uniquely determine the solution, one needs to impose appropriate boundary conditions on the velocity profile. Boundary conditions describe the fluid behavior at boundaries that the solution must obey at all times. The velocity profile $\boldsymbol{u}(\boldsymbol{r}, t)$ of the fluid satisfies the following boundary condition (known as the kinematic boundary condition [88, 80, 92]):

$$v(r = R(z,t), z, t) - u(r = R(z,t), z, t)\frac{\partial R(z,t)}{\partial z} - \frac{\partial R(z,t)}{\partial t} = 0. \tag{5.14}$$

Since the boundary of the soft elastic tube undulates, the kinematic boundary condition must be adopted, which sets the relative velocity of the fluid at the boundary to zero, allowing the boundary layers to follow boundary modes.

5.1.1.2 Steady flow at Zeroth order

For the sake of completeness, let us first look at the zeroth-order structure of the solution. At zeroth order, the system describes a steady, pressure-driven flow in a rigid, uniform channel. We assume that forces f_r and f_z, induced by boundary fluctuations, are an order of magnitude smaller than the pressure gradient because these forces are generated by surface undulations of order ϵR_1. The leading order transport of fluid is due to the pressure gradient. Using Eq. 5.7 and 5.8 one can write out the zeroth order equations:

$$-\frac{\partial P'}{\partial z'} + \frac{\partial^2 u_0'}{\partial z'^2} + \frac{\partial^2 u_0'}{\partial r'^2} + \frac{1}{r'}\frac{\partial u_0'}{\partial r'} = 0, \tag{5.15}$$

and

$$\frac{\partial^2 v_0'}{\partial z'^2} + \frac{\partial^2 v_0'}{\partial r'^2} + \frac{1}{r'}\frac{\partial v_0'}{\partial r'} - \frac{v_0'}{r'^2} = 0. \tag{5.16}$$

Now, zeroth-order equations solve for steady flow along the z-direction in a much simpler setting

$$\frac{\partial u_0'}{\partial z'} = 0\ ,\ \frac{\partial^2 u_0'}{\partial z'^2} = 0,\ \text{and}\ v_0' = 0. \tag{5.17}$$

Thus, the equation for u_0' becomes:

$$-\frac{\partial P'}{\partial z'} + \frac{\partial^2 u_0'}{\partial r'^2} + \frac{1}{r'}\frac{\partial u_0'}{\partial r'} = 0. \tag{5.18}$$

Assuming a constant pressure gradient, solving the equation above yields the following result:

$$u_0' = C_1 + \frac{1}{4}\frac{\partial P'}{\partial z'} r'^2, \tag{5.19}$$

where C_1 is the integration constant. Restoring the dimensions of various quantities, we have:

$$\begin{aligned} u_0 &= U u_0' \\ &= U\left(C_1 + \frac{1}{4\eta}\frac{\partial P}{\partial z}\frac{R_0}{P_0} r^2 \frac{1}{R_0^2}\right) \\ &= C_2 + \frac{1}{4\eta}\frac{\partial P}{\partial z} r^2. \end{aligned} \tag{5.20}$$

Since $v_0' = 0$, we have

$$v_0 = 0, \tag{5.21}$$

where the direction of the longitudinal flow is determined by the pressure head, which could be chosen in either direction in order to make the direction of the bulk flow opposite to the direction of the surface-driven flow profile. Now, instead of imposing the classical no-slip boundary condition on the channel wall, we consider the presence of a finite slip [93, 94, 95, 96]. This choice is not only physically more realistic for microconfined flows, but it will also remove divergence (t dependent growth in the expression of $R_1(z,t)$) that would otherwise arise in the boundary profile. Accordingly, the velocity field is expressed as the sum of two contributions: the first part corresponds to the usual Poiseuille component, which vanishes at the wall, while the second part accounts for the finite slip velocity v_{slip} that remains nonzero at the boundary.

$$u_0 = -\frac{1}{4\eta}\frac{\partial P}{\partial z}\left(R_0^2 - r^2\right) + v_{\text{slip}}. \tag{5.22}$$

The continuity equation at zeroth order is

$$\frac{1}{r}\frac{\partial}{\partial r}(r v_0) + \frac{\partial u_0}{\partial z} = 0. \tag{5.23}$$

With these expressions for u_0 and v_0, the zeroth-order continuity equation trivially satisfies, as the pressure gradient $\partial P/\partial z$ is a constant. All of these are quite well-known results [79].

5.1.1.3 First order equations

The first order equations obtained from Eq. 5.7 and 5.8 are:

$$\frac{\partial^2 u_1'}{\partial z'^2} + \frac{\partial^2 u_1'}{\partial r'^2} + \frac{1}{r'}\frac{\partial u_1'}{\partial r'} = -{f_z}'^{(1)}, \tag{5.24}$$

and

$$\frac{\partial^2 v_1'}{\partial z'^2} + \frac{\partial^2 v_1'}{\partial r'^2} + \frac{1}{r'}\frac{\partial v_1'}{\partial r'} - \frac{v_1'}{r'^2} = -{f_r}'^{(1)}, \tag{5.25}$$

where ${f_z}'^{(1)}$ and ${f_r}'^{(1)}$, respectively, represent the components z and r of the dimensionless forces (per unit volume) experienced by the fluid due to the surface undulations present on the walls of the microchannel.

Instead of defining the forces and solving for the velocity, we adopt the inverse approach. We prescribe a desired time-dependent velocity profile u_1' that can act as a ratcheting potential for a tracer particle and then use Eq. 5.24 and 5.25 to determine the corresponding forces required to generate it in a self-consistent manner. To act as a ratcheting potential, we must choose a velocity field u_1' to be of a spatially inversion symmetric broken form modulated by time undulations, which will drive the system out of equilibrium. We do this by using the minimal coupling of the first two spatial harmonics of a sinusoidal wave, which leads to the following form:

$$u_1'(r', z', t') = C_1' \sin(\omega' t' + \phi) \cos(\omega' t') \times \Big(\cos(2k' z') - 2\cos(k' z')\Big). \tag{5.26}$$

Where $k' = kR_0$ and $\omega' = 2\pi$ as usual. Note that the linearity of Eq. 5.24 and 5.25 allows us to consider the velocity profile as a superposition of modes, and here lies the merit of the analytical method that we have developed.

Now, the continuity equation at first order is the following:

$$\frac{1}{r'}\frac{\partial}{\partial r'}(r' v_1') + \frac{\partial u_1'}{\partial z'} = 0. \tag{5.27}$$

Using the expression for u_1', we can integrate the continuity equation to find the corresponding radial velocity component v_1', which is given by

$$v_1' = C_1' k' r' \sin(\omega' t' + \phi) \cos(\omega' t') \times \Big(\sin(2k' z') - \sin(k' z')\Big). \tag{5.28}$$

Restoring the dimensions and absorbing the dimensionless constant C_1' in the characteristic velocity scale $U = \omega R_0/2\pi$, we get the following expressions for the first-order velocity fields.

$$u_1(r,z,t) = U\ \sin(\omega t+\phi)\ \cos(\omega t) \times \Big(\cos(2kz) - 2\cos(kz)\Big), \tag{5.29}$$

and

$$v_1(r,z,t) = kr\,U\ \sin(\omega t+\phi)\ \cos(\omega t) \times \Big(\sin(2kz) - \sin(kz)\Big). \tag{5.30}$$

Finally, the velocity fields in the channel are given by

$$u(r,z,t) = -\frac{1}{4\eta}\frac{\partial P}{\partial z}(R_0^2 - r^2) + v_{\text{slip}} + \text{Re}\frac{\omega R_0}{2\pi}\ \sin(\omega t+\phi)\ \cos(\omega t)\Big(\cos(2kz) - 2\cos(kz)\Big), \tag{5.31}$$

and

$$v(r,z,t) = \text{Re}\ kr\ \frac{\omega R_0}{2\pi}\ \sin(\omega t+\phi)\ \cos(\omega t)\Big(\sin(2kz) - \sin(kz)\Big). \tag{5.32}$$

Where, $\text{Re} = \rho\omega R_0^2/2\pi\eta$. To self consistently determine the forces ${f_z}'^{(1)}$ and ${f_r}'^{(1)}$ we substitute the expression of u_1' and v_1' in Eq. 5.24 and 5.25 respectively and we get:

$${f_z}'^{(1)} = 2C_1'k'^2 \sin(\omega' t' + \phi)\cos(\omega' t')\Big[\,2\cos(2k'z') - \cos(k'z')\,\Big], \tag{5.33}$$

and

$${f_r}'^{(1)} = C_1'k'^3 r' \sin(\omega' t' + \phi)\cos(\omega' t')\Big[\,4\sin(2k'z') - \sin(k'z')\,\Big], \tag{5.34}$$

which are quite regular and devoid of singularity. Restoring the dimensions in the above equations gives:

$$f_z^{(1)} = 2\,\eta\,Uk^2\ \sin(\omega t+\phi)\cos(\omega t)\Big[\,2\cos(2kz) - \cos(kz)\,\Big], \tag{5.35}$$

and

$$f_r^{(1)} = \eta\,Uk^3 r\ \sin(\omega t+\phi)\cos(\omega t)\Big[\,4\sin(2kz) - \sin(kz)\,\Big]. \tag{5.36}$$

It should be noted that the first order velocities u_1 and v_1 together with the above determined forces $f_z^{(1)}$, $f_r^{(1)}$ and $R_1(z,t)$ (determined in the next section) close the system in a consistent way. Physically, these body forces originate from externally driven surface undulations, and the fluid inside the microchannel responds by developing the corresponding velocity fields shown above.

5.1.1.4 First-order Radius Correction

The first-order kinematic boundary condition is as follows.

$$v_1(r = R_0, z, t) - u_0(r = R_0, z, t)\frac{\partial R_1(z,t)}{\partial z} - u_1(r = R_0, z, t)\frac{\partial R_0}{\partial z} - \frac{\partial R_1(z,t)}{\partial t} = 0. \quad (5.37)$$

Since R_0 is constant, the third term in the above equation is zero. Substituting the expression of various quantities, we get the following equation:

$$v_{\text{slip}}\frac{\partial R_1(z,t)}{\partial z} + \frac{\partial R_1(z,t)}{\partial t} = kR_0U\ \sin(\omega t + \phi)\cos(\omega t)\Big(\sin(2kz) - \sin(kz)\Big). \quad (5.38)$$

This is a first-order linear partial differential equation in $R_1(z,t)$. To solve this PDE, we use the method of characteristics [97, 98]. For a detailed discussion of the method of characteristics, the reader is advised to refer to Appendix C. The characteristic equations are given by:

$$\frac{dz}{d\tau} = v_{\text{slip}}, \quad (5.39)$$

and

$$\frac{dt}{d\tau} = 1. \quad (5.40)$$

The solutions of the above equations are as follows:

$$z(\tau) = v_{\text{slip}}\,\tau + C_1, \quad (5.41)$$

and

$$t(\tau) = \tau + C_2. \quad (5.42)$$

Thus, the characteristic line is given by:

$$z - v_{\text{slip}}t = C(= C_1 - v_{\text{slip}}C_2). \quad (5.43)$$

Along these characteristic lines, the partial differential equation reduces to the following ordinary differential equation for R_1:

$$\frac{dR_1}{dt} = \beta \sin(\omega t + \phi)\cos(\omega t)\Big[\sin(2k(v_{\text{slip}}t + \zeta)) - \sin(k(v_{\text{slip}}t + \zeta))\Big]. \tag{5.44}$$

Where $\beta = kUR_0$. The solution of Eq. (5.44) is:

$$R_1(v_{\text{slip}}t+\zeta, t) = \beta \int_0^t d\tau \sin(\omega\tau+\phi)\cos(\omega\tau)\Big[\sin(2k(v_{\text{slip}}\tau+\zeta)) - \sin(k(v_{\text{slip}}\tau+\zeta))\Big]. \tag{5.45}$$

Now, replacing ζ by $z - v_{\text{slip}}t$, we get:

$$R_1(z,t) = \beta \int_0^t d\tau \ \sin(\omega\tau + \phi)\ \cos(\omega\tau) \times \Big[\sin\big(2k(z - v_{\text{slip}}(t-\tau))\big) - \sin\big(k(z - v_{\text{slip}}(t-\tau))\big)\Big]. \tag{5.46}$$

Using the identity,

$$\sin A \cos B = \frac{1}{2}(\sin(A+B) + \sin(A-B)), \tag{5.47}$$

we get

$$R_1(z,t) = \frac{\beta}{2}\int_0^t d\tau \ \Big(\sin\phi + \sin(2\omega\tau + \phi)\Big)\Big[\sin(a_2 + b_1\tau) - \sin(a_1 + b_1\tau)\Big], \tag{5.48}$$

where,

$$a_2 = 2kz - 2kv_{\text{slip}}t, \tag{5.49}$$
$$b_2 = 2kv_{\text{slip}}, \tag{5.50}$$
$$a_1 = kz - kv_{\text{slip}}t, \tag{5.51}$$

and

$$b_1 = kv_{\text{slip}}. \tag{5.52}$$

By defining

$$S(t; a, b) = \int_0^t \sin(a + b\tau)\ d\tau, \tag{5.53}$$

and

$$K(t;a,b) = \int_0^t \sin(2\omega\tau + \phi)\sin(a + b\tau)\, d\tau, \tag{5.54}$$

We get the following

$$R_1(z,t) = \frac{\beta}{2}\Big\{\sin\phi\,\Big[S(t;a_2,b_2) - S(t;a_1,b_1)\Big] + \Big[K(t;a_2,b_2) - K(t;a_1,b_1)\Big]\Big\}. \tag{5.55}$$

Where the S-integral is

$$S(t;a,b) = \frac{\cos a - \cos(a+bt)}{b}. \tag{5.56}$$

And the K-integral reads

$$K(t;a,b) = \frac{1}{2}\int_0^t \Big(\cos\big((2\omega - b)\tau + \phi - a\big) - \cos\big((2\omega + b)\tau + \phi + a\big)\Big)\, d\tau. \tag{5.57}$$

Solving the above gives:

$$K(t;a,b) = \frac{1}{2}\Bigg(\frac{\sin\big((2\omega - b)t + \phi - a\big) - \sin(\phi - a)}{2\omega - b} - \frac{\sin\big((2\omega + b)t + \phi + a\big) - \sin(\phi + a)}{2\omega + b}\Bigg). \tag{5.58}$$

Writing $\Omega = kv_{\text{slip}}$, we get the following analytical expression for $R_1(z,t)$.

$$\begin{aligned} R_1(z,t) = \frac{\beta}{2}\Big\{&\sin\phi\,\frac{\cos\big(2kz - 2\Omega t\big) - \cos(2kz)}{2\,\Omega} - \sin\phi\,\frac{\cos\big(kz - 2\Omega t\big) - \cos(kz)}{\Omega} \\ &+ \frac{1}{2}\Big[\frac{\sin(2\omega t - 2kz + \phi) + \sin(2kz - 2\Omega t - \phi)}{2\omega - 2\Omega} + \frac{\sin(2\omega t + 2kz + \phi) - \sin(2kz - 2\Omega t + \phi)}{2\omega + 2\Omega} \\ &+ \frac{\sin(2\omega t - kz + \phi) + \sin(kz - \Omega t - \phi)}{2\omega - \Omega} + \frac{\sin(2\omega t + kz + \phi) - \sin(kz - \Omega t + \phi)}{2\omega + \Omega}\Big]\Big\}. \end{aligned} \tag{5.59}$$

At this point, it is interesting to check what happens to the above expression of $R_1(z,t)$ when the slip velocity v_{slip} vanishes. In the limit $v_{\text{slip}} \to 0$, the last four terms of the above expression remain finite, whereas the first two terms grow in time, obtained using L'Hôpital's

rule to evaluate the limit.

$$\lim_{\Omega\to 0} R_1 = \frac{\beta}{2}\Bigg\{ t\,\sin\phi\Big[\sin(2kz) - 2\sin(kz)\Big] + \frac{1}{4\omega}\Big[\sin(2\omega t - 2kz + \phi) + \sin(2kz - \phi) + \sin(2\omega t + 2kz + \phi) - \sin(2kz + \phi) + \sin(2\omega t - kz + \phi) + \sin(kz - \phi) + \sin(2\omega t + kz + \phi) - \sin(kz + \phi)\Big]\Bigg\}. \tag{5.60}$$

Thus, the model yields an unphysical result in the limit of zero slip velocity. Specifically, as $v_{\text{slip}} \to 0$, the expression for $R_1(z,t)$ shows unbounded temporal growth. Consequently, the existence of a finite slip velocity is a key physical necessity in such situations. After rearranging the above equation and substituting $\beta = kUR_0$ we obtain:

$$R_1(z,t) = \frac{kUR_0}{2\Omega}\Bigg\{\sin\phi\,\frac{\cos\big(2kz - 2\Omega t\big) - \cos(2kz)}{2} - \sin\phi\,\frac{\cos\big(kz - 2\Omega t\big) - \cos(kz)}{1} + \frac{1}{2}\Bigg[\frac{\sin(2\omega t - 2kz + \phi) + \sin(2kz - 2\Omega t - \phi)}{2(\omega/\Omega - 1)} + \frac{\sin(2\omega t + 2kz + \phi) - \sin(2kz - 2\Omega t + \phi)}{2(\omega/\Omega + 1)} + \frac{\sin(2\omega t - kz + \phi) + \sin(kz - \Omega t - \phi)}{2(\omega/\Omega - 1/2)} + \frac{\sin(2\omega t + kz + \phi) - \sin(kz - \Omega t + \phi)}{2(\omega/\Omega + 1/2)}\Bigg]\Bigg\}. \tag{5.61}$$

Substituting $U = \omega R_0/2\pi$ we get,

$$R_1(z,t) = \frac{\omega R_0^2}{4\pi v_{\text{slip}}}\Bigg\{\frac{1}{2}\sin\phi\,\big(\cos\big(2kz - 2\Omega t\big) - \cos(2kz)\big) - \sin\phi\,\big(\cos\big(kz - 2\Omega t\big) - \cos(kz)\big) + \frac{1}{4}\Bigg[\frac{\sin(2\omega t - 2kz + \phi) + \sin(2kz - 2\Omega t - \phi)}{(\omega/\Omega - 1)} + \frac{\sin(2\omega t + 2kz + \phi) - \sin(2kz - 2\Omega t + \phi)}{(\omega/\Omega + 1)} + \frac{\sin(2\omega t - kz + \phi) + \sin(kz - \Omega t - \phi)}{(\omega/\Omega - 1/2)} + \frac{\sin(2\omega t + kz + \phi) - \sin(kz - \Omega t + \phi)}{(\omega/\Omega + 1/2)}\Bigg]\Bigg\}. \tag{5.62}$$

Thus, the boundary profile $R(z,t)$ is given by:

$$R(z,t) = R_0 + \text{Re}\; R_1(z,t), \tag{5.63}$$

where $R_1(z,t)$ is given by the Eq. 5.62. From above, the amplitude of surface undulations

δA_0 can be read off as $\delta A_0 = \mathrm{Re}\,\omega R_0^2/4\pi v_{\mathrm{slip}}$. Thus,

$$\delta A_0 = \frac{\rho\omega^2 R_0^4}{8\pi^2\eta v_{\mathrm{slip}}}. \tag{5.64}$$

One may rewrite $R_1(z,t)$ in the form

$$R_1(z,t) = \frac{\beta}{2}\Big[\cos(2kz)\,G_1(t) + \sin(2kz)\,G_2(t) + \cos(kz)\,H_1(t) + \sin(kz)\,H_2(t)\Big] \tag{5.65}$$

where

$$G_1(t) = \sin\phi\,\frac{\cos(2\Omega t)-1}{2\Omega} + \frac{1}{2}\left[\frac{\sin(2\omega t+\phi)-\sin(2\Omega t+\phi)}{2\omega-2\Omega} + \frac{\sin(2\omega t+\phi)+\sin(2\Omega t-\phi)}{2\omega+2\Omega}\right], \tag{5.66}$$

$$G_2(t) = \sin\phi\,\frac{\sin(2\Omega t)}{2\Omega} + \frac{1}{2}\left[\frac{\cos(2\Omega t+\phi)-\cos(2\omega t+\phi)}{2\omega-2\Omega} + \frac{\cos(2\omega t+\phi)-\cos(2\Omega t-\phi)}{2\omega+2\Omega}\right], \tag{5.67}$$

$$H_1(t) = -\sin\phi\,\frac{\cos(\Omega t)-1}{\Omega} + \frac{1}{2}\left[\frac{\sin(2\omega t+\phi)-\sin(\Omega t+\phi)}{2\omega-\Omega} + \frac{\sin(2\omega t+\phi)+\sin(\Omega t-\phi)}{2\omega+\Omega}\right], \tag{5.68}$$

$$H_2(t) = -\sin\phi\,\frac{\sin(\Omega t)}{\Omega} + \frac{1}{2}\left[\frac{\cos(\Omega t+\phi)-\cos(2\omega t+\phi)}{2\omega-\Omega} + \frac{\cos(2\omega t+\phi)-\cos(\Omega t-\phi)}{2\omega+\Omega}\right]. \tag{5.69}$$

5.1.2 Langevin Model for Tracer Dynamics

5.1.2.1 Overdamped Langevin Equation

To model the dynamics of a microscopic tracer particle suspended in the fluid, we employ the Langevin framework. This approach treats the particle's motion as a combination of

deterministic drag from the surrounding fluid and stochastic fluctuations. The equation of motion is given by:

$$m\frac{d\boldsymbol{u}_p(t)}{dt} = -\gamma(\boldsymbol{u}_p(t) - \boldsymbol{u}(\boldsymbol{r}_p(t), t)) + \sqrt{2\gamma k_B T}\boldsymbol{\xi}(t). \tag{5.70}$$

Where γ is the damping constant of the tracer particle in the fluid, T is the temperature, and k_B is the Boltzmann constant. Here $\boldsymbol{\xi}(t) = (\xi_r(t), \xi_\theta(t), \xi_z(t))$ represents the noise vector whose components are delta-correlated stationary Gaussian processes with zero mean, satisfying:

$$\langle \boldsymbol{\xi}(t) \rangle = 0, \tag{5.71}$$

and

$$\langle \xi_i(t)\, \xi_j(t') \rangle = \delta_{ij}\, \delta(t - t'), \qquad i, j \in \{r, \theta, z\}. \tag{5.72}$$

Here, $\boldsymbol{u}_p(t)$ is the velocity of the tracer and $\boldsymbol{u}(\boldsymbol{r}_p(t), t)$ denotes the velocity of fluid flow being evaluated at the position of the tracer particle $\boldsymbol{r}_p(t)$. Since we are working in the low Reynolds number regime, we take the overdamped limit of the Langevin equation, in which the inertial term on the left-hand side vanishes, reducing the equation to:

$$0 = -\gamma(\boldsymbol{u}_p(t) - \boldsymbol{u}(\boldsymbol{r}_p(t), t)) + \sqrt{2\gamma k_B T}\boldsymbol{\xi}(t). \tag{5.73}$$

Here, we can identify the particle's translational diffusion coefficient, D_0, through the Stokes-Einstein relation as $D_0 = k_B T/\gamma$. The use of this relation is justified because ratcheting in a Low Reynolds number fluid flow is a weakly non-equilibrium phenomenon. The equation can then be written as:

$$\frac{d\boldsymbol{r}_p(t)}{dt} = \boldsymbol{u}(\boldsymbol{r}_p(t), t)) + \sqrt{2D_0}\boldsymbol{\xi}(t). \tag{5.74}$$

Writing down the above vector equation in component cylindrical coordinates, we get:

$$\frac{dz_p(t)}{dt} = u_z\big(r_p(t), z_p(t), t\big) + \sqrt{2D_0}\,\xi_z(t), \tag{5.75}$$

$$\frac{dr_p(t)}{dt} = u_r\big(r_p(t), z_p(t), t\big) + \frac{D_0}{r_p} + \sqrt{2D_0}\,\xi_r(t), \tag{5.76}$$

$$\frac{d\theta_p(t)}{dt} = \sqrt{\frac{2D_0}{r_p^2}}\,\xi_\theta(t). \tag{5.77}$$

Note that the radial equation Eq. 5.87 includes a term D_0/r_p (where $D_0 = k_B T/\gamma$). This is not an external potential, but a known geometric correction that appears when interpreting

a stochastic differential equation [99, 100] in curvilinear coordinates. This is known as the geometric Itô correction [101, 102]. The Fokker-Planck equation [101, 100, 102] corresponding to the above Langevin equation is given by:

$$\frac{\partial P(\boldsymbol{r},t)}{\partial t} = -\nabla \cdot (\boldsymbol{u}(\boldsymbol{r},t)P(\boldsymbol{r},t)) + D_0 \nabla^2 P(\boldsymbol{r},t), \tag{5.78}$$

with probability current $\boldsymbol{J}(\boldsymbol{r},t)$ given by:

$$\boldsymbol{J}(\boldsymbol{r},t) = \boldsymbol{u}(\boldsymbol{r},t)P(\boldsymbol{r},t) - D_0 \nabla^2 P(\boldsymbol{r},t). \tag{5.79}$$

Expanding the above Fokker-Planck equation in cylindrical coordinates and assuming azimuthal symmetry for the probability distribution $P(r,z,t)$, gives:

$$\frac{\partial P}{\partial t} = -\frac{1}{r}\frac{\partial}{\partial r}\left(r u_r P\right) - \frac{\partial}{\partial z}\left(u_z P\right) + D_0 \left[\frac{1}{r}\frac{\partial}{\partial r}\left(r\frac{\partial P}{\partial r}\right) + \frac{\partial^2 P}{\partial z^2}\right]. \tag{5.80}$$

The Itô correction term, which appears as an explicit drift of magnitude D_0/r in the radial Langevin equation, is not an added term in the Fokker-Planck equation. Instead, it is implicitly contained within the mathematical form of the Laplacian operator (∇^2) in cylindrical coordinates. To show this, we can expand the radial part of the diffusive term from Eq. 5.78:

$$\begin{aligned} D_0 \nabla_r^2 P &= D_0 \frac{1}{r}\frac{\partial}{\partial r}\left(r\frac{\partial P}{\partial r}\right) \\ &= D_0 \frac{1}{r}\left(\frac{\partial P}{\partial r} + r\frac{\partial^2 P}{\partial r^2}\right) \\ &= \underbrace{\frac{D_0}{r}\frac{\partial P}{\partial r}}_{\substack{\text{This term has the form} \\ \text{of a drift}}} + \underbrace{D_0 \frac{\partial^2 P}{\partial r^2}}_{\substack{\text{Standard diffusion.} \\ \text{term}}}. \end{aligned}$$

As shown above, the expansion of the Laplacian in cylindrical coordinates naturally splits into two parts. The second term is the standard form for diffusion. However, the first term has the mathematical structure of a drift term from the Fokker-Planck equation. This shows that an effective drift velocity $= D_0/r$ arises purely from the geometry of the coordinate system. A detailed discussion of the geometric drift term $1/r$, which emerges when expressing diffusion in cylindrical coordinates, can be found in standard references on stochastic processes (see, e.g., [102, 101, 103]).

5.1.2.2 Boundary condition for tracer particle

For a tracer particle confined within an impermeable channel, a reflecting boundary condition is imposed on the walls. This physically ensures that no particle can cross the boundary, and thus the total probability $P(\boldsymbol{r},t)$ of finding the particle inside the channel is conserved. Mathematically, this is expressed by stating that the component of the probability current $\boldsymbol{J}(\boldsymbol{r},t)$, that is normal (perpendicular) to the boundary surface, must be zero.

$$\boldsymbol{J}(\boldsymbol{r},t)\cdot\boldsymbol{n}=0 \quad \text{at the boundary } r=R(z,t), \tag{5.81}$$

where $\boldsymbol{n}$ is the unit vector normal to the channel wall. Substituting the definition of the probability current, $\boldsymbol{J}=\boldsymbol{u}P-D_0\nabla P$, gives the full form of the boundary condition:

$$[\boldsymbol{u}(\boldsymbol{r},t)P(\boldsymbol{r},t)-D_0\nabla P(\boldsymbol{r},t)]\cdot\boldsymbol{n}=0. \tag{5.82}$$

5.1.2.3 Equations of Motion for Simulations

The dynamics of the particle are given by:

$$\frac{dz_p}{dt}=u_0\big(r_p(t),z_p(t),t\big)+\mathrm{Re}\;u_1\big(r_p(t),z_p(t),t\big)+\sqrt{2D_0}\,\xi_z(t), \tag{5.83}$$

$$\frac{dr_p}{dt}=\mathrm{Re}\;v_1\big(r_p(t),z_p(t),t\big)+\frac{D_0}{r_p(t)}+\sqrt{2D_0}\,\xi_r(t), \tag{5.84}$$

$$\frac{d\theta_p}{dt}=\sqrt{\frac{2D_0}{r_p(t)^2}}\,\xi_\theta(t). \tag{5.85}$$

Substituting the expression of various terms, we get the following.

$$\begin{aligned}\frac{dz_p}{dt}&=-\frac{1}{4\eta}\frac{\partial P}{\partial z}\,(R_0^2-r_p^2)+v_{\text{slip}}\\&\quad+\mathrm{Re}\frac{\omega R_0}{2\pi}\sin(\omega t+\phi)\cos(\omega t)\big[\cos(2kz_p)-2\cos(kz_p)\big]+\sqrt{2D_0}\,\xi_z(t),\end{aligned} \tag{5.86}$$

$$\frac{dr_p}{dt}=\mathrm{Re}\;kr_p\frac{\omega R_0}{2\pi}\sin(\omega t+\phi)\cos(\omega t)\big[\sin(2kz_p)-\sin(kz_p)\big]+\frac{D_0}{r_p}+\sqrt{2D_0}\,\xi_r(t), \tag{5.87}$$

$$\frac{d\theta_p}{dt}=\sqrt{\frac{2D_0}{r_p^2}}\,\xi_\theta(t). \tag{5.88}$$

Equations 5.86, 5.87, and 5.88 are our working equations for numerical simulations.

5.2 Numerical Results

Let us simulate the above equations of motion for a tracer particle confined in an undulating microchannel to demonstrate that the tracer particle is transported entirely due to the symmetry-broken structure of the fluid flow field.

5.2.1 Hydrodynamic Ratcheting of the Tracer Particle

To investigate the transport properties of the tracer particle under the influence of the undulating walls, we performed numerical simulations [89] of the overdamped Langevin equations. The fluid velocity field is given by zeroth-order and first-order contributions as given in Eq. 5.31 and 5.32. To illustrate the effect of surface undulations along with the boundary, we have taken into account only the first-order correction of the velocity fields to simulate the dynamics of the tracer particle taking into account that the position of the tracer particle is bounded by the walls of the channel by a purely reflecting boundary condition, whose analytical expression is given by Eq. 5.62 and 5.63.

It should be noted that in this chapter, we have considered purely reflecting boundary conditions for the tracer particle, whereas in real situations, the boundary condition can be more complex, including partially absorbing and partially reflecting types, depending on the channel wall structure. But for the sake of simplicity, at the first stage of reporting the procedure, we have considered here only the purely reflecting boundary condition. In Fig. 5.2, we show the dynamics of a tracer particle inside the channel as obtained from the simulation of Eq. 5.86, 5.87, and 5.88 in the presence of a velocity field only due to surface undulations and noise. The simulation time step is set to $\Delta t = 10^{-4}\,\mathrm{s}$, and we employ the Euler-Maruyama method for numerical integration. We have calculated the tracer particle's velocity by averaging over 1000 realizations.

In Fig. 5.2(a), we have plotted the evolution of the longitudinal coordinate z of the tracer particle. It clearly shows the main result of our work. Surface undulations generating an inversion-symmetry-broken velocity field in a confined channel can act as a ratcheting

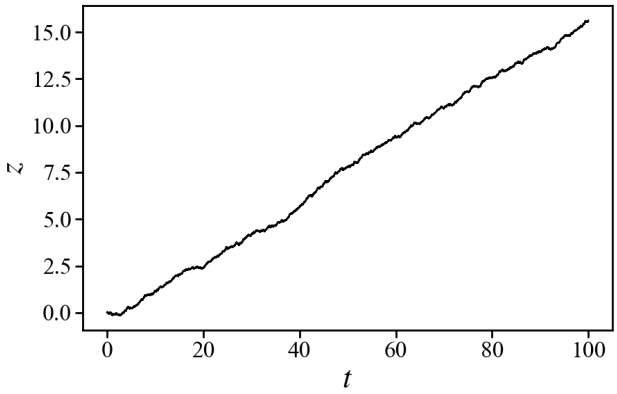

(a)

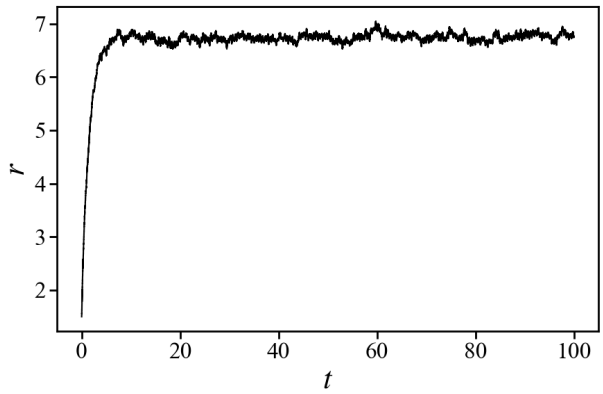

(b)

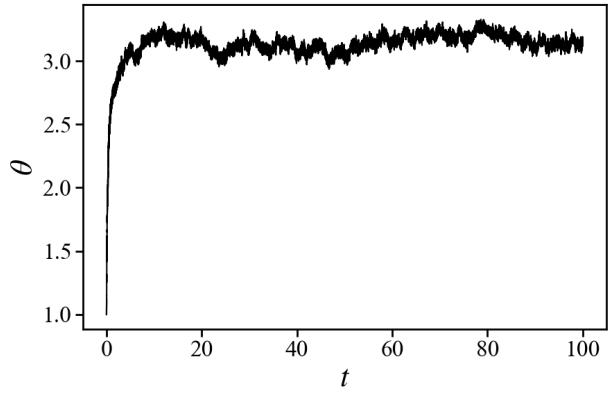

(c)

Figure 5.2: Trajectory of a tracer particle in cylindrical coordinates. The simulation parameters used are: $\omega = 70$ rad $\mathrm{s}^{-1}, \lambda = 1.0$ μm, $R_0 = 10$ μm, $D_0 = 1.0$ $\mu\mathrm{m}^2$ $\mathrm{s}^{-1}, v_{\mathrm{slip}} = 1.0$ μm $\mathrm{s}^{-1}, \phi = -\pi/2$ rad. (a) Axial coordinate z (in μm) as a function of time t (in sec), showing the net drift of the particle. (b) Radial coordinate r (in μm) as a function of time t (in sec). (c) Angular coordinate θ (in radians) as a function of time t (in sec).

mechanism. The velocity obtained from the simulation is approximately 0.15 μm/s. The next Fig. 5.2(b) shows the evolution of the radial (r) coordinate. It can be seen that the particle's radial coordinate evolves away from the axis of the channel, which is what is expected from Eq. 5.87 for a cylindrical channel. The term $1/r$ acts as a negative logarithmic potential ($\propto -\ln r$) for the evolution of the radial coordinate of the tracer particle, pushing the particle away from the axis of the channel. Similarly, the evolution of the angular coordinate (θ) with time is shown in Fig. 5.2(c). The time evolution of the ensemble-averaged angular coordinate shows a saturation at long times. However, it is essential to note that this behavior does not indicate true confinement of the angular variable. The angular dynamics are governed by a pure diffusive process, with the effective diffusion coefficient determined by the tracer particle's radial coordinate. This radial dependence reduces the rate at which the angular coordinate spreads over the whole angular range. Consequently, upon averaging over a large number of realizations (here, 1000 ensembles), the symmetric diffusive spreading around the initial angle leads to an apparent saturation of the mean angular displacement. This apparent confinement is therefore a statistical artifact of ensemble averaging and slow diffusion, rather than a physical localization mechanism. The parameter values used in the simulations are $\omega = 70$ rad s^{-1}, $\lambda = 1.0$ μm, $R_0 = 10$ μm, $D_0 = 1.0$ μm^2 s^{-1}, $v_{\text{slip}} = 1.0$ μm s^{-1} and $\phi = -\pi/2$ rad. The drag coefficient (or damping coefficient) γ for the dynamics of a tracer particle in the fluid can be written in terms of the radius a of the tracer particle, the dynamic viscosity η of the fluid, by the Stokes formula: $\gamma = 6\pi\eta a$. The value of $D_0 = 1.0\,\mu\text{m}^2\text{s}^{-1}$ can be used to interpret the size of a tracer particle using the Stokes-Einstein relation, $D_0 = \frac{k_B T}{6\pi\eta a}$. For a particle in water at $T = 300\,\text{K}$ (where $\eta \approx 10^{-3}\,\text{Pa}\cdot\text{s}$), this diffusion coefficient corresponds to a hydrodynamic radius of $a \approx 0.22\,\mu\text{m}$.

We can use these parameters to calculate the amplitude δA_0 of channel wall undulations using Eq. 5.64, which yields ~ 0.6 μm.

5.2.2 Parametric Dependence of Ratcheting Velocity

Next, we study the variation of the ratcheting speed with external forcing parameter, that is, frequency ω. In Fig. 3.5(d), we show the variation of ratcheting speed $\langle v \rangle$ with the frequency ω of the surface undulations. The simulation parameters used are: $R_0 = 10$ μm, $v_{\text{slip}} = 1.0$ μm s^{-1}, $\lambda = 1.0$ μm, $\phi = -\pi/2$, $D_0 = 1.0$ μm^2 s^{-1}. We find that the ratcheting speed increases with the increase in frequency of undulations. In this analysis, the angular

frequency ω is varied from 0 to 75 rad/sec. We chose this range because exceeding this limit would cause the ω dependent terms, specifically the first-order velocity correction and surface undulation amplitude u_1 in Eq. 5.31 and 5.64 respectively, to become too large, thereby violating the assumptions of the perturbation method.

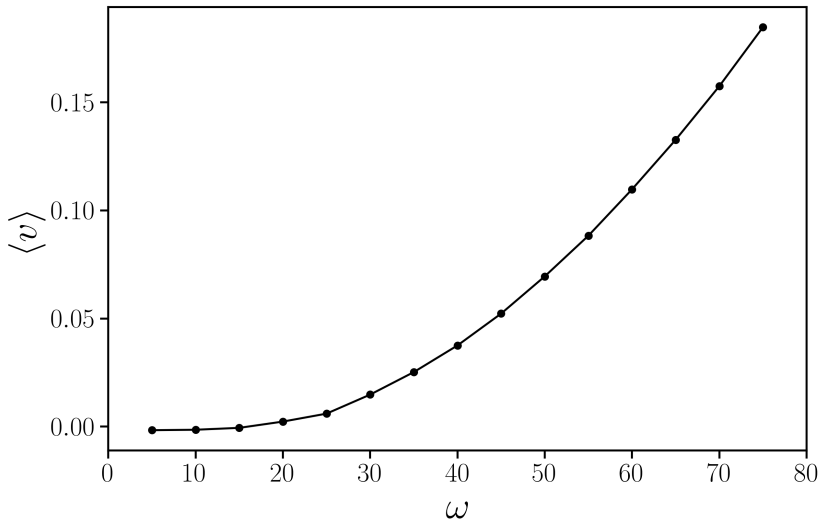

Figure 5.3: Variation of average velocity with the frequency of wall undulations ($\langle v \rangle$ in μm s^{-1}, ω in rad s^{-1}). Parameters: $R_0 = 10$ μm, $v_{\text{slip}} = 1.0$ μm s^{-1}, $\lambda = 1.0$ μm, $\phi = -\pi/2$, $D_0 = 1.0$ μm^2 s^{-1}.

A note about the condition for ratcheting is in place here. The condition of ratcheting is that the diffusive length of the tracer particle, that is, the distance covered by the tracer particle in one time period of oscillation, should be of the order of the wavelength of undulations. This condition on the parameters ω, k, and D_0 translates into $\omega \sim k^2 D_0$, where the exact formula depends on the details of the symmetry-broken waveform. Thus, ω and λ follow an inverse relationship for the ratcheting, meaning the ratcheting speed increases with an increase in ω but decreases with an increase in λ. In Fig. 5.4, we show the variation of ratcheting speed $\langle v \rangle$ with diffusivity D_0 of the tracer particle. The simulation parameters used are: $R_0 = 10$ μm, $v_{\text{slip}} = 1.0$ μm s^{-1}, $\lambda = 1.0$ μm, $\phi = -\pi/2$, $\omega = 70$ rad s^{-1}. We find that the ratcheting first increases and then the ratcheting speed becomes practically constant for a large range of diffusivity values.

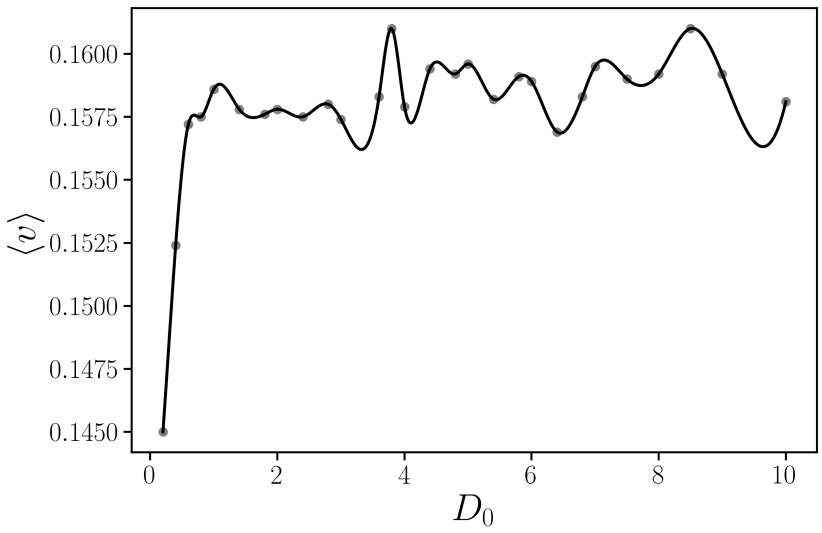

Figure 5.4: Variation of average velocity with the diffusivity D_0 of the tracer particle (D_0 in μm^2 s^{-1} and $\langle v \rangle$ in μm s^{-1}). Parameters: $R_0 = 10$ μm, $v_{\text{slip}} = 1.0$ μm s^{-1}, $\lambda = 1.0$ μm, $\phi = -\pi/2$, $\omega = 70$ rad s^{-1}.

5.3 Summary and Discussion

In this work, we have shown that a particular velocity field broken by a local inversion symmetry could be modeled for a fluid in an undulating microchannel in a very systematic manner. We first demonstrated that a self-consistent relationship exists between the surface undulations and the fluid velocity profile. Then, we revealed that a physically meaningful regime of tracer particle ratcheting exists in such velocity fields, where the particles are dragged by the fluid's velocity. This physically relevant regime exists in water at room temperature for sub-micrometer-sized particles in a channel approximately 10 micrometers in width. At least, such a regime becomes perturbatively accessible to analysis in low-Reynolds-number flows, revealing the details of the process's dependence on the magnitude and frequency of the surface drive, as well as the nature of the fluid.

Here, it is worth noting that Eq. 5.31 reveals a sharp dependence of the undulating velocity amplitude on the channel width as R_0^3 and the oscillation frequency as ω^2. Specifically, the cubic and quartic dependence on R_0 and ω are the ones that determine the energy input to the ratcheting particle. It renders ratcheting particularly pronounced in channels of micrometer width, thereby making transport very small or impossible in very small-width

nanochannels, at least within the purview of the present perturbative analysis. This particular observation could be crucial for biological systems. The frequency chosen in this chapter ensures that the velocity amplitude, treated as a perturbative correction, remains less than unity while still being sufficiently large to produce significant ratcheting transport.

The slip velocity v_{slip} may be interpreted as an effective parameter capturing near-wall interactions, which can arise from hydrodynamic slip, steric constraints, or mobility differences between the tracer and the surrounding fluid. In this sense, it provides a coarse-grained representation of tracer-boundary coupling beyond ideal no-slip conditions. In the present work, however, the tracer dynamics is governed solely by the velocity field generated by time-dependent wall undulations, and no explicit slip velocity term is included in the simulations. The interaction with the boundary is implemented via reflecting boundary conditions, which constrain motion without introducing a directional bias. Consequently, the observed directed transport arises purely from asymmetry in the induced flow field. Within the perturbative framework, the introduction of a finite v_{slip} is primarily required to ensure mathematical consistency of the solution. In the limit $v_{\text{slip}} \to 0$, the formulation exhibits unphysical behavior, such as time-growing boundary contributions, indicating a breakdown of the perturbative description in this limit. Therefore, v_{slip} should be regarded as an effective regularization parameter within the model, rather than as a fundamental physical requirement for transport. Importantly, the mechanism of directed transport remains governed by the asymmetry of the induced flow field, while v_{slip} serves to maintain a well-behaved and physically consistent description within the analytical framework.

Another key assumption in our model is the neglect of particle-boundary hydrodynamic interactions. For a single particle in confined geometry, these interactions refer to the influence of the channel walls on the fluid flow around the particle. These interactions depend strongly on the particle's proximity to the boundary and its size relative to the dimensions of the channel. When a tracer particle moves in confined channels, its diffusivity gets renormalized due to two factors, the first being the proximity of the tracer particle to the walls of the channels, making the diffusivity D_0 coordinate-dependent. Second is the undulations of the walls themselves. The spatiotemporal undulations can alter the diffusivity of the tracer in a complex manner that depends on the spectrum of the undulations [47]. Interestingly, these undulations can increase or decrease the diffusivity; analysis of the dynamics of the tracer particle, including all these effects, will be the pursuit of future explorations.

It should be noted that in this work, we have considered purely reflecting boundary conditions for the tracer particle, whereas in real situations, the boundary condition can be more complex, including partially absorbing and partially reflecting types, etc., depending upon the structure of the walls of the channel. These boundary conditions can themselves have a significant impact on the transport properties; however, in this initial analysis, our purpose has been to present the analytical method applicable in the situation of microchannel ratcheting, where a consistent handling of the velocity field is possible in the low-Reynolds-number regime.

In the present chapter, we have derived the velocity field for a spatiotemporally undulating microchannel to construct the equation of motion of a tracer particle by considering the dominant forces in the low Reynolds number regime: the viscous drag and the stochastic force. This approach, known as the quasi-steady Stokesian or Langevin model, is a common and powerful simplification. A complete treatment of particle dynamics in an unsteady low Reynolds number flow is described by the Basset–Boussinesq–Oseen (BBO) equation [104, 81, 105]. This equation includes additional terms, such as the Froude-Krylov force (due to pressure gradient), the added mass (inertia of the surrounding fluid), and the Basset history force (viscous memory of the flow), all of which arise from the unsteady nature of the flow. A detailed account of Fluid-Particle interaction is given in the Appendix B

6

Summary, Conclusions, and Future Outlook

In this chapter, we summarize the key findings of this thesis and discuss the future research directions.

6.1 Summary and Conclusion

In this thesis, we have explored two ratcheting mechanisms: surface undulations-driven ratcheting transport in a nanochannel, as discussed in Chapter 3, and fluid flow-structure driven ratcheting transport in a microchannel, as mentioned in Chapter 5. The surface undulations-driven mechanism is an entropic one, meaning that it arises purely due to the undulations of the surface geometry. In contrast, the one due to fluid flow structure is a result of the interaction between fluid flow and the tracer particle. In general, a tracer particle in a fluid confined by undulating surfaces will experience both of these effects, and studying these effects is necessary to understand the complete picture of tracer particle dynamics.

In Chapter 3, we showed how the undulation of the wall surface in a nanochannel can give rise to transport of a tracer particle and that the transport velocity peaks near room temperature for very realistic parameters such as viscosity equal to that of water and tracer particles of size about 10 nm.

In Chapter 4, we solved for the fluid velocity profile in an undulating nanochannel using

perturbation theory because of the advantage of low-Reynolds-number fluid flow. Using this perturbative treatment, we demonstrate the delineation between pressure-driven and surface-driven flow.

Finally, in Chapter 5 we studied the fluid flow structure in a soft microchannel with undulating walls and the transport of a tracer particle in this microchannel. We derived the structure of fluid flow in this microchannel and the Boundary modes sustaining this fluid flow structure. As shown in Chapter 5, the geometric term Itô in the Langevin equation (arising due to curvilinear geometry) pushes the particle near the boundary of the channel. Since surface-driven flow is stronger near the channel boundary, surface undulations are crucial for studying fluid or particle transport in a channel. Thus, this type of system with undulating walls naturally finds application in filtration and is worth exploring for the same.

The primary contribution of this thesis was not in introducing a fundamentally new physical principle, but in developing a quantitative and physically consistent framework to understand how time-dependent boundary deformations generate velocity fields that can induce directed transport.

6.2 Future Outlook

A natural extension of the research will consider the dynamics of many interacting tracer particles or structured particles in such a steady, inversion-symmetry-broken velocity field. How mutual cooperativity, specifically interparticle interactions, changes transport properties could be investigated within the present theoretical framework, as long as the particles remain tracer particles.

Another natural extension of the work will involve the many-particle dynamics, not only interacting through direct interactions (charged interactions or others), but also due to Hydrodynamic interactions.

Even studying the dynamics of a single particle in the presence of wall-driven hydrodynamic interaction is an interesting direction worth exploring. Due to the small scales of these systems, wall-driven hydrodynamic interactions become essential in both micro- and nanochannels.

Incorporating fluid-particle interactions into the model, where the particles are no longer tracers, would be an interesting direction. Involving the two-way coupling in fluid particle interaction, taking into account all necessary interactions, is an active and quite involved pursuit.

The success of the perturbative scheme developed in this thesis in the low Reynolds number regime motivates exploring all these possibilities in the future.

A

Ensemble and Time Averages

In statistical mechanics, observables describing physical systems are random quantities. For example, in Brownian motion, the position $x(t)$ or velocity $v(t)$ of a particle is not a single deterministic function of time, but changes from one realization of the experiment to another. To describe such quantities, the concepts of *ensemble averages* and *time averages* are useful.

Ensemble Average

Consider an observable $A(t)$ (for instance, $A(t) = x(t)$ or $A(t) = x^2(t)$) defined for a stochastic process. We conceptually imagine repeating the same experiment many times under identical macroscopic conditions (same temperature, same external fields, same initial preparation, etc.). Each repetition gives one *realization* or *trajectory*, which we label by an index $n = 1, 2, \ldots$. At a fixed time t, the *ensemble average* (denoted by angle bracket) of A is defined as

$$\langle A(t) \rangle = \sum_i A_i(t)\, P_i(t), \tag{1}$$

if the system can be in discrete states i with probabilities $P_i(t)$. In practice, in simulations or experiments with N independent realizations, this is approximated by

$$\langle A(t) \rangle \approx \frac{1}{N} \sum_{n=1}^{N} A^{(n)}(t), \tag{2}$$

where $A^{(n)}(t)$ is the value of the observable in the n-th realization at time t. Thus, an ensemble average is an average over *many copies of the system* at the *same time*.

Time Average

Instead of preparing many copies of the system, one may follow a *single* realization for a long duration and average the observable along that trajectory. For an observable $A(t)$, the *time average* (shown by overbar) over a time window of length T is defined as

$$\overline{A}_T = \frac{1}{T}\int_0^T A(t)\,\mathrm{d}t. \tag{3}$$

In discrete-time simulations with a time step δt and M time steps ($T = M\delta t$), this becomes

$$\overline{A}_T \approx \frac{1}{M}\sum_{k=0}^{M-1} A(t_k), \qquad t_k = k\,\delta t. \tag{4}$$

Here, the averaging is performed over *time* along a single trajectory, rather than over many realizations at a fixed time.

Relation Between Ensemble and Time Averages (Ergodicity)

For a stationary and ergodic system, the long-time limit of the time average along almost any trajectory coincides with the ensemble average:

$$\lim_{T\to\infty} \overline{A}_T = \lim_{t\to\infty} \langle A(t)\rangle. \tag{5}$$

This property is called *ergodicity*. It allows one to replace an ensemble average (over many realizations) by a long-time average along a single realization. Many equilibrium systems are ergodic, but non-equilibrium systems may fail to be ergodic, in which case ensemble and time averages need not coincide.

B

Fluid-Particle Interaction

Fluid–particle interaction refers to the way the dynamics of dispersed particles affect the fluid dynamics and vice versa. It is fundamentally governed by how momentum exchange is treated between the fluid and the dispersed particles. Depending on the particle size, concentration, and inertia, different coupling regimes are used. The two primary categories are *one-way coupling* and *two-way coupling*.

Governing Fluid and Particle Equations

The incompressible Navier-Stokes equations for the fluid phase are

$$\rho_f \left(\frac{\partial \boldsymbol{u}}{\partial t} + \boldsymbol{u} \cdot \nabla \boldsymbol{u} \right) = -\nabla p + \eta \nabla^2 \boldsymbol{u} + \boldsymbol{f}_p, \tag{1}$$

$$\nabla \cdot \boldsymbol{u} = 0, \tag{2}$$

where ρ_f and η are the density and dynamic viscosity of the fluid, and $\boldsymbol{f}_p$ represents the momentum forcing from particles, which may or may not be included depending on the coupling regime.

The motion of a spherical particle of radius a and mass m_p in the Stokes regime is

governed by the Basset–Boussinesq–Oseen (BBO) equation:

$$m_p \frac{d\boldsymbol{v}}{dt} = m_p \boldsymbol{g} - V_p(\rho_p - \rho_f)\boldsymbol{g} - 6\pi\eta a(\boldsymbol{v} - \boldsymbol{u}) - \rho_f V_p \frac{D\boldsymbol{u}}{Dt} - 6a^2\sqrt{\pi\rho_f\eta}\int_0^t \frac{1}{\sqrt{t-\tau}}\frac{d}{d\tau}(\boldsymbol{v} - \boldsymbol{u})\, d\tau. \tag{3}$$

The table below provides the meanings of various symbols in the equation above.

Symbol	**Meaning**
m_p	Mass of the particle
$\boldsymbol{v}(t)$	Particle velocity vector
$\frac{d\boldsymbol{v}}{dt}$	Particle acceleration
$\boldsymbol{g}$	Gravitational acceleration
V_p	Particle volume
ρ_p	Particle density
ρ_f	Fluid density
a	Particle radius
η	Dynamic viscosity of the fluid
$\boldsymbol{u}(t)$	Fluid velocity at particle location
$\frac{D\boldsymbol{u}}{Dt}$	Material derivative of fluid velocity
τ	Past time (integration variable)

Let us understand in a little more detail the physical meaning of each term of the BBO equation.

- **Particle inertia**:

  $$m_p \frac{d\boldsymbol{v}}{dt}$$

  represents the rate of change of particle momentum.

- **Weight of the particle**:

  $$m_p \boldsymbol{g}$$

  represents the downward gravitational force acting on the particle.

- **Buoyancy force**:
$$-V_p(\rho_p - \rho_f)\boldsymbol{g}$$
represents upward fluid buoyant effect (opposes gravity).

- **Stokes drag force**:
$$-6\pi\eta a(\boldsymbol{v} - \boldsymbol{u})$$
Viscous resistance to motion caused by relative velocity between particle and fluid.

- **Added mass force**:
$$-\rho_f V_p \frac{D\boldsymbol{u}}{Dt}$$
is the effective mass of the particle. The particle accelerates some of the surrounding fluid, effectively increasing its inertia.

- **Basset history force**:
$$-6a^2\sqrt{\pi\rho_f\eta}\int_0^t \frac{1}{\sqrt{t-\tau}}\frac{d}{d\tau}(\boldsymbol{v} - \boldsymbol{u})\,d\tau$$
represents the effect of delay, which keeps the fluid disturbed even after the cause is removed.

One-Way Coupling

In one-way coupling, particles are influenced by the fluid, but their feedback on the fluid is neglected. That is, we take:
$$\boldsymbol{f}_p = 0.$$
Thus, the fluid equations are solved independently, and then particle trajectories are computed via
$$m_p\frac{d\boldsymbol{v}}{dt} = \boldsymbol{F}_{\text{fluid}\to\text{particle}}.$$
This assumption is accurate in dilute suspensions, aerosols, dust in air, tracer particles in microfluidics, and Brownian particles in a dilute colloidal suspension.

Two-Way Coupling

Two-way coupling accounts for momentum transfer both ways. That is

$$\boldsymbol{f}_p \neq 0.$$

The forcing term can be written as

$$\boldsymbol{f}_p(\boldsymbol{x}, t) = \sum_{n=1}^{N_p} \boldsymbol{F}_n \, \delta(\boldsymbol{x} - \boldsymbol{x}_n), \tag{4}$$

where $\boldsymbol{F}_n$ is the interaction force from particle n on the fluid. That is, fluids affect particles, and particles in turn modify the motion of the fluids. This approximation means momentum exchange modifies fluid flow; therefore, we must solve particles and fluid *simultaneously*. In the above equations, we haven't considered the finite side of dispersed particles. The finite size of dispersed particles themselves adds the correction in the BBO equation (commonly known as Faxen's corrections or Faxen's Laws). Including Faxen's corrections with the BBO equation gives the Maxey-Riley-Gatignol equation. It is given by:

$$\begin{aligned} m_p \frac{d\boldsymbol{v}}{dt} = & \underbrace{(m_p - \rho_f V_p)\boldsymbol{g}}_{\text{buoyancy + weight}} + \underbrace{6\pi\eta a \left[(\boldsymbol{u} - \boldsymbol{v}) + \frac{a^2}{6}\nabla^2 \boldsymbol{u}\right]}_{\text{Stokes drag with Faxén}} \\ & + \underbrace{\rho_f V_p \left[\frac{D\boldsymbol{u}}{Dt} + \frac{a^2}{10}\nabla^2\left(\frac{D\boldsymbol{u}}{Dt}\right)\right]}_{\text{pressure-gradient/Faxén}} + \underbrace{\frac{1}{2}\rho_f V_p \left(\frac{D\boldsymbol{u}}{Dt} - \frac{d\boldsymbol{v}}{dt}\right)}_{\text{added mass}} \\ & + \underbrace{6\pi\eta a^2 \int_0^t \frac{d}{d\tau}\left[(\boldsymbol{u} - \boldsymbol{v}) + \frac{a^2}{6}\nabla^2 \boldsymbol{u}\right] \frac{d\tau}{\sqrt{\pi\nu(t-\tau)}}}_{\text{Basset history}} + \underbrace{\boldsymbol{F}_{\text{lift}} + \boldsymbol{F}_{\text{nonlin}}}_{\text{optional terms}}. \end{aligned} \tag{5}$$

Many-Particle Hydrodynamic Interactions (HI)

In the presence of particles dispersed in a fluid, the velocity disturbance created by one particle couples to every other particle through the fluid. These long-ranged couplings are called **hydrodynamic interactions** (HI). They fundamentally change the dynamics of the

fluid as well as the dispersed particles.

For an incompressible Newtonian fluid of dynamic viscosity η with velocity $\boldsymbol{u}(\boldsymbol{x})$ and pressure $p(\boldsymbol{x})$:

$$-\nabla p + \eta \nabla^2 \boldsymbol{u} + \boldsymbol{f}(\boldsymbol{x}) = \boldsymbol{0}, \tag{6}$$

$$\nabla \cdot \boldsymbol{u} = 0. \tag{7}$$

Here $\boldsymbol{f}(\boldsymbol{x})$ represents a body-force density which takes into account the effect of Hydrodynamic interactions (HI).

To find out the expression for Hydrodynamic interaction, one considers the presence of point dispersed particles acting as the source of disturbance in the fluid, which is equivalent to finding out the Green's function (known as the Oseen Tensor) for the Stokes' flow.

Free-Space Green's Function (Oseen Tensor)

The *Stokeslet* is the velocity field due to a point force $\boldsymbol{F}$ applied at $\boldsymbol{y}$:

$$-\nabla p + \eta \nabla^2 \boldsymbol{u} + \boldsymbol{F}\,\delta(\boldsymbol{x} - \boldsymbol{y}) = \boldsymbol{0}, \qquad \nabla \cdot \boldsymbol{u} = 0. \tag{8}$$

By linearity and translational invariance,

$$u_i(\boldsymbol{x}) = J_{ij}(\boldsymbol{r}) F_j, \qquad p(\boldsymbol{x}) = P_j(\boldsymbol{r}) F_j, \tag{9}$$

where J_{ij} is the *Oseen tensor* and it can be derived via Fourier transforms.

$$\boldsymbol{u}(\boldsymbol{r}) = \mathbf{J}(\boldsymbol{r}) \cdot \boldsymbol{F} = \frac{1}{8\pi\eta} \left(\frac{\mathbb{I}}{r} + \frac{\boldsymbol{r}\,\boldsymbol{r}}{r^3} \right) \cdot \boldsymbol{F}, \tag{10}$$

And the pressure field is given by:

$$p(\boldsymbol{r}) = \frac{\boldsymbol{F} \cdot \boldsymbol{r}}{4\pi r^3}. \tag{11}$$

Here, it is worth noting that the Oseen tensor diverges as r approaches zero since it is derived using point particle approximations. To address this, one employs the Rotne–Prager–Yamakawa (RPY) tensor in the computations, which regularizes the inter-

action by accounting for the finite size of the particles. The RPY tensor also suffers from the limitation that it ignores the near-field hydrodynamics. When the particles come very close to each other, near-field hydrodynamics, i.e., lubrication forces, become very large, which are completely ignored by the RPY tensor.

When two rigid surfaces approach with a thin fluid gap $\delta \ll a$, viscous resistance diverges. For two equal spheres (radius a) with surface-to-surface gap $\epsilon = \delta/a \ll 1$:

$$\text{Normal (squeeze) resistance:} \quad R^{\parallel} \sim \frac{6\pi\mu a^2}{\delta}, \tag{12}$$

$$\text{Tangential (shear) resistance:} \quad R^{\perp} \sim 6\pi\mu a \left[\ln\left(\frac{a}{\delta}\right) + C\right], \tag{13}$$

with a geometry-dependent constant C. These singular asymptotics are matched to far-field multipoles in *Stokesian Dynamics*, yielding accurate many-body resistance/mobility matrices over all separations. Another important effect that changes the fluid velocity profile is wall-induced hydrodynamic interactions (HI). When a particle moves in a viscous fluid near a boundary, the flow that it creates is modified by the presence of the wall. Because the wall enforces a no-slip boundary condition, the fluid cannot follow the same profile as in an unbounded domain; instead, the disturbance flow is reflected and distorted by the wall. These wall-induced modifications of the flow lead to wall-induced hydrodynamic interactions (HI). Even if only a single particle is present, the wall generates an "image system" of singularities (Stokeslet, source dipole, and higher multipoles) that alters the velocity field around the particle. As a result, the particle experiences a self-interaction (modified drag, lift forces, anisotropic mobility) and pairwise interaction with other nearby particles that differs from the free-space Oseen or RPY description. Physically, the wall screens and redirects the momentum carried by the flow, causing hydrodynamic interactions to become short-ranged, anisotropic, and non-pairwise additive. These wall-induced HI are essential in confined geometries. The classical representation of these effects is given by the Blake tensor, which is the Green's function of the Stokes equations in the presence of a no-slip wall.

C

Method of Characteristics for First-Order PDEs

In physics, we often encounter partial differential equations (PDEs) with variable coefficients. Of particular importance in terms of exact solution is the class of Linear and nonlinear first-order PDEs with variable coefficients. The method of characteristics is a powerful technique for solving linear and nonlinear first-order partial differential equations (PDEs). It converts the PDE into a set of ordinary differential equations (ODEs) along special curves called characteristic curves. Along these curves, the PDE simplifies to a total derivative, which can be integrated more easily.

A general form of the first-order PDEs in two variables x and y for which the method of characteristics can be applied is of the following form:

$$A(x,y,u)\,\frac{\partial}{\partial x}u(x,y) + B(x,y,u)\,\frac{\partial}{\partial y}u(x,y) = C(x,y,u), \tag{1}$$

where A, B, C are known functions, and the equation needs to be solved for $u(x,y)$.

Characteristic Curves

The key idea is to find curves $(x(s), y(s))$ in the (x,y)-plane along which u evolves as a function of a parameter s. Along such a curve $u(x,y) = u(x(s), y(s)) = u(s)$. Therefore,

using the chain rule, we get,

$$\frac{du}{ds} = \frac{\partial u}{\partial x}\frac{dx}{ds} + \frac{\partial u}{\partial y}\frac{dy}{ds}. \tag{2}$$

Comparing above equation with PDE (1), we choose

$$\frac{dx}{ds} = a(x, y, u), \qquad \frac{dy}{ds} = b(x, y, u), \qquad \frac{du}{ds} = c(x, y, u). \tag{3}$$

These three ODEs describe the characteristic curves and the evolution of the solution along them.

Solving the PDE

To solve (1):

1. Find the characteristic equations (3).
2. Solve the system of ODEs to obtain relations between x, y, and u.
3. Use initial or boundary conditions to determine constants of integration.
4. Write the solution implicitly or explicitly as $u(x, y)$.

Example: Linear Transport Equation

Consider the simplest transport equation

$$u_t + c\, u_x = 0, \tag{4}$$

with initial condition $u(x, 0) = f(x)$. The characteristic equations are:

$$\frac{dt}{ds} = 1, \qquad \frac{dx}{ds} = c, \qquad \frac{du}{ds} = 0. \tag{5}$$

Solving these:

$$t = s + \text{const}, \tag{6}$$

$$x = cs + \text{const}, \tag{7}$$

$$u = \text{constant along characteristic}. \tag{8}$$

Thus, characteristics are straight lines: $x - ct = \text{const}$, and the solution is:

$$u(x,t) = f(x - ct), \tag{9}$$

representing a wave that propagates without distortion at speed c.

D

Existence and Uniqueness of SDE Solutions

Stochastic differential equations (SDEs) are widely used in physics to describe the dynamics of systems under thermal fluctuations or random forces. A typical one-dimensional SDE takes the form

$$dX_t = a(X_t, t)\,dt + b(X_t, t)\,dW_t,$$

where the deterministic part $a(X_t, t)$ represents the drift of the process and the stochastic part $b(X_t, t)\,dW_t$ represents noise from the surrounding environment (e.g. Brownian motion due to molecular collisions). Here, W_t is a standard Wiener process. Before solving an SDE numerically or otherwise, one must ensure that the SDE admits a well-behaved solution. For this, a simple prescription is given below.

Existence and Uniqueness of Solutions

Theorem 1. *Consider the SDE*

$$dX_t = a(X_t, t)\,dt + b(X_t, t)\,dW_t, \qquad X_0 = x_0,$$

with measurable drift $a : \mathbb{R} \times [0, T] \to \mathbb{R}$ *and diffusion* $b : \mathbb{R} \times [0, T] \to \mathbb{R}$. *Assume the following conditions:*

1. ***Lipschitz continuity:*** *There exists a constant $L > 0$ such that, for all $x, y \in \mathbb{R}$ and $t \in [0, T]$,*

$$|a(x,t) - a(y,t)| + |b(x,t) - b(y,t)| \leq L|x - y|.$$

(Physically this means that small changes in state X cannot cause large, instantly amplified changes in drift or noise.)

2. ***Linear growth condition:*** *There exists $K > 0$ such that for all $x \in \mathbb{R}$ and $t \in [0, T]$,*

$$|a(x,t)|^2 + |b(x,t)|^2 \leq K(1 + |x|^2).$$

(It basically means that force or noise intensity cannot grow faster than linearly with X.)

Then, there exists a ***unique strong solution*** *X_t to the SDE on $[0, T]$ and the solution has continuous sample paths almost surely.*

Remark .1. *A* ***strong solution*** *means the system's randomness comes solely from the given Brownian motion W_t, defined on the same probability space. Physically, this ensures that if the initial conditions and the noise history are the same, the resulting trajectory of the system is also uniquely determined.*

In contrast, a ***weak solution*** *allows the probability space (and even the Brownian motion) to change, so trajectories are unique only in distribution.*

The above theorem guarantees that SDE modeling physical systems evolves in a predictable statistical manner and does not display unbounded or nonphysical behavior purely due to randomness.

Bibliography

[1] Outsider (Paweł Tokarz). Ion channel protein schematic, 2009. Public Domain. Accessed: 18 November 2025.

[2] Vossman. Side view of aquaporin 1 channel (pdb id: 1j4n), 2009. CC BY-SA 3.0. Accessed: 18 November 2025.

[3] Robert Brown. Xxvii. a brief account of microscopical observations made in the months of june, july and august 1827, on the particles contained in the pollen of plants; and on the general existence of active molecules in organic and inorganic bodies. *The philosophical magazine*, 4(21):161–173, 1828.

[4] Albert Einstein. Über die von der molekularkinetischen theorie der wärme geforderte bewegung von in ruhenden flüssigkeiten suspendierten teilchen. *Annalen der physik*, 4, 1905.

[5] William H Brock and David M Knight. The atomic debates:" memorable and interesting evenings in the life of the chemical society". *Isis*, 56(1):5–25, 1965.

[6] Marian Von Smoluchowski. Zur kinetischen theorie der brownschen molekularbewegung und der suspensionen. *Annalen der physik*, 326(14):756–780, 1906.

[7] Paul Langevin et al. Sur la théorie du mouvement brownien. *CR Acad. Sci. Paris*, 146(530-533):530, 1908.

[8] Xin Bian, Changho Kim, and George Em Karniadakis. 111 years of brownian motion. *Soft Matter*, 12(30):6331–6346, 2016.

[9] Peter Hänggi and Fabio Marchesoni. Introduction: 100years of brownian motion. *Chaos: An Interdisciplinary Journal of Nonlinear Science*, 15(2), 2005.

[10] Arthur Genthon. The concept of velocity in the history of brownian motion: From physics to mathematics and back. *The European Physical Journal H*, 45(1):49–105, 2020.

[11] Albert Libchaber. From biology to physics and back: The problem of brownian movement. *Annual Review of Condensed Matter Physics*, 10(1):275–293, 2019.

[12] William Sutherland. Lxxv. a dynamical theory of diffusion for non-electrolytes and the molecular mass of albumin. *The London, Edinburgh, and Dublin Philosophical Magazine and Journal of Science*, 9(54):781–785, 1905.

[13] Patrick Tabeling. *Introduction to microfluidics*. Oxford university press, 2023.

[14] Brian J Kirby. *Micro-and nanoscale fluid mechanics: transport in microfluidic devices*. Cambridge university press, 2010.

[15] Jan CT Eijkel and Albert Van Den Berg. Nanofluidics: what is it and what can we expect from it? *Microfluidics and Nanofluidics*, 1(3):249–267, 2005.

[16] Lydéric Bocquet and Elisabeth Charlaix. Nanofluidics, from bulk to interfaces. *Chemical Society Reviews*, 39(3):1073–1095, 2010.

[17] Patrick Abgrall and Nam-Trung Nguyen. *Nanofluidics*. Artech House, 2009.

[18] Mario Tagliazucchi and Igal Szleifer. Transport mechanisms in nanopores and nanochannels: can we mimic nature? *Materials Today*, 18(3):131–142, 2015.

[19] YA Perez Sirkin, M Tagliazucchi, and Ijmta Szleifer. Transport in nanopores and nanochannels: some fundamental challenges and nature-inspired solutions. *Materials Today Advances*, 5:100047, 2020.

[20] Imre Derényi and R Dean Astumian. ac separation of particles by biased brownian motion in a two-dimensional sieve. *Physical Review E*, 58(6):7781, 1998.

[21] Mukul Sonker, Daihyun Kim, Ana Egatz-Gomez, and Alexandra Ros. Separation phenomena in tailored micro-and nanofluidic environments. *Annual Review of Analytical Chemistry*, 12:475–500, 2019.

[22] Franziska M Esmek, Parisa Bayat, Fabián Pérez-Willard, Tobias Volkenandt, Robert H Blick, and Irene Fernandez-Cuesta. Sculpturing wafer-scale nanofluidic devices for dna single molecule analysis. *Nanoscale*, 11(28):13620–13631, 2019.

[23] Jianping Fu, Reto B Schoch, Anna L Stevens, Steven R Tannenbaum, and Jongyoon Han. A patterned anisotropic nanofluidic sieving structure for continuous-flow separation of dna and proteins. *Nature nanotechnology*, 2(2):121–128, 2007.

[24] Yong Zeng and D Jed Harrison. Self-assembled colloidal arrays as three-dimensional nanofluidic sieves for separation of biomolecules on microchips. *Analytical chemistry*, 79(6):2289–2295, 2007.

[25] Jianping Fu, Pan Mao, and Jongyoon Han. Continuous-flow bioseparation using microfabricated anisotropic nanofluidic sieving structures. *nature protocols*, 4(11):1681, 2009.

[26] M Napoli, Jan CT Eijkel, and S Pennathur. Nanofluidic technology for biomolecule applications: a critical review. *Lab on a Chip*, 10(8):957–985, 2010.

[27] Xiayan Wang, Shili Wang, Vijaykumar Veerappan, Chang Kyu Byun, Han Nguyen, Brina Gendhar, Randy D Allen, and Shaorong Liu. Bare nanocapillary for dna separation and genotyping analysis in gel-free solutions without application of external electric field. *Analytical chemistry*, 80(14):5583–5589, 2008.

[28] Howard A Stone, Abraham D Stroock, and Armand Ajdari. Engineering flows in small devices: microfluidics toward a lab-on-a-chip. *Annu. Rev. Fluid Mech.*, 36:381–411, 2004.

[29] Daniel Mark, Stefan Haeberle, Günter Roth, Felix Von Stetten, and Roland Zengerle. Microfluidic lab-on-a-chip platforms: requirements, characteristics and applications. *Microfluidics based microsystems: fundamentals and applications*, pages 305–376, 2010.

[30] OA Saleh and LL Sohn. Quantitative sensing of nanoscale colloids using a microchip coulter counter. *Review of Scientific Instruments*, 72(12):4449–4451, 2001.

[31] Anirban Mitra, Bradley Deutsch, Filipp Ignatovich, Carrie Dykes, and Lukas Novotny. Nano-optofluidic detection of single viruses and nanoparticles. *ACS nano*, 4(3):1305–1312, 2010.

[32] Harikrishnan Jayamohan, Himanshu J Sant, and Bruce K Gale. Applications of microfluidics for molecular diagnostics. In *Microfluidic Diagnostics*, pages 305–334. Springer, 2013.

[33] Aleksandr Noy, Hyung Gyu Park, Francesco Fornasiero, Jason K Holt, Costas P Grigoropoulos, and Olgica Bakajin. Nanofluidics in carbon nanotubes. *Nano today*, 2(6):22–29, 2007.

[34] Jiabo Tao, Xianyu Song, Teng Zhao, Shuangliang Zhao, and Honglai Liu. Confinement effect on water transport in cnt membranes. *Chemical Engineering Science*, 192:1252–1259, 2018.

[35] Sander J Tans, Michel H Devoret, Hongjie Dai, Andreas Thess, Richard E Smalley, LJ Geerligs, and Cees Dekker. Individual single-wall carbon nanotubes as quantum wires. *Nature*, 386(6624):474–477, 1997.

[36] Savas Berber, Young-Kyun Kwon, and David Tománek. Unusually high thermal conductivity of carbon nanotubes. *Physical review letters*, 84(20):4613, 2000.

[37] Philip Kim, Li Shi, Arun Majumdar, and Paul L McEuen. Thermal transport measurements of individual multiwalled nanotubes. *Physical review letters*, 87(21):215502, 2001.

[38] Francisco Antonio Perdigones, Antonio Luque, and Jose M Quero. Correspondence between electronics and fluids in mems: Designing microfluidic systems using electronics. *IEEE Industrial Electronics Magazine*, 8(4):6–17, 2014.

[39] John Happel and Howard Brenner. *Low Reynolds number hydrodynamics: with special applications to particulate media*, volume 1. Springer Science & Business Media, 1983.

[40] George Karniadakis, Ali Beskok, and Narayan Aluru. *Microflows and nanoflows: fundamentals and simulation*, volume 29. Springer Science & Business Media, 2006.

[41] Edward M Purcell. Life at low reynolds number. In *Physics and our world: reissue of the proceedings of a symposium in honor of Victor F Weisskopf*, pages 47–67. World Scientific, 2014.

[42] Todd M Squires and Stephen R Quake. Microfluidics: Fluid physics at the nanoliter scale. *Reviews of modern physics*, 77(3):977, 2005.

[43] Shagun Gupta, Kritika Ramesh, Suhaib Ahmed, and Vipan Kakkar. Lab-on-chip technology: A review on design trends and future scope in biomedical applications. *Int. J. Bio-Sci. Bio-Technol*, 8(5):311–322, 2016.

[44] Semra Akgönüllü, Monireh Bakhshpour, Ayşe Kevser Pişkin, and Adil Denizli. Microfluidic systems for cancer diagnosis and applications. *Micromachines*, 12(11):1349, 2021.

[45] Rachid Ait-Haddou and Walter Herzog. Brownian ratchet models of molecular motors. *Cell biochemistry and biophysics*, 38(2):191–213, 2003.

[46] SN Ethier and Jiyeon Lee. The tilted flashing brownian ratchet. *Fluctuation and Noise Letters*, 18(01):1950005, 2019.

[47] Sophie Marbach, David S Dean, and Lydéric Bocquet. Transport and dispersion across wiggling nanopores. *Nature Physics*, 14(11):1108–1113, 2018.

[48] M Y Jaffrin and A H Shapiro. Peristaltic pumping. *Annual Review of Fluid Mechanics*, 3(Volume 3, 1971):13–37, 1971.

[49] Christina Kurzthaler, Danielle L. Chase, and Howard A. Stone. Surface corrugations induce helical near-surface flows and transport in microfluidic channels. *Journal of Fluid Mechanics*, 982:A31, 2024.

[50] P Sajeesh and Ashis Kumar Sen. Particle separation and sorting in microfluidic devices: a review. *Microfluidics and nanofluidics*, 17:1–52, 2014.

[51] Aleksandra Słapik and Jakub Spiechowicz. Tunable particle separation via deterministic absolute negative mobility. *Scientific Reports*, 10(1):16639, 2020.

[52] L Gorre-Talini, S Jeanjean, and Pascal Silberzan. Sorting of brownian particles by the pulsed application of an asymmetric potential. *Physical Review E*, 56(2):2025, 1997.

[53] Andrej Grimm, Holger Stark, and Johan RC van der Maarel. Model for a brownian ratchet with improved characteristics for particle separation. *Physical Review E—Statistical, Nonlinear, and Soft Matter Physics*, 79(6):061102, 2009.

[54] C Keller, Florian Marquardt, and C Bruder. Separation quality of a geometric ratchet. *Physical Review E*, 65(4):041927, 2002.

[55] Masumi Yamada, Megumi Nakashima, and Minoru Seki. Pinched flow fractionation: continuous size separation of particles utilizing a laminar flow profile in a pinched microchannel. *Analytical chemistry*, 76(18):5465–5471, 2004.

[56] R Dean Astumian and Martin Bier. Fluctuation driven ratchets: molecular motors. *Physical review letters*, 72(11):1766, 1994.

[57] R Dean Astumian. Thermodynamics and kinetics of a brownian motor. *science*, 276(5314):917–922, 1997.

[58] A Bhattacharyay. Directed transport in equilibrium: A model study. *Physica A: Statistical Mechanics and its Applications*, 391(4):1111–1119, 2012.

[59] Martin B Tarlie and R Dean Astumian. Optimal modulation of a brownian ratchet and enhanced sensitivity to a weak external force. *Proceedings of the National Academy of Sciences*, 95(5):2039–2043, 1998.

[60] Lukas Bogunovic, Ralf Eichhorn, Jan Regtmeier, Dario Anselmetti, and Peter Reimann. Particle sorting by a structured microfluidic ratchet device with tunable selectivity: theory and experiment. *Soft Matter*, 8(14):3900–3907, 2012.

[61] Emily S Park, Simon P Duffy, and Hongshen Ma. Microfluidic separation of circulating tumor cells based on size and deformability. In *Circulating Tumor Cells*, pages 21–32. Springer, 2017.

[62] D Caballero, Jaideep Katuri, J Samitier, and Samuel Sanchez. Motion in microfluidic ratchets. *Lab on a Chip*, 16(23):4477–4481, 2016.

[63] Maurice J Chacron and Gary W Slater. Particle trapping and self-focusing in temporally asymmetric ratchets with strong field gradients. *Physical Review E*, 56(3):3446, 1997.

[64] David Caballero, Rui L Reis, and Subhas C Kundu. Trapping metastatic cancer cells with mechanical ratchet arrays. *Acta Biomaterialia*, 170:202–214, 2023.

[65] Marian Smoluchowski. Experimentell nachweisbare, der üblichen thermodynamik widersprechende molekular-phänomene. *Physikalische Zeitschrift*, 13:1069–1080, 1912.

[66] Richard P Feynman, Robert B Leighton, Matthew Sands, and Everett M Hafner. The feynman lectures on physics; vol. i. *American Journal of Physics*, 33(9):750–752, 1965.

[67] Gonzalo Pablo Suárez, Miguel Hoyuelos, and Dante R Chialvo. Invited review: Fluctuation-induced transport. from the very small to the very large scales. *Papers in physics*, 8(1):0–0, 2016.

[68] Léon Brillouin. Can the rectifier become a thermodynamical demon? *Physical Review*, 78(5):627, 1950.

[69] Alex_X. Atp synthase structure, 2007. CC BY-SA 3.0. Accessed: 18 November 2025.

[70] Peter Hänggi and Fabio Marchesoni. Artificial brownian motors: Controlling transport on the nanoscale. *Reviews of Modern Physics*, 81(1):387, 2009.

[71] Slagt and Bcjordan. Motility of kinesin along a microtubule, 2009. Public Domain. Accessed: 18 November 2025.

[72] G. E. P. Box and M. E. Muller. A note on the generation of random normal deviates. *Annals of Mathematical Statistics*, 29(2):610–611, 1958.

[73] E. R. Golder and J. G. Settle. The box–müller method for generating pseudo-random normal deviates. *Journal of the Royal Statistical Society: Series C (Applied Statistics)*, 25(1):12–20, 1976.

[74] David W. Scott. Box–muller transformation. *WIREs Computational Statistics*, 3:177–179, 2011.

[75] Arijit Bhattacharyay et al. Room temperature flashing ratcheting in nano-channels. *Physica A: Statistical Mechanics and its Applications*, 622:128889, 2023.

[76] Imre Derényi, Martin Bier, and R Dean Astumian. Generalized efficiency and its application to microscopic engines. *Physical review letters*, 83(5):903, 1999.

[77] CJ Olson Reichhardt and Charles Reichhardt. Ratchet effects in active matter systems. *Annual Review of Condensed Matter Physics*, 8:51–75, 2017.

[78] Danielle McDermott, Cynthia J Olson Reichhardt, and Charles Reichhardt. Collective ratchet effects and reversals for active matter particles on quasi-one-dimensional asymmetric substrates. *Soft Matter*, 12(41):8606–8615, 2016.

[79] Aakash Anand and Arijit Bhattacharyay. Flow cross-overs under surface fluctuations in cylindrical nano-channel. *Physics Letters A*, page 130676, 2025.

[80] Tsutomu Kambe. *Elementary fluid mechanics*. World Scientific, 2007.

[81] Lev D Landau. Fluid mechanics, course of theoretical physics, vol. 6. *Addison-Wesley Publishing Co.*, 1959.

[82] R Dean Astumian and Peter Hänggi. Brownian motors. *Physics today*, 55(11):33–39, 2002.

[83] Joel S Bader, Richard W Hammond, Steven A Henck, Michael W Deem, Gregory A McDermott, James M Bustillo, John W Simpson, Gregory T Mulhern, and Jonathan M Rothberg. Dna transport by a micromachined brownian ratchet device. *Proceedings of the National Academy of Sciences*, 96(23):13165–13169, 1999.

[84] SN Ethier and Jiyeon Lee. The flashing brownian ratchet and parrondo's paradox. *Royal Society Open Science*, 5(1):171685, 2018.

[85] Martin Bier. Brownian ratchets in physics and biology. *Contemporary Physics*, 38(6):371–379, 1997.

[86] Aakash Anand and A Bhattacharyay. Hydrodynamic ratchet for tracer transport in a soft microchannel: A detailed analysis. *arXiv preprint arXiv:2510.12492*, 2025.

[87] Pijush K Kundu, IM Cohen, and DR Dowling. Fluid mechanics, academic press. *Philadelphia, Pennsylvania*, 1990.

[88] George Keith Batchelor. *An introduction to fluid dynamics*. Cambridge university press, 2000.

[89] Peter Eris Kloeden, Eckhard Platen, and Henri Schurz. *Numerical solution of SDE through computer experiments*. Springer Science & Business Media, 2012.

[90] Venkataraman Balakrishnan. *Elements of nonequilibrium statistical mechanics*, volume 3. Springer, 2008.

[91] Noëlle Pottier. *Nonequilibrium statistical physics: linear irreversible processes*. Oxford University Press, 2009.

[92] Ascher H Shapiro, Michel Yves Jaffrin, and Steven Louis Weinberg. Peristaltic pumping with long wavelengths at low reynolds number. *Journal of fluid mechanics*, 37(4):799–825, 1969.

[93] Eric Lauga, Michael P Brenner, and Howard A Stone. Microfluidics: The no-slip boundary condition. *Perspective*, 17:1, 2006.

[94] Lydéric Bocquet and Jean-Louis Barrat. Flow boundary conditions from nano-to micro-scales. *Soft matter*, 3(6):685–693, 2007.

[95] Derek C Tretheway and Carl D Meinhart. Apparent fluid slip at hydrophobic microchannel walls. *Physics of fluids*, 14(3):L9–L12, 2002.

[96] Chiara Neto, Drew R Evans, Elmar Bonaccurso, Hans-Jürgen Butt, and Vincent SJ Craig. Boundary slip in newtonian liquids: a review of experimental studies. *Reports on progress in physics*, 68(12):2859, 2005.

[97] Nakhlé H Asmar. *Partial differential equations with Fourier series and boundary value problems*. Courier Dover Publications, 2016.

[98] Tyn Myint-U and Lokenath Debnath. *Linear partial differential equations for scientists and engineers*. Springer, 2007.

[99] Bernt Oksendal. *Stochastic differential equations: an introduction with applications*. Springer Science & Business Media, 2013.

[100] Uffe Høgsbro Thygesen. *Stochastic differential equations for science and engineering*. Chapman and Hall/CRC, 2023.

[101] Hannes Risken. Fokker-planck equation. In *The Fokker-Planck equation: methods of solution and applications*, pages 63–95. Springer, 1989.

[102] Crispin W Gardiner and Peter Zoller. Springer series in synergetics, 2009.

[103] Nicolaas Godfried Van Kampen. *Stochastic processes in physics and chemistry*, volume 1. Elsevier, 1992.

[104] Martin R Maxey and James J Riley. Equation of motion for a small rigid sphere in a nonuniform flow. *The Physics of Fluids*, 26(4):883–889, 1983.

[105] Alfred Barnard Basset. *A treatise on hydrodynamics: with numerous examples*, volume 2. Deighton, Bell and Company, 1888.